

2013

A Study Of Cytocompatibility And Biodegradability Of Az31 Magnesium Alloy In Simulated Airway Surface Lining Fluid

Daniel R. Owuor
North Carolina Agricultural and Technical State University

Follow this and additional works at: <https://digital.library.ncat.edu/theses>

Recommended Citation

Owuor, Daniel R., "A Study Of Cytocompatibility And Biodegradability Of Az31 Magnesium Alloy In Simulated Airway Surface Lining Fluid" (2013). *Theses*. 317.
<https://digital.library.ncat.edu/theses/317>

This Thesis is brought to you for free and open access by the Electronic Theses and Dissertations at Aggie Digital Collections and Scholarship. It has been accepted for inclusion in Theses by an authorized administrator of Aggie Digital Collections and Scholarship. For more information, please contact iyanna@ncat.edu.

A Study of Cytocompatibility and Biodegradability of AZ31 Magnesium Alloy in Simulated
Airway Surface Lining Fluid

Daniel R. Owuor

North Carolina A&T State University

A thesis submitted to the graduate faculty
in partial fulfillment of the requirements for the degree of

MASTER OF SCIENCE

Department: Chemical, Biological Engineering and Bioengineering

Major: Bioengineering

Major Professor: Dr. Yeoheung Yun

Greensboro, North Carolina

2013

School of Graduate Studies
North Carolina Agricultural and Technical State University
This is to certify that the Master's Thesis of

Daniel R. Owuor

has met the thesis requirements of
North Carolina Agricultural and Technical State University

Greensboro, North Carolina
2013

Approved by:

Dr. Yeoheung Yun
Major Professor

Dr. Jenora T. Waterman
Co-Advisor

Dr. Jagannathan Sankar
Committee Member

Dr. Leonard Uitenham
Department Chair

Dr. Sanjiv Sarin
Dean, The Graduate School

© Copyright by
Daniel R. Owuor
2013

Biographical Sketch

Daniel R. Owuor graduated from North Carolina Agricultural and Technical State University with a Bachelor of Science degree in Mechanical Engineering in May 2011. He is a candidate for the Master of Science degree in Bioengineering at North Carolina Agricultural and Technical State University, where he continued working as a Research Assistant for the National Science Foundation Engineering Research Center for Revolutionizing Metallic Biomaterials until the completion of his degree requirements.

Dedication

I would like to dedicate this work to my Aunt Ruth for her love, caring, and support.

Acknowledgements

It would not have been possible to write this thesis without the help and support of the kind people around me, to only some of whom it is possible to give particular mention here.

Firstly I would like to express my deepest gratitude to Dr. Yeoheung Yun, my advisor for giving me the opportunity to work on this project. I want to thank not only for his knowledge and insightful support during the course of this work, but also for his willingness to motivate and push me beyond my comfort zone to enable me to realize my potential. I am thankful to Dr.

Jagannathan Sankar, for mentoring and introducing me to the ERC. This rare opportunity has allowed me the opportunity to learn new skills as well as meet an outstanding group of people.

I would also like to thank Dr. JangYongseok for his kindness and endless support during the course of my work by sharing his knowledge of experiments. I would like to extend my sincere gratitude to Dr. Jenora Waterman for her guidance and insight during my cell culture experiments, her input was extremely valuable and very much appreciated. Much thanks to Dr. Boyce Collins for his availability to answer any questions I had regarding my research and more importantly ensuring safety in the labs. I am thankful to Dr. Zhigang Xu for training me to use the SEM which proved to be very useful in my research. Much thanks to Dr. Ram Gupta for providing me with the basic knowledge needed to use the XRD machine. Moreover, I would like to thank my lab mates Leon White, Chris Mahoney, Nevija Watson, Lauren Douglas-Byrd and Christopher Smith for the fruitful discussions and the great working atmosphere.

Lastly, I would like to thank my family for all their love, support and encouragement. For my parents who raised me with a love of science and supported me in all my pursuits and allowing me to dream big. All their sacrifice to give me good education is being rewarded now, and my achievement is no less than theirs too.

Table of Contents

List of Figures	x
List of Tables	xiii
Nomenclature and Symbols	xiv
Abstract	2
CHAPTER 1 Introduction.....	3
1.1 Background	3
1.1.1 Anatomy of the trachea.	5
1.1.2 Tracheal stenosis.	6
CHAPTER 2 Literature Review	7
2.1 Airway Surface Liquid Overview	7
2.2 Components in the Airway Lining.....	8
2.2.1 Ionic and chemical composition in the airway.....	8
2.2.2 Mucus and mucin role in the airway.	8
2.2.3 Airway stent/tissue interface.	9
2.3 Historical Background on Magnesium.....	10
2.4 Magnesium as a Biodegradable Implant Material.....	11
2.5 Corrosion of Magnesium.....	14
2.5.1 Negative difference effect (NDE).	15
2.5.2 The pourbaix diagram for magnesium corrosion.	15
2.5.3 Galvanic corrosion.	17

2.5.4 Pitting corrosion.	18
2.5.5 Stress cracking corrosion (SCC).	18
2.6 Surface Treatment of Magnesium Alloy.....	19
2.6.1 Plasma electrolytic oxidation (PEO).	20
2.6.2 Polymer coating (PLGA).....	21
2.7 Problem Statement	22
CHAPTER 3 Materials and Methods	24
3.1 Sample.....	24
3.2 Solution	25
3.3 Porcine Stomach Mucin	27
3.4 Corrosion Characterization	27
3.4.1 pH measurement.....	28
3.4.2 Immersion test.	28
3.4.3 Open circuit potential (OCP).....	28
3.4.4 Electrochemical impedance spectroscopy (EIS).	29
3.4.5 Linear polarization resistance (LPR).....	29
3.4.6 Potentiodynamic polarization.....	29
3.5 Plasma Electrolytic Oxidation (PEO)	30
3.6 Polymer (PLGA) coating	31
3.7 Cell Adhesion Assay	32

3.8 Surface Characterization	32
3.8.1 Scanning electron microscopy (SEM).....	33
3.8.2 X-ray diffraction (XRD).....	33
3.8.3 X-ray computed tomography (micro-CT).	33
CHAPTER 4 Results and Discussion	35
4.1 Immersion Tests Results	35
4.1.1 pH measurement results.	35
4.1.2 X-ray computed tomography (micro-CT) results.....	37
4.1.3 Scanning electron microscope results.	37
4.1.4 X-ray diffraction (XRD) results.	47
4.2 Electrochemical Test Results	47
4.2.1 pH measurement.....	47
4.2.2 Open circuit potential (OCP).....	48
4.2.3 Electrochemical impedance spectroscopy (EIS) results.....	50
4.2.4 Linear polarization resistance (LPR).....	57
4.2.5 Potentiodynamic polarization.....	60
4.3 Plasma Electrolytic Oxidation and PLGA Coating Results	61
4.4 Cell Adhesion Assay Results	66

CHAPTER 5 Conclusions and Future Work	71
References	74
<i>Appendix</i>	90

List of Figures

Figure 1. Anatomy of Trachea (a) Trachea and main bronchi (b) Schematic view of the axial cross-section (Source: WebMD.com).....	6
Figure 2. Epithelial cells, Cilia and Mucus layer illustrating defense mechanisms in the airway..	7
Figure 3. Reactions between magnesium alloy and aqueous environment.	14
Figure 4. Magnesium's pourbaix diagram in H ₂ O (Makar and Kruger 1993).....	16
Figure 5. Schematic description of a ceramic coating prepared by the PEO process.....	21
Figure 6. Electrochemical testing setup.	27
Figure 7. Scheme of square waveform of applied voltage (V) with time (t).	30
Figure 8. Plasma Electrolytic Oxidation experimental setup.....	31
Figure 9. Micro-CT System Nanotom-M at North Carolina A&T State University.	34
Figure 10. Variation of pH plot on the AZ31 samples showing the effect mucin and HCO ₃ ⁻ increase in Gamble solution.....	36
Figure 11. SEM images of corroded surface after immersion test for 10 days. Solutions had 0 g/l concentration of mucin with (a) 0 HCO ₃ ; (b) 1 HCO ₃ ; (c) 2.6 HCO ₃ ; (d) 4HCO ₃	38
Figure 12. SEM images of corroded surface after immersion test for 10 days. Solutions had 0 g/L HCO ₃ with (a) 0 g/l mucin; (b) 0.03 g/l mucin; (c) 0.1 g/l mucin.	39
Figure 13. SEM images of corroded surface after immersion test for 10 days. Solutions had 4 g/l HCO ₃ with (a) 0g/l mucin; (b) 0.03 g/l mucin; (c) 0.1 g/l mucin.	40
Figure 14. SEM images showing mapping images of cross-sections of corrosion products formed after immersion for 10 days in Gamble solution; (a) 0 g/l HCO ₃ , 0 g/l mucin, (b) 0 g/l HCO ₃ , 0.1 g/l mucin, (c) 2.6 g/l HCO ₃ , 0 g/l mucin and (d) 2.6 g/l HCO ₃ , 0.1 g/l mucin.	43

Figure 15. Line analysis of cross section on corrosion products after immersion test in the solutions (a) 0 g/l HCO_3^- , 0 g/l Mucin, (b) 2.6 g/l HCO_3^- , 0 g/l Mucin.....	44
Figure 16. SEM cross-section morphology comparing the corrosion products thickness on the samples in different solution concentrations; (a) 0 g/l HCO_3^- , 0 g/l Mucin, (b) 2.6 g/l HCO_3^- , 0 g/l Mucin, (c) 4 g/l HCO_3^- , 0 g/l Mucin (d) 0 g/l HCO_3^- , 0.1 g/l Mucin, (e) 2.6 g/l HCO_3^- , 0.1 g/l Mucin and (f) 4 g/l HCO_3^- , 0.1 g/l Mucin.....	46
Figure 17. Variation of pH plot showing the effect of mucin increase on the pH of Gamble solution containing 4 g/l HCO_3^- during electrochemical testing.	48
Figure 18. OCP plots comparing the mucin effect on the samples immersed in Gamble solution containing different concentration of HCO_3^- ions for 24 hour at 37°C. (a) 0 g/ml mucin; (b) 0.03 g/l mucin; (c) 0.1 g/l mucin.....	49
Figure 19. Schematic representation corresponding to equivalent circuit of EIS plot.	51
Figure 20. EIS nyquist plots of sample immersed in Gamble solution containing 0g/l HCO_3^- showing the effect of mucin increase. (a) 0g/l Mucin (b) 0.03 g/l mucin; (c) 0.1 g/l mucin.....	52
Figure 21. EIS nyquist plots of sample immersed in Gamble solution containing 0g/l mucin showing the effect of increasing carbonate ions (a) 0 g/l HCO_3^- ; (b) 1 g/l HCO_3^- ; (c) 2.6 g/l HCO_3^- ; (d) 4 g/l HCO_3^-	54
Figure 22. Nyquist plots of untreated magnesium AZ31 samples immersed in Gamble solution in different concentrations of mucin.	56
Figure 23. Linear polarization curves of sample immersed in Gamble solution containing 2.6 g/l HCO_3^- , 0g/l mucin for 24 hours.	58
Figure 24. Potentiodynamic polarization curves of untreated magnesium AZ31 samples immersed in Gamble solution with different concentrations of mucin.....	60

Figure 25. Potentiodynamic polarization curves of AZ31 alloy in Gamble solution.	62
Figure 26. Nyquist plots of untreated anodized AZ31 and anodized+ PLGA coated AZ31 in Gamble solution at 37°C.	63
Figure 27. Surface morphologies of AZ31B anodized surface.....	65
Figure 28. Optical light microscopy image showing control PTE cells attached on a glass substrate.	67
Figure 29. SEM images of PTE cells adhered on the surfaces after the cell adhesion assay for 12 hours. (a) untreated AZ31, (b) Anodized coated AZ31, (c) Untreated AZ31 coated with 2wt% PLGA and (d) untreated AZ31 coated with 2wt% PLGA with 10% paclitaxel drug.....	68

List of Tables

Table 1 Differences between silicone and expandable metallic stents (Wood, 2001).....	4
Table 2 Mechanical properties of Magnesium alloy compared to Natural Bone and other engineering materials (Staiger, et al., 2006)	12
Table 3 Concentrations of chemicals used to prepare Gamble solution or SLF (Marques, et al., 2011)	25
Table 4 Test solutions with different concentrations of mucin and sodium carbonate (NaHCO_3) in Gamble solution.....	26
Table 5 Chemical composition of corrosion products formed on the surface after immersion test in solutions for 10 days detected by EDX analysis (Unit: Atomic %)	41
Table 6 Parameters of EIS showing the effect of mucin increase in Gamble solution.....	53
Table 7 Parameters of EIS showing the effect of carbonate ions in Gamble solution.....	55
Table 8 Parameters of untreated AZ31 by fitting EIS model carried out in Gamble with different concentrations of mucin	57
Table 9 Linear polarization data measurement by Gamry Echem Analyst software of untreated AZ31 alloy immersed in Gamble solution containing 2.6 g/l HCO_3^- , 0g/l mucin for 24 hours. ..	59
Table 10 Parameters of untreated magnesium AZ31 samples immersed in Gamble solution with different concentrations of mucin	61
Table 11 Parameters of untreated, anodized AZ31 and anodized+ PLGA AZ31 by fitting DC polarization curve obtained in Gamble solution	63
Table 12 Parameters of untreated anodized and anodized + PLGA AZ31 samples obtained from EIS model carried out in Gamble solution.....	64

Nomenclature and Symbols

ASL	Airway Surface Liquid
CE	Counter Electrode
CT	Computed Tomography
DMEM	Dulbecco's Modified Eagle Medium
EDX	Energy-Dispersive X-ray Spectroscopy
EIS	Electrochemical Impedance Spectroscopy
LPR	Linear Polarization Potential
NDE	Negative Difference Effect
OCP	Open Circuit Potential
PEO	Plasma Electrolytic Oxidation
PCL	Periciliary Liquid
PLGA	Poly (Lactic-co-Glycolic Acid)
PTE	Porcine Tracheal Epithelial
RE	Reference Electrode
SCC	Stress Corrosion Cracking
SEM	Scanning Electron Microscopy
SLF	Simulated Lung Fluid
WE	Working Electrode
XRD	X-Ray Diffraction

Abstract

The nature of magnesium alloys to degrade is attributed to the high oxidative corrosion rates which are attractive for a biodegradable medical implant since they will avoid a removal surgery by gradually degrading and being absorbed by the body. In this thesis project, the biocorrosion characteristics of AZ31 Mg alloy are investigated in a simulated physiological solution mimicking the airway surface lining fluid. Particular attention was focused on the effect of carbonate ions present in the solution and porcine stomach mucin added to the test solution to create an *in vitro* model of the epithelial mucus surfaces mimicking the epithelial surface along the trachea. The corrosion behavior of the samples was analyzed using both immersion and electrochemical tests. The morphological characterization of the samples was performed using X-ray computed tomography (Micro-CT) and scanning electron microscopy (SEM). Chemical composition of the surface corrosion products was determined with electron dispersive X-ray spectroscopy (EDX) and X-ray diffraction (XRD). The results showed that addition of bicarbonate ions accelerated uniform corrosion rate with the increase of bicarbonate concentration while mucin decelerated the corrosion rate of the samples by adhering to the surface thereby reducing the amount of corrosion products formed on the surface. *In vitro* cytocompatibility studies were performed using porcine tracheal epithelial (PTE) cells which proved to be non-toxic and biocompatible to the Mg alloy. The experimental data in this thesis project is intended to be used as foundation knowledge to predict the corrosion behavior of AZ31 Mg alloy in the physiological environment, in order to provide degradation information for future *in vivo* study to be utilized as a tracheal stent device.

CHAPTER 1

Introduction

1.1 Background

Airway stenting has now been an integral part of the medical armamentarium for more than a decade and is proven to offer effective palliation for patients with airway stenosis complications (Dumon, 1990). Airway stents are hollow prosthetic devices made of metal, polymers or a combination of both and are placed in the airway intended to restore airway patency caused by stenosis (Murgu & Colt, 2006). Surgery is usually the preferred treatment; however, when the clinical status of the patient permits, stenting provides a reliable alternative in selected cases such as tracheal reconstruction surgeries to prevent airway collapse or to stabilize the reconstructed airway which helps to improve quality of life in non-surgical patients (Stamenkovic, Hierner, De Leyn, & Delaere, 2007). Patients with expiratory central airway collapse often have debilitating dyspnea, cough, inability to clear secretions, and even respiratory failure requiring mechanical ventilation (Collard, Freitag, Reynaert, Rodenstein, & Francis, 1996; Nuutinen, 1977).

The current airway stents technology are either constructed of silicone (Dumon, 1990) or expandable metallic stent made of nickel and titanium alloy (Wood, 2001). The silicone stents are well established in the treatment of stenoses resulting from the intraluminal ingrowth of tumors or granulation tissue while the expandable metallic airway stents are most often used in patients with airway stenosis caused by extrinsic tumoral compression. Both the silicone and expandable metallic stents have different advantages and disadvantages shown in Table 1 (Wood, 2001), which should be considered when the physician chooses the most appropriate

stent for an individual patient. However, the ideal airway stent that combines the advantages of silicone and metallic stents has not yet been developed.

Table 1

Differences between silicone and expandable metallic stents (Wood, 2001)

Silicone	Expandable metal
Removable	Permanent
Able to be dislodged	Stable placement
Adjustable	Difficult adjustment
No epithelialization	Epithelialization
Difficult placement	Easy delivery
Require general anesthesia	Require local anesthesia
No tissue ingrowth	Tissue (tumor) ingrowth
Unreactive	Granulation formation
Can disturb mucociliary clearance	Better clearance mucociliary secretion
Rigid bronchoscopy	Flexible bronchoscopy

The advantages of metallic stents over silicone stents include; simpler insertion and fixation. The metallic stents also have a high internal-to-external diameter ratio and provide better clearance of secretion. However, metallic stents can cause granulation formation where tissues grow through stent interstices causing the stent to be covered by epithelium. This makes the metallic stents not easily removable and therefore may require an open surgery. It is also recommended that the metallic stents should not be used in children because it may be necessary to exchange existing stents for larger ones as they grow.

However, biodegradable metallic stents made of magnesium alloy seems to be a promising material for use in the airway since it offers certain theoretical benefits such as non-toxicity, less irritation on tissues, and high anti-infection capability when compared to the currently available for clinical use. The extraction of the bioabsorbable stent will be unnecessary and the normal airway will be preserved after stent resorption thereby eliminating the need for additional invasive procedures, reducing healthcare expenses and spares the patient the pain of multiple procedures used to implant and later remove the implant (Witte, 2010b). Thus, the development of biodegradable stents, which can fulfill its mission and step away, is the logical approach (Colombo & Karvouni, 2000; Erne, Schier, & Resink, 2006).

In order to fully understand the purpose of airway stenting, it is vital to have some familiarity with the anatomy of the trachea and the main characteristics of tracheal stenosis affecting the airway including the most common causes.

1.1.1 Anatomy of the trachea. The trachea is comprised of 18 to 22 C-shaped rings of hyaline cartilage anteriorly located, whose ends are posteriorly connected by trachealis muscles. Figure 1 (a) illustrates the trachea and the main bronchi. It functions as a conduit for air and clearance of secretions (Grillo, Donahue, Mathisen, Wain, & Wright, 1995). The length goes from 9 to 12 cm in adults, measured from the lower border of cricoid cartilage down to carina where it divides to left and right bronchi. The average laterolateral diameter is between 1.3 and 2.2 cm (Grillo, et al., 1995; Webb, Elicker, & Webb, 2000).

The trachea is composed of 4 layers as shown in Figure 1 (b). The inner layer is the mucosa, which is composed of a pseudostratified columnar epithelium containing ciliated cells and goblet cells. The second layer is the submucosa, which is composed of connective tissue ranging in density from loose to dense irregular. The cartilaginous layer contains C-shaped

rings of hyaline cartilage and facilitates smooth movement of the joints. The outermost layer is the adventitia, which is an outermost layer and contains the cartilaginous rings interconnected by connective tissue.

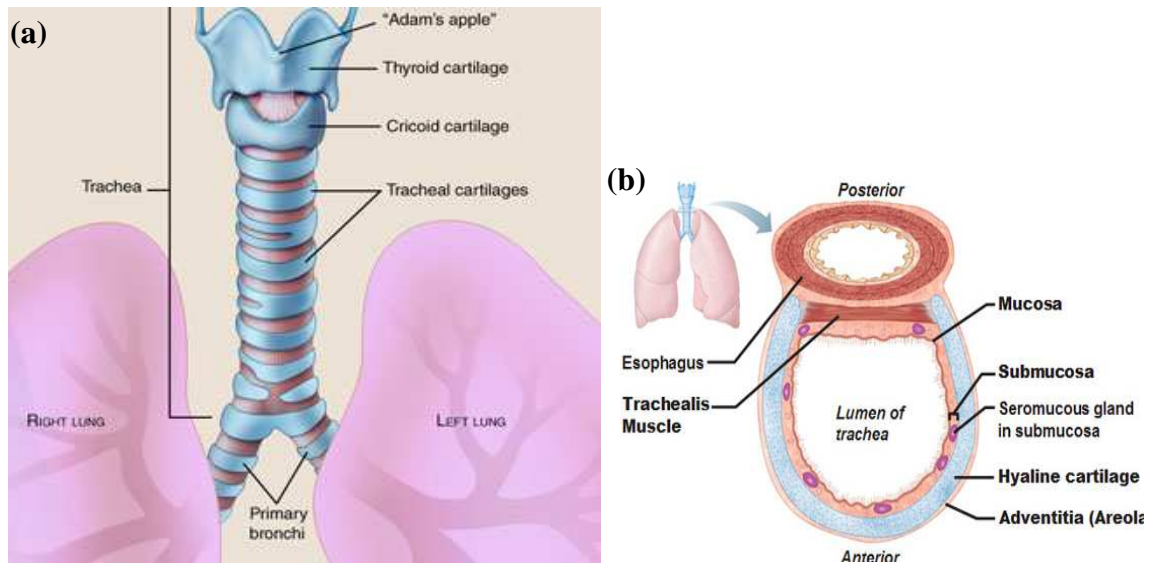


Figure 1. Anatomy of Trachea (a) Trachea and main bronchi (b) Schematic view of the axial cross-section (Source: WebMD.com).

1.1.2 Tracheal stenosis. Tracheal stenosis is defined as narrowing of the central airway due to loss of soft tissue and cartilage support along the trachea. Despite being relatively rare, this condition can be life threatening with treatment including surgery or the use of stents (Spittle & McCluskey, 2000). The most common cause of tracheal stenosis is trauma, specifically internal trauma, usually caused by intubation (Lee, 2008). Other potential causes of tracheal stenosis, includes inflammatory diseases, benign or malignant neoplastic conditions, and extrinsic pressure (Grillo, et al., 1995). Typical symptoms of tracheal stenosis include shortness of breath, coughing, and stridor (Elliott et al., 2003). The narrowing may be seen in various different shapes which are usually associated with its causes (Lee, 2008; Webb, et al., 2000).

CHAPTER 2

Literature Review

2.1 Airway Surface Liquid Overview

During normal respiration, thousands of bacteria and other airborne irritants are inhaled in the airway. Despite this constant intake of pathogens, the body is able to maintain sterility in the airways due to the fluid that covers the surface of conducting airways referred to as the Airway Surface Liquid (ASL). ASL plays a critical role in the defense mechanisms of the lungs against microbial and other environmental threats (Joris, Dab, & Quinton, 1993). It possesses a mucus component that traps inhaled particles; and a periciliary liquid layer (PCL) that keeps mucus at an optimum distance from the underlying epithelia, through which the microorganisms can be expelled in the flow of mucus of approximately $60 \mu\text{m/s}$ driven by the beating of epithelial cilia from the airways illustrated in Figure 2 (Knowles & Boucher, 2002; Tarran, Grubb, Gatzky, Davis, & Boucher, 2001).

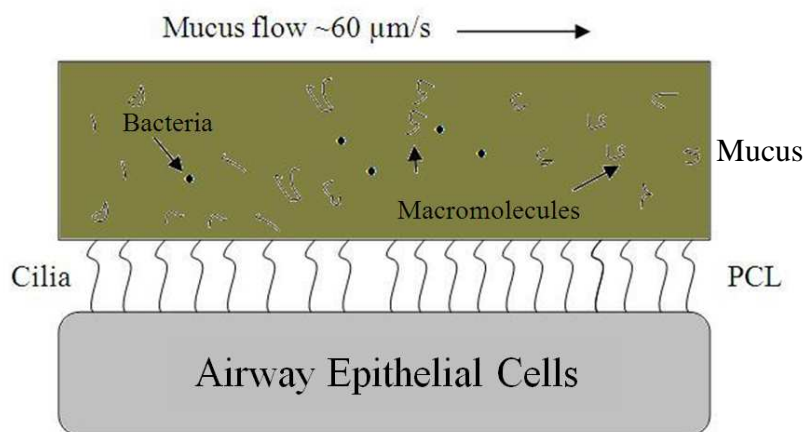


Figure 2. Epithelial cells, Cilia and Mucus layer illustrating defense mechanisms in the airway.

In normal airways, the PCL approximates the length of the outstretched cilia which is $7 \mu\text{m}$, whereas the mucus layer varies considerably in height from $7 - 70 \mu\text{m}$ (Jayaraman, Song,

Vetrivel, Shankar, & Verkman, 2001; Winters & Yeates, 1997). ASL also contains antibacterial agents (e.g., lysozyme and lactoferrin), and migratory cells such as neutrophils and macrophages (Allen, Hutton, Pearson, & Sellers, 1984; Knowles & Boucher, 2002).

2.2 Components in the Airway Lining

2.2.1 Ionic and chemical composition in the airway. The volume, ionic composition, and pH of the ASL are key physiological parameters that are related to airway hydration, reactivity, and antimicrobial activity (Jayaraman, et al., 2001). These parameters are also important in the physiology of Cystic Fibrosis (CF) which is a disease caused by a defective gene characterized by abnormal transport of $[\text{Na}^+]$ and $[\text{Cl}^-]$ across the epithelium, causing the body to produce abnormally thick and sticky mucus. The composition of ASL may also depend on secretion from airway glands, ion transport across the surface epithelium and goblet cell discharge (Widdicombe, 2002).

The surface of the airway lining layer is covered by a liquid that contains mucin macromolecules, electrolytes, and water. The ASL from a healthy airway contains $[\text{Na}^+]$, $[\text{Cl}^-]$ and K^+ with steep ion gradients existing across normal airway epithelia which must be regulated and maintained by active electrolyte transport processes of airway epithelia (Joris, et al., 1993). Water moves into the airway lumen in response to active Cl^- secretion across the epithelia of the tracheal surface and of submucosal glands. Active absorption of Na^+ across the surface epithelium serves to remove liquid. These active ion transport processes move liquid by generating local osmotic gradients across the epithelium (Diamond, 1979).

2.2.2 Mucus and mucin role in the airway. Mucus is a complex viscous adherent secretion synthesized by specialized goblet cells in the epithelium that lines the airway. It is primarily composed of approximately 95% water, ions, lung secretions and proteins (Allen, et

al., 1984). Airway mucus maintains hydration in the airway, it acts as a form of barrier to pathogens, bacteria and contributes to the innate defensive system in mucosal immunology and as a permeable gel layer for the exchange of gases and nutrients with the underlying epithelium (Allen, et al., 1984; Jeffery & Li, 1997; Tabak, 1995). Mucus is the first barrier with which nutrients and enteric drugs must interact and diffuse through, in order to be absorbed and gain access to the circulatory system and their target end organs.

The major macromolecular constituents of mucus are the mucin glycoprotein (Thornton, Rousseau, & McGuckin, 2008). Mucins are high-molecular weight glycoproteins ranging from 200kD to 20-40 MDa (Offner & Troxler, 2000) and are expressed by the epithelial cells and endothelial cells (Levine et al., 1987). Mucins are present as membrane bound or secreted mucins with approximately 80% content of carbohydrate. Mucins structure consist of tandemly repeating amino acids rich in serine and threonine, which are the site for O-linked glycosylation (Rose & Voynow, 2006). Mucin is responsible for viscoelastic properties of the secretions, providing protection for the exposed delicate epithelial surfaces from microbial and physical injuries. They also produce certain enzymes that are responsible for the host intestinal defensive mechanism which prevents many microbial diseases (Satoh et al., 2000).

2.2.3 Airway stent/tissue interface. In order to have a successful and effective airway stent, it is vital to understand the interface between the device placed in the airway and the underlying tissue or environment around the implant. Both the self-expandable metallic stent and the silicone stents experience various problems with the underlying tissues after placement in the airway. The most common problem associated with self-expandable metallic stents is granulation tissue formation, mucus plugging and inflammatory cells (Gottlieb et al., 2009). The mechanism of granulation tissue formation involves the interaction of the metal with airway tissue which

causes excessive growth of healing tissue around the wire to cause blockage of the stent. Similarly Bjarnason et al. reported the effects of placing a metal stent in pig trachea which resulted in retention of secretions or plugs of mucus and secondary infection (Bjarnason et al., 1999). Another problem associated with the metallic stent is the shearing forces at the stent-mucosal interface created by the differential motion of the stent relative to the airway contribute to the constant stimulation of the airway mucosa, leading to reactive granulation tissue (Burningham, Wax, Andersen, Everts, & Cohen, 2002).

Magnesium alloys have a potential to be used as a biodegradable tracheal stent because of their attractive properties such as low density, high strength-to-mass ratio and good damping characteristics (Tan, Soutar, Annergren, & Liu, 2005; Witte, 2010a). Magnesium is essential to human metabolism and is naturally found in bone tissue; therefore released ions are nontoxic to the human body. The current metallic tracheal stents may not be used in children because they are still growing therefore exchanging the existing stents are required. Thus a magnesium airway implant can gradually be dissolved and excreted hence the extraction of the implants will be unnecessary. Therefore, it is intriguing to evaluate the dynamics of metallic airway stents and components of airway surface lining fluid interactions.

2.3 Historical Background on Magnesium

Although Joseph Black discovered magnesia in 1754, it was not until 1808 when Humphrey Davy demonstrated magnesia was the oxide of a new metal using electrolytic splitting, but it was first industrially produced only 78 years later. Michael Faraday later enabled the production of Mg metal by electrolysis of fused anhydrous $MgCl_2$ in 1833 (Witte, 2010a). The production of commercial magnesium began in 1852 in Germany, using a modification of Bunsen's cell and then followed by America during World War I. Magnesium

was used mainly for weapon-manufacturing as it burns hot and fast. It was, however, only during the World War II in 1939 when the Germans and later the Americans started using magnesium alloy for aircraft construction and other military applications, exploiting the low density of magnesium (Chino, Kado, & Mabuchi, 2008; Nguyen, Gupta, & Srivatsan, 2009; Prasad, Rao, & Gupta, 2009). From this first industrial production until the Second World War the amount of magnesium annual production increased from nearly 10 to 235,000 tons in 1944, only to fall again in the late 1940s (Heublein et al., 2003).

Research and development of magnesium alloys significantly declined after the 1960's as a result of an unfavorable price differential between magnesium and aluminum, and magnesium alloys were no longer needed to support war activities. Today, major automotive makers are researching applications of magnesium alloys in engines and car parts in order to reduce the weight and environmental impact due to gas emission, in accordance with the requirements for a more sustainable use of natural resources and controlled environmental impact (Mordike & Ebert, 2001). Magnesium alloys are also widely used for manufacturing of mobile phones, laptop computers, cameras, and other electronic components owing to their excellent resistance to electromagnetic radiation (Goh, Wei, Lee, & Gupta, 2006; Han, Hu, Northwood, & Li, 2008; Hassan & Gupta, 2003).

2.4 Magnesium as a Biodegradable Implant Material

Magnesium is the lightest of all the engineering metals, having a density of 1.7 g/cm^3 . It is 35% lighter than aluminum which has a density of 2.7 g/cm^3 and over four times lighter than steel which is 7.86 g/cm^3 (Zucchi, Frignani, Grassi, Balbo, & Trabanelli, 2008). The physical and mechanical properties of magnesium make it quite suitable as a biodegradable metal implant for both orthopedic and stent application (Staiger, Pietak, Huadmai, & Dias, 2006). Table 2

compares magnesium to the natural bone and other engineering materials used as implants. The difference in elastic modulus of the other engineering materials corresponding value for natural bone varies which may lead to stress shielding effect between implant and bone of the injured bone since it will deprive the bone of the normal stress compromising the whole healing process as well as the implant stability (Winzer et al., 2005; E. L. Zhang, Yin, Xu, Yang, & Yang, 2009).

Table 2

Mechanical properties of Magnesium alloy compared to Natural Bone and other engineering materials (Staiger, et al., 2006)

Properties	Natural bone	Magnesium	Ti alloy	Co-Cr alloy	Stainless steel	Nitinol
Density (g/cm ³)	1.8-2.1	1.74-2.0	4.4-4.5	8.3-9.2	7.9-8.1	6.45
Elastic modulus (GPa)	3-20	41-45	110-117	200-230	189-205	28-40
Compressive yield strength (MPa)	130-180	65-100	758-1117	450-1000	170-310	70-140
Fracture toughness (MPam ^{1/2})	3-6	15-40	55-115	N/A	50-200	N/A

Because of their low density and good mechanical properties combination, magnesium alloys are interesting candidate for biodegradable implants. Magnesium alloys provide advantages when used as structural materials, because of their high strength-to-weight ratio, specific rigidity, good damping characteristics, and castability, which makes them applicable in various fields of modern engineering (Tan, et al., 2005). Magnesium is the fourth most common mineral salt in the human body and the second most common intracellular cation Mg²⁺ (Dube &

Granry, 2003). It's also a vital element involved in several metabolic and biological mechanisms (G. L. Song & Song, 2007) and is mainly present in the bone, muscle and soft tissues.

As early as in 1906 Lambotte applied magnesium as a degradable implant material for the fixation of bone fractures (Cao & Kou, 2006). He used pure magnesium plates in combination with gold-coated steel nails for the fixation of a fractured lower leg. However, due to galvanic corrosion, the Mg plate degraded fast and it dissolved within 8 days with a large amount of gas observed beneath the skin. Despite this set-back he concluded that magnesium was resorbable in the body and further research in the area has been undertaken since then in both animals and humans using different alloys (Cao & Kou, 2006; Djurdjevic & Schmid-Fetzer, 2006; Riemelmoser et al., 2007) mostly *in vitro* (Liu et al., 2010; Witte et al., 2006), but also *in vivo* studies (Witte et al., 2005; Zreiqat et al., 2002).

In general, the use of degradable implants reduces the need for a second operation for implant removal, which saves money to the health system besides being beneficial to the patient. This is particularly important for pediatric cases because the body is still changing and growing which thus requires the permanent implants to match the growth. Additionally, degradable implants also stimulate the damaged tissue as a result of a gradual load transfer from the implant to the tissue (Witte, 2010a). However, the optimal degradation performance of a biodegradable implant must be controlled to ensure the total mechanical integrity of the tissue as well as biocompatibility by delaying the formation of degradation products. For these reasons, a magnesium implant resuming all the advantages mentioned, make it a good material selection for use as a biodegradable implant.

2.5 Corrosion of Magnesium

Corrosion was defined in 1946, by The American Electrochemical Society as “the destruction of a metal by chemical or electrochemical reaction with its environment”. Corrosion occurs due to the metals spontaneous need to revert to a more stable form as it is found in nature (Jacobs, Gilbert, & Urban, 1998). Magnesium corrosion is attributed to the high oxidative corrosion rates due to its strong thermodynamic tendency to oxidize. It is generally known to degrade in aqueous environments via an electrochemical reaction which produces magnesium hydroxide and hydrogen gas. The general anodic and cathodic reactions occurring on a magnesium anode can be expressed by reactions (2-1) and (2-2), respectively.

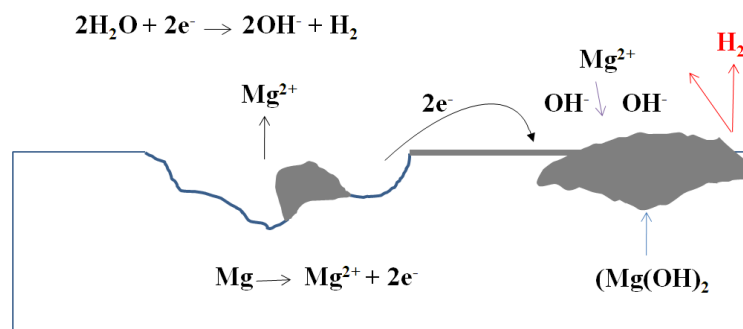
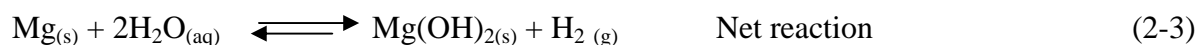


Figure 3. Reactions between magnesium alloy and aqueous environment.

These processes are illustrated on Figure 3. The prime corrosion product formed is magnesium hydroxide however different environments will lead to further types of corrosion products, e.g. carbonates when in the presence of carbonic acid or CO_2 in water or sulphates when in the presence of diluted sulphuric acid or sulphur containing contaminants. From the analysis of the previous equations it can be observed that magnesium corrosion is not

considerably dependent on the environment's oxygen concentration (G. Song, Atrens, Stjohn, Nairn, & Li, 1997; G. L. Song & Song, 2007) .

2.5.1 Negative difference effect (NDE). The NDE is a very strange phenomenon found in magnesium and its alloy due to the strong hydrogen evolution and the rate of this reaction has been found to increase with the increase in the anodic polarization. However, this phenomenon is still not well understood. Due to this effect, predicting the corrosion behavior of magnesium becomes challenging because it does not follow the normal corrosion behavior as other metals such as copper, iron and steels. Typically, anodic and cathodic reaction models the behavior of all electrochemical corrosion processes meaning as current density increases, the anodic reaction rate increases and the cathodic reaction rate decreases. An anodic increase of the applied potential causes an increase in anodic dissolution rate, while the cathodic site decreases in hydrogen evolution (G. L. Song & Atrens, 1999).

Song et. al reports the breakdown of a protective film where the hydrogen evolution is attributed to the presence of film-free regions inside the pits (G. L. Song & Atrens, 1999). Therefore the increase of film-free surface with anodic polarization must be overcompensated by the decrease of the cathodic current density by anodic polarization. The dissolution of Mg undergoes two reactions as shown in equations (2-4) and (2-5). In this model, the NDE is due to the increase of the Mg^+ concentration by the anodic polarization, which accelerates the hydrogen evolution (Przylusk.J & Palka, 1970).



2.5.2 The pourbaix diagram for magnesium corrosion. The behavior of magnesium in water solutions at room temperature is shown in the Pourbaix diagram in Figure 4 and it

highlights the theoretical areas of corrosion, passivation, and immunity. The Pourbaix diagram provides a means for visualizing the effects of potential and pH on the thermodynamic regions of magnesium corrosion and stability. At physiological pH = 7.4, magnesium's corrosion potential corresponds to the region where hydrogen is stable. Therefore, magnesium corrodes in physiological environments to produce magnesium ions ($\text{Mg}^+/\text{Mg}^{2+}$) and hydrogen gas. Hydrogen evolution is the dominant reduction reaction, so dissolved oxygen does not play a significant role in Mg corrosion (Makar & Kruger, 1993). Corrosion is strongly deterred above pH = 11, the equilibrium pH for $\text{Mg}(\text{OH})_2$, which is assumed to be the major constituent of the passive film.

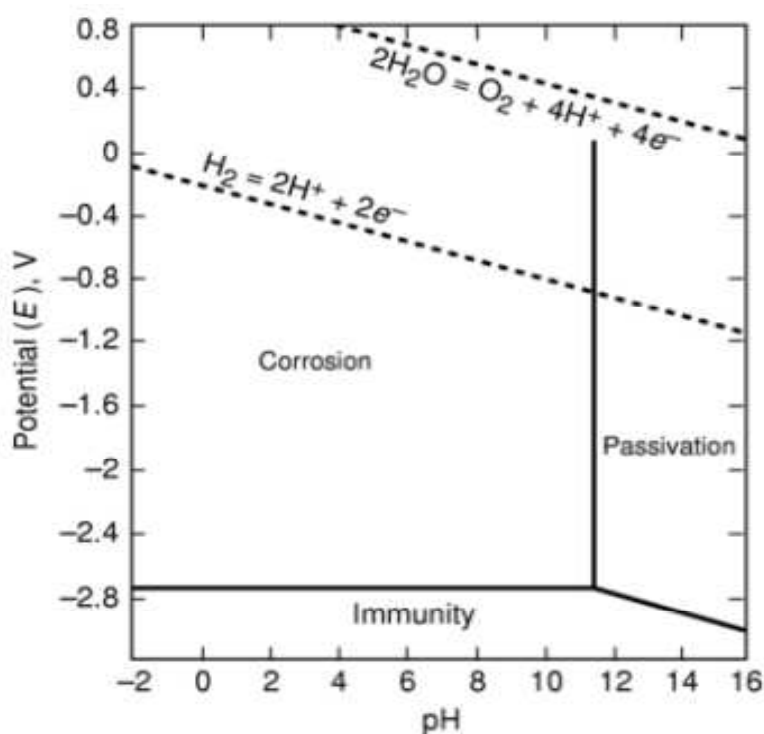


Figure 4. Magnesium's pourbaix diagram in H_2O (Makar and Kruger 1993).

The electrochemical standard potential of the metal is $E_0 = -2.37\text{V}$. Within the human body magnesium degrades according to the reactions in equation 2-3, leaving hydrogen gas bubbles and magnesium hydroxide. These hydrogen bubbles may cause physical problems such

as blocking the blood stream or separating the tissues leading to necrosis in the vicinity of an implant if large volumes are formed in a short period of time. If the hydrogen bubbles are formed slowly enough they will have time to diffuse into the tissue. The magnesium hydroxides form on the surface of the implant, alkalizing the surroundings. When reaching pH above 11, this can temporarily protect the metal, according to the Pourbaix diagram.

2.5.3 Galvanic corrosion. Galvanic corrosion is the corrosion that takes place when different metals or alloys are coupled together in the presence of an electrolyte. This type of corrosion is observed when heavy localized corrosion of the magnesium matrix is detected close to cathodic areas (G. L. Song & Atrens, 1999). A distinction between external and internal galvanic corrosion can be established depending on whether the Mg is in contact with a nobler metal or whether there exist cathodic second phases or impurities in the matrix, respectively. The position of the dissimilar metals in the galvanic series, the conductivity of the electrolyte and the ratio of the surface areas of the dissimilar metals are factors which affect the severity of the corrosion. Magnesium is the least noble of the metals with a potential of -1.7V, meaning that magnesium is very susceptible to galvanic corrosion (Zeng et al., 2006).

According to Ohm's law, the galvanic corrosion current can be expressed by:

$$I_{\text{corr}} = \frac{(E_{\text{p-c}} - E_{\text{p-Mg}})}{(R_{\text{e}} + R_{\text{m}})}$$

$E_{\text{p-c}}$ – Polarized potentials for the cathode material

$E_{\text{p-Mg}}$ – Polarized potentials for the magnesium

R_{e} – Electrolyte resistance

R_{m} – Resistance in the metal-metal contact between anode and cathode

From the equation, galvanic corrosion current can be minimized by either minimizing the potential difference between magnesium and the cathode or maximizing the resistance of the

circuit. Metals with low hydrogen overvoltage such as copper, nickel, and iron may have a negative effect on the degradation performance of magnesium even in minor quantities, because their low solubility in Mg can ease the development of micro-galvanic cells and cause internal galvanic corrosion (G. L. Song & Atrens, 1999). On the other hand, metals with high hydrogen overvoltage are much less damaging. Additionally, the secondary phases present in the Mg alloy can also behave as cathodes leading to dissolution of the Mg matrix adjacent to them. Grain boundaries also represent cathodic regions to the anodic grain interior. In this case, corrosion tends to concentrate in the adjacent zone to the grain boundary until the eventual undercut and fallout of the grain (G. L. Song & Atrens, 2003).

2.5.4 Pitting corrosion. Pitting corrosion is the most common type of localized corrosion in which pits form from dissolution of the specific areas of the material surface which leads to creation of small holes in the metal. Pitting corrosion occurs due to the depassivation of a small area, which becomes anodic while an unknown but potentially vast area becomes cathodic, leading to very localized galvanic corrosion. Magnesium mostly undergoes pitting corrosion in the presence of chloride ions in non-oxidizing medium (G. L. Song & Atrens, 1999). The initiation of pits starts at defects of the passive film such as pores and scratches which are anodic compared to their vicinity and result in the dissolution of metal.

2.5.5 Stress cracking corrosion (SCC). Since the Mg implant being used as a biomedical implant will be under load, corrosion under stress conditions must be addressed. Stress corrosion cracking (SCC) is characterized by the growth of cracks in a material that is exposed to a corrosive environment and stress due to mechanical loading or a susceptible alloy. The driving force of this type of corrosion is related to the potential difference between the grain boundaries and the bulk material. In certain corrosive environments, SCC usually leads to an

unexpected quick failure of the sample, especially when subjected to a tensile stress. It usually progresses rapidly and is more common among alloys than pure metals. Al and Zn containing alloys promote SCC whereas alloys containing zirconium and rare earth are free from SCC (Winzer, et al., 2005).

Studies regarding this type of corrosion claimed that, depending on the medium (Miller, 1993), chemical composition and structure of the Mg alloy, intergranular and transgranular SCC was observed (Winzer, et al., 2005). Intergranular cracking is continuous and involves only electrochemical processes where dissolution of the matrix adjacent to the grain boundaries is observed and the consequent stress pulls the metal apart. On the other hand, transgranular cracking is found to be discontinuous and comprising mechanical and electrochemical processes. Pits and notches caused by electrochemical processes result in brittle fractures, cracking after high stress tensions. The crack stops at barriers, for example grain boundaries, and continues once the obstruction is removed by electrochemical attack. Hydrogen embrittlement has also been reported to be responsible for SCC (Winzer, et al., 2005).

2.6 Surface Treatment of Magnesium Alloy

In order to enhance the corrosion resistance of magnesium based implants to avoid fast degradation in the human body, the magnesium alloy need to be coated to maintain their mechanical integrity. There are many ways to enhance the corrosion resistance of magnesium alloys in a way that inhibits electric contact between the substrate and avoid galvanic corrosion, as described in literature (Chiu, Wong, Cheng, & Man, 2007; Gray & Luan, 2002; Kuwahara et al., 2000; Thomann et al., 2010). Typical surface modification techniques include physical surface modification, chemical conversion treatment, plasma electrolytic oxidation, electroplating and organic coating. Among these techniques, plasma electrolytic oxidation is one

of the most promising methods for magnesium alloys (Hsiao & Tsai, 2005; Hsiao, Tsung, & Tsai, 2005; Mizutani, Kim, Ichino, & Okido, 2003; Wu et al., 2007). Although plasma electrolytic oxidation treatment is usually more expensive than a chemical surface treatment, it is always selected for application requiring high performance, such as wear resistance and heavy duty paint preparation. In this work, plasma electrolytic oxidation of AZ31 magnesium alloy was the coating choice for the surface treatment method for the magnesium alloy.

2.6.1 Plasma electrolytic oxidation (PEO). It is the most industrially used method for coating magnesium alloys. It is an electrolytic passivation process used to increase the thickness of the natural oxide layer on the surface of the metal parts by applying high voltages usually from 100-500V (Vijh, 1971) on the metal which constitute the anode electrode of the electrical circuit (Y. J. Zhang, Yan, Wang, & Li, 2005). Many studies in the literature are dedicated to understand the properties of these coatings on magnesium substrates resulting in enhanced corrosion and wear resistance (Arrabal, Matykina, Hashimoto, Skeldon, & Thompson, 2009; Ghasemi, Raja, Blawert, Dietzel, & Kainer, 2008; Liang, Srinivasan, Blawert, & Dietzel, 2009, 2010).

In general, the microstructure of PEO coating is composed of an outer porous layer and an inner barrier layer as shown in Figure 5. The composition and quality of the inner barrier layer has a considerable influence on the corrosion resistance of the coating, while the resistance of the outer porous layer is too weak thereby not contributing to a significant corrosion protection of the Mg substrate (Y. J. Zhang, et al., 2005). These micro-pores, acting as transportation passage for the corrosive ions, thereby, corrosive media may rapidly enter onto the barrier layer of PEO coating and so that decrease largely the protectiveness of the PEO coatings (Blawert, Dietzel, Ghali, & Song, 2006; Srinivasan, Liang, Blawert, Stormer, & Dietzel, 2010). Therefore, the outer

layer usually requires a sealing treatment to achieve the necessary performance (Zuo, Zhao, & Zhao, 2003). Preparation process can also produce a good quality of inner barrier layer, and simultaneously, lower the porosity of the porous layer should be helpful to upgrade the corrosion performance of PEO coatings.

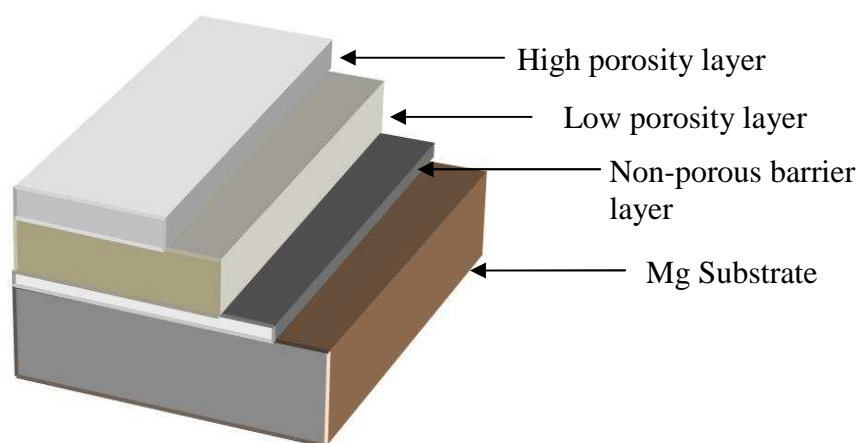


Figure 5. Schematic description of a ceramic coating prepared by the PEO process.

The structures of PEO coating on Mg alloy depend on processing parameters, such as chemical composition of electrolyte, electric parameters, alloy composition of substrate, pretreatment and post treatment, etc. Especially, the chemical composition of the electrolyte exerts a considerable influence on the formation and property of effective oxide layer for Mg alloy (W. Zhang, Tian, Du, Zhang, & Wang, 2011). Therefore, it is important to select proper base electrolyte compositions to improve the compactness and its corrosion resistance on Mg alloys. The most common electrolytic bath contains chemicals such as phosphates, silicates, hydroxides, fluorides in variable concentrations.

2.6.2 Polymer coating (PLGA). Amongst all the biomaterials, application of the biodegradable polymer poly lactic-co-glycolic acid (PLGA) has shown immense potential as a drug delivery carrier and as scaffolds for tissue engineering (Makadia & Siegel, 2011). PLGA is

a copolymer of poly lactic acid (PLA) and poly glycolic acid (PGA). PLGA polymers are physically strong and highly biocompatible and have been extensively studied as delivery vehicles for drugs, proteins and various other macromolecules such as DNA, RNA and peptides (Bouissou, Rouse, Price, & van der Walle, 2006; Jain, 2000). The PLGA films can be used on metallic surfaces to some effect, particularly in stents where sustained delivery of drugs is critical in preventing restenosis and helping prevent cell proliferation in stents (Pan, Tang, Shao, Wang, & Huang, 2007). However, this type of delivery method results in an uncontrolled, usually short, diffusion-like release and can disguise the structure of the metallic implant by applying a uniform layer to the surface (Pan, Tang, Weng, Wang, & Huang, 2007).

In orthopedic applications it has been shown that a micro/nanostructure is very important for bone growth, even on the surface of a PLGA film (Smith et al., 2007). An alternate method of sustained drug delivery would be to employ a particulate formulation of PLGA. By doing so, it would allow for a controlled, tunable drug release whilst preserving or enhancing the underlying texture of the implant surface, thus also promoting cellular interactions. The PLGA degradation and the drug release rate can be accelerated by greater hydrophilicity, increase in chemical interactions among the hydrolytic groups, less crystallinity and larger volume to surface ratio of the device (Park, 1994; Schliecker, Schmidt, Fuchs, Wombacher, & Kissel, 2003; Tsuji, Mizuno, & Ikada, 2000). All of these factors should be taken into consideration in order to tune the degradation and drug release mechanism for desired application.

2.7 Problem Statement

The present work aims to investigate the *in vitro* corrosion behavior of the AZ31 Mg alloy in order to provide degradation information for future *in vivo* study while aiming to reinforce the progress of biodegradable magnesium implants. This was performed by evaluating

the different concentrations of carbonate ions and porcine stomach mucin in a physiological environment to determine their effect on the corrosion rate on Mg alloy.

Hypothesis:

- i) Addition of carbonate ions in the simulated physiological solution will accelerate general corrosion rate of the magnesium alloy.
- ii) Addition of porcine stomach mucin in the test solution decreased the corrosion rate of the magnesium by adsorption on the solid surface thereby reducing the formation of corrosion products forming on the surface.

The corrosion resistance of magnesium alloy was evaluated by coating the samples using plasma electrolytic oxidation (PEO) technique to grow protective coatings on the surface. Consequently, a multi-layer coating of both anodized and Poly Lactic-co-Glycolic Acid (PLGA) coatings was investigated to further slow down the initial corrosion rate of the anodized magnesium alloy by sealing the micro-cracks and micro-pores on the outer surface oxide layer effectively.

Cytocompatibility of the magnesium alloy was assessed using porcine tracheal epithelial (PTE) cells to determine the cell responses, in terms of cell morphology and cell adhesion on the different surfaces of the AZ31 Mg alloy including untreated, anodized, multilayer coating of anodized+PLGA and PLGA+Paclitaxel drug were evaluated. The cell adhesion assay was used to analyze the potential of the magnesium alloy to be utilized as biomedical implant studying its non-toxicity and biocompatibility.

CHAPTER 3

Materials and Methods

This study employed multiple techniques to characterize the corrosion rate of AZ31B magnesium alloy as a biomaterial. Evaluation of corrosion behavior was performed using electrochemical testing and immersion testing in a Gamble solution mimicking the biological environment. The morphological characterization of the samples was performed using Micro-CT and SEM and chemical compositions were identified using EDX and XRD analysis on corrosion products after immersion tests. Cell adhesion assay was performed using porcine tracheal epithelial (PTE) cells to determine biocompatibility of Mg alloys. Analysis of the cell culture samples was performed by SEM observation, after ion beam coating, following fixation and dehydration.

3.1 Sample

AZ31 Magnesium alloys with nominal composition of 2.5-3.5 wt % Al, 0.6-1.4 wt % Zn and balance Mg was tested in this study. The samples were obtained from GoodFellow Corp., Oakdale, PA. For the immersion test samples, the cylindrical specimens were cut with diameter of 6.35 mm and a height of 2 mm, which were polished up to 1200 grit of silicone carbide sand paper, using water as a lubricant and rinsed with acetone and distilled water sequentially and dried. The electrochemical samples were embedded into epoxy resin to leave a working area of 0.785cm^2 , and electrical connection provided through a copper wire. In order to ensure the same surface roughness of samples, the exposed surface was also polished to 1200 grit of silicone carbide sand paper.

3.2 Solution

Both electrochemical and immersion tests were carried in Gamble solution also referred to as simulated lung fluid (SLF), as shown in Table 2, intended to simulate the interstitial conditions in the lung (Marques, Loebenberg, & Almukainzi, 2011). When preparing Gamble solution, the components were added in order presented in the Table 3 to avoid salt precipitation. Citrate was used instead of proteins to avoid foaming and acetate instead of organic acids. The pH of solution was adjusted using 0.1M HCl and 0.1M NaOH to obtain a pH of 7.4.

Table 3

Concentrations of chemicals used to prepare Gamble solution or SLF (Marques, et al., 2011)

Gamble Solution Composition	Concentration
Magnesium Chloride	0.095 g/l
Sodium Chloride	6.019 g/l
Potassium Chloride	0.298 g/l
Disodium Hydrogen Phosphate	0.126 g/l
Sodium Sulfate	0.063 g/l
Calcium Chloride Dihydrate	0.368 g/l
Sodium Acetate	0.574 g/l
Sodium Hydrogen carbonate	2.604 g/l
Sodium Citrate Dihydrate	0.097 g/l

The concentration of sodium bicarbonate was changed in order to study the effect of the different concentrations of carbonate ions in a physiological environment and evaluate the effect on corrosion rate of Mg. The different carbonate ions concentrations tested included 0 g/l, 1 g/l,

2.6g/l and 4g/l. Porcine stomach mucin was later added in the SLF to mimic the epithelial surface along the trachea. The different mucin concentrations tested included 0 g/l, 0.03 g/l and 0.1 g/l. In total, there were 12 test solutions. Table 4, shows the different concentrations of both porcine stomach mucin and NaHCO₃ in Gamble solution. The different concentrations of both carbonate ions and mucin was studied to identify the effect of both ions and proteins on the corrosion of magnesium alloy.

Table 4

Test solutions with different concentrations of mucin and sodium carbonate (NaHCO₃) in Gamble solution

Solution No.	Concentrations of NaHCO ₃	Mucin Concentrations
Test Solution 1	0 g/l NaHCO ₃	0 g/l Mucin
Test Solution 2	1 g/l NaHCO ₃	0 g/l Mucin
Test Solution 3	2.6 g/l NaHCO ₃	0 g/l Mucin
Test Solution 4	4 g/l NaHCO ₃	0 g/l Mucin
Test Solution 5	0 g/l NaHCO ₃	0.03 g/l Mucin
Test Solution 6	1 g/l NaHCO ₃	0.03 g/l Mucin
Test Solution 7	2.6 g/l NaHCO ₃	0.03 g/l Mucin
Test Solution 8	4 g/l NaHCO ₃	0.03 g/l Mucin
Test Solution 9	0 g/l NaHCO ₃	0.1 g/l Mucin
Test Solution 10	1 g/l NaHCO ₃	0.1 g/l Mucin
Test Solution 11	2.6 g/l NaHCO ₃	0.1 g/l Mucin
Test Solution 12	4 g/l NaHCO ₃	0.1 g/l Mucin

3.3 Porcine Stomach Mucin

Type III partially purified porcine stomach mucin was purchased from Sigma-Aldrich, St. Louis, MO (Cat #. M1778). The mucin was diluted into the Gamble solution to create an *in vitro* model of the epithelial mucus surfaces mimicking the epithelial surface along the trachea to help understand the degradation mechanism of magnesium alloy in mucin. The three different concentrations were 0 g/l, 0.03 g/l and 0.1 g/l as illustrated in Table 4. The test solution was prepared using distilled water and was continuously stirred until a homogeneous solution was obtained.

3.4 Corrosion Characterization



Figure 6. Electrochemical testing setup.

The corrosion characterization techniques used included immersion test, electrochemical tests as well as monitoring of the pH change. Electrochemical tests were carried out using a Gamry Ref 600 with the typical three electrode system and a water bath set up at 37°C. Figure 6 shows the electrochemical setup used in the electrochemical tests. The three electrodes constituted of the working electrode (WE), reference electrode (RE) and the counter electrode (CE). RE measures the working electrode potential and has a constant electrochemical potential

as long as no current flows through it. The WE is the electrode where the current is measured while CE is a conductor that completes the cell circuit. A water bath set at 37°C was included in the experiment.

3.4.1 pH measurement. The pH value of the test solution has a tremendous effect on the corrosion rate of magnesium (Inoue, Sugahara, Yamamoto, & Tsubakino, 2002). Therefore, the pH of both electrochemical and immersion tests solutions were measured with pH meter (Oakton® pH2100, Eutech instruments, Singapore) before and after the tests to measure the pH variation of the test solutions.

3.4.2 Immersion test. Immersion testing was employed in this research in an effort to expose the degradation behavior of the magnesium alloy in a physiological environment. Cylindrical specimens with a diameter of 6.35 mm and a height of 2 mm were cut from a rod of as drawn AZ31B magnesium alloy, which were polished up to 1200 grit of silicone carbide sand paper. The test was carried out in an isotherm incubator at 37°C for 10 days, the samples were immersed in 250ml Gamble solution and the beakers covered with parafilm to minimize hydrogen evolution and evaporation of the solution. The pH of solutions was adjusted using 0.1M HCl and 0.1M NaOH to 7.4 ± 0.05 before the immersion test and measured after the immersion test to determine the corrosion rate. Due to the pH increase during the test, the solutions were changed every day to minimize the pH impact.

3.4.3 Open circuit potential (OCP). The open circuit potential measurement started 1 min after the sample was immersed in the test solution. The data acquisition frequency was 0.5 Hz. The potential vs. time response data was collected for a period of 24 hours for each test involving the different test solutions tested. The samples exhibited stable curves after 3 to 5 h as

the surface of the sample became passivated. Each test was repeated 3 times to ensure the reproducibility of the results.

3.4.4 Electrochemical impedance spectroscopy (EIS). The frequency range for EIS measurements was 100 kHz to 10 mHz, with seven measurement points per decade. Measurements were made at the OCP with rms amplitude of 10 mV. The initial OCP delay was 1 min. The test was repeated 3 times to ensure the reproducibility of the results.

3.4.5 Linear polarization resistance (LPR). All polarization experiments were performed at 37°C for a period of 24 hours. Linear polarization instrumentation used by Gamry Echem Analyst software converted the current measured to corrosion rate readings in mils per year (mpy). The test was repeated 3 times to ensure the reproducibility of the results.

3.4.6 Potentiodynamic polarization. Potentiodynamic polarization curves were obtained by scanning the potential from -0.2 V/OCP to 1 V/OCP with a scanning rate of 0.5mV/s. The larger anodic scan range was used because we are more interested in the anodic region. After the graphs were generated, Gamry Echem Analyst software was used in order to generate corrosion rates for the samples. To do this, both an anodic and cathodic section of the resulting curve was chosen. The software then used a linear regression to fit the curve to the Butler-Volmer equation, shown below, and to obtain the resulting tafel slopes and corrosion current.

$$I = i_{\text{corr}} \left[e^{\frac{2.3*(E-E_{\text{OC}})}{\beta_a}} - e^{-\frac{2.3*(E-E_{\text{OC}})}{\beta_a}} \right]$$

Where;

I – The measured cell current (Amps)

i_{corr} – The corrosion current (Amps)

E – The electrode potential (Volts)

E_{oc} – The open circuit potential (Volts)

β_a – The anodic tafel slope constant (Volts per decade)

β_c – The cathodic tafel slope constant (Volts per decade)

3.5 Plasma Electrolytic Oxidation (PEO)

In this experiment, the formation of anodic oxide films was performed in 1M sodium hydroxide and 0.1M sodium silicate electrolyte. The solution was prepared from distilled water and was continuously stirred during treatment with a stainless steel rod used as a counter electrode. The PEO coatings were done at different applied voltages in the range of 100V - 500V and current density of 0.020mA cm^{-2} - 0.600mA cm^{-2} and the pulse frequency was between 50Hz - 100Hz using the square waveform as illustrated in Figure 7.

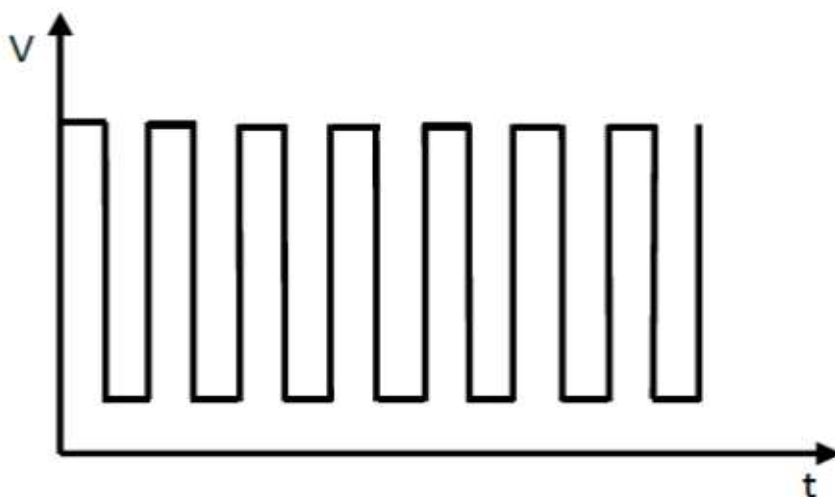


Figure 7. Scheme of square waveform of applied voltage (V) with time (t).

The experiment was performed at room temperature and to maintain a uniform distribution of temperature, the bath solution was stirred by a magnetic stirrer in the 1000ml glass container. The anodized sample was rinsed using distilled water and dried. The corrosion resistance of the coated AZ31 was analyzed using electrochemical testing. The plasma electrolytic oxidation experimental setup is shown in Figure 8.

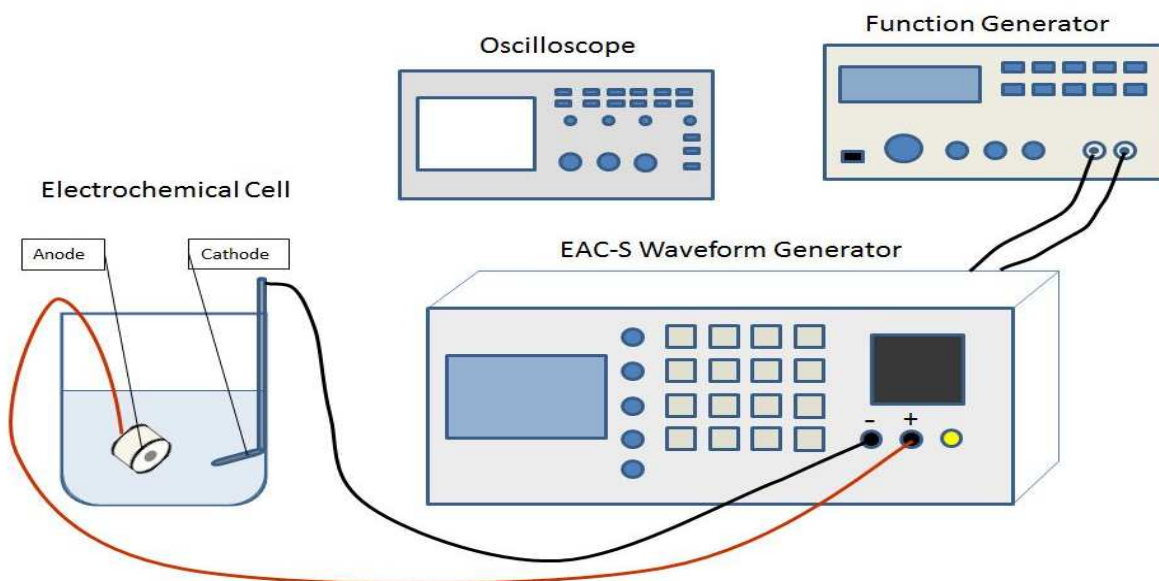


Figure 8. Plasma Electrolytic Oxidation experimental setup.

3.6 Polymer (PLGA) coating

PLGA (poly D,L-lactide-co-glycolide) pellets (PLGA; LA/GA=50/50, Mw 40000-75000) were dissolved in chloroform in order to obtain 5% (w/v) solution. The solution was stirred until a homogenous polymer solution was obtained. Before coating deposition, the samples were polished with waterproof abrasive paper up to 1200 grits, degreased with acetone and rinsed with ethanol and distilled water sequentially, and then followed by blow-drying. The dip coating process was performed by dipping the both the untreated and anodized AZ31 samples into the polymer solution, followed by drying in an oven at 60°C for 10 min. The thickness of the deposited polymer was controlled by the number of dipping between 1 and 5. For this study, three dip coatings were explored for both electrochemical testing and cell adhesion assay.

Polymeric drug delivery system using paclitaxel-loaded PLGA was used to coat cell adhesion assay samples. Paclitaxel of 99.5% purity was purchased from Sigma-Aldrich (USA). The drug release coating was composed of poly (DL-lactide-co-glycolide)/paclitaxel

(PLGA/PTX) layer coated using dip coating. The morphology of the cells attached on the cells was studied using SEM to determine if the cells were affected by the drug release controlled by the degradation of PLGA.

3.7 Cell Adhesion Assay

In this study, the cell adhesion assay involved incubating AZ31 alloys samples generally exhibiting an area of 0.785cm^2 with primary porcine tracheal epithelial cells. The porcine airway epithelial cells were provided by Dr. Jenora Waterman (North Carolina A&T State University, Greensboro, NC). Briefly, frozen porcine tracheal epithelial cells were warmed in a 37°C water bath for 1-2 min. The cells were transferred to pre-warmed media (50:50 mixture of Dulbecco's Modified Eagle Medium (DMEM): Ham's F-12 containing 2% fetal bovine serum (FBS), antibiotics and growth supplements) and pipetted gently to evenly distribute cells. Cell were seeded at a density of 1×10^5 PTE cells/well (in a volume of 0.6 ml media/well) onto AZ31 alloy discs categorized into four test groups: untreated, anodized, untreated+PLGA, and untreated+PLGA+10% Paclitaxel drug coatings. Samples were incubated at 37°C with 5% CO_2 conditioned humidified air, using 24-well (#3526) plates for approximately 12 hours. Following incubation, media was aspirated and the samples were rinsed three times with 1X PBS pH 7.4 to remove non-adherent cells. The attached cells were then fixed in 4% paraformaldehyde and dehydrated using 100% ethanol. Analysis was performed by ion beam coating and SEM observation, following fixation and dehydration.

3.8 Surface Characterization

In this section, introductory surface characterization techniques used in the experimental work is presented. The techniques used included SEM, XRD, EDX analysis, and Micro CT.

3.8.1 Scanning electron microscopy (SEM). In this experiment, Hitachi SU8000 field emission scanning electron microscope was used. It utilizes a raster scan pattern which enables the observation and local characterization of materials' surface topography, chemical composition and crystallography at the micrometer scale. The operating principle of the SEM involves the scan of the sample surface, using a finely focused electron beam, controlling the brightness at each point of the obtained image which is acquired in accordance with the signal emitted by the sample (Hitachi, 2012).

3.8.2 X-ray diffraction (XRD). In this experiment, X-ray diffraction was performed using the Bruker AXS D8 Discover. X-ray diffraction (XRD) is a versatile, non-destructive technique that reveals detailed information about the chemical composition and crystallographic structure of materials. The basic step in X-ray crystallography involves measuring the intensity of the diffracted X-rays at various angles. The different samples after the 10 day immersion test were characterized by XRD to determine the chemical composition of corrosion products formed on the surface. The patterns were later compared with the control sample.

3.8.3 X-ray computed tomography (micro-CT). The surface morphology of the immersion test samples in this experiment was examined using micro-CT (Phoenix Nanotom-MTM, GE sensing & Inspection technologies GmbH, Germany) shown in Figure 9. X-ray computed tomography in non-destructive 3D analysis developed to fulfill the fast growing demand for high resolution and high precision images. It features a fully automated CT scan execution, volume reconstruction and the analysis process. The immersion test samples were analyzed after the 10 days immersion to characterize the 3-D morphology of the corrosion products formed on the surface.



Figure 9. Micro-CT System Nanotom-M at North Carolina A&T State University.

CHAPTER 4

Results and Discussion

4.1 Immersion Tests Results

Figures 30, 31 and 32 in the appendix shows optical images of AZ31B alloy after immersion test (Before Immersion, Day 3 and Day 10 respectively) in Gamble solution with different concentrations of carbonate ions and porcine stomach mucin in the test solutions as illustrated in Table 4. White calcium phosphate was deposited on the surface of the sample immersed in the Gamble solution containing 0 g/l HCO_3^- , 0g/l Mucin. It was observed that the thickness of the precipitate increased as day passed. However, the white calcium phosphate precipitation diminished gradually with the increase of both carbonate ions and mucin glycoproteins in the solutions. The thickness and uniform corrosion products mainly $\text{Mg}(\text{OH})_2$ were formed on the surface of magnesium alloy immersed in solution with carbonate in this study. Xin Y et al. asserted that HCO_3^- ions in solution accelerated initial corrosion of magnesium, but retarded the pitting corrosion and corrosion rate as time lapse since it forms passivation layer consisting of magnesium carbonate (Xin et al., 2007).

4.1.1 pH measurement results. The variation of pH plot during immersion tests is shown in Figure 10. The immersion test was repeated 3 times ($n=3$) for duration of 10 days each and the average values plotted with the error bars showing the minimum and the maximum pH values. From the plot it can be noted that the pH decreased in the test solutions containing 0 g/l HCO_3^- , 0 g/l mucin by -0.4 while the pH of the test solutions containing 0 g/l HCO_3^- , 0.03 g/l mucin and 0g/l HCO_3^- , 0.1 g/l mucin both decreased about -0.3. The pH usually increases during immersion test because OH^- are generated at both anodic and cathodic regions as magnesium is corroded (G. L. Song & Atrens, 2003). However, the pH of solutions was lower in this case

because of the effect or the formation of hydroxyapatite on the sample surface (Barrere et al., 2003; Lindstrom, Johansson, & Svensson, 2003). The process that induces hydrogen ions is shown in equation (4-1). The pH variation without the magnesium sample was also tested to confirm decrease of pH by dissolution of CO₂ in the atmosphere and average of daily decrement was about 0.2.

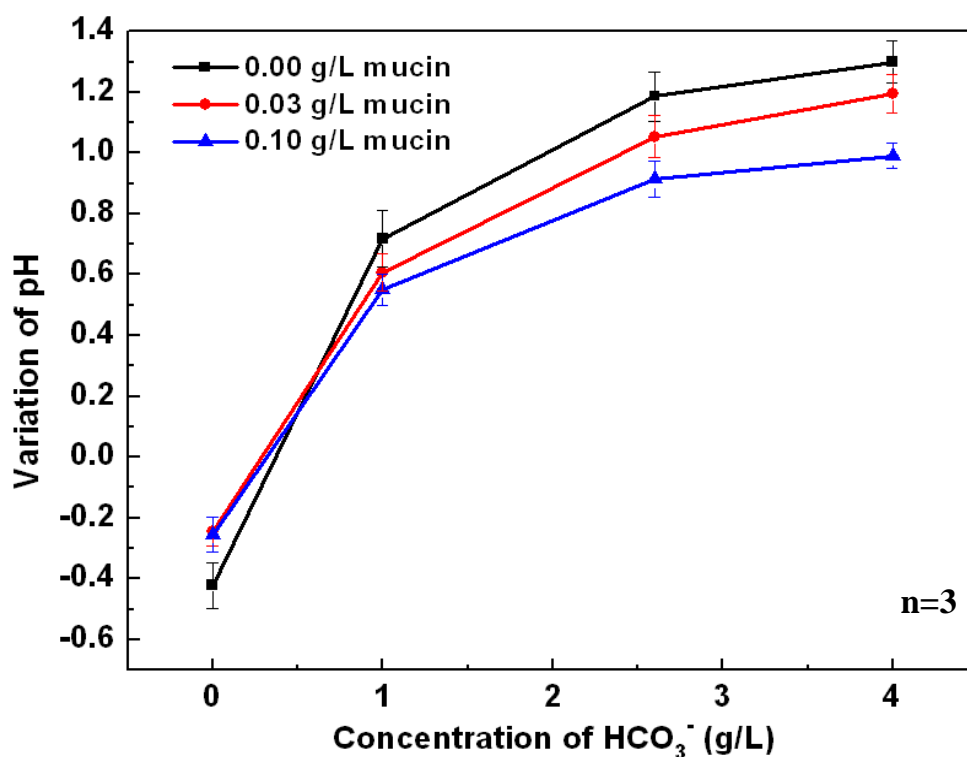


Figure 10. Variation of pH plot on the AZ31 samples showing the effect mucin and HCO₃⁻ increase in Gamble solution.

The addition of bicarbonate ions in the solution showed a substantial increase in the pH. The plot illustrates solutions containing 4 g/l HCO₃⁻, 0 g/l mucin increased by approximately +1.3 which was the highest pH increase from all the solutions tested. This indicated that the corrosion rate of magnesium alloy caused by HCO₃⁻ ions was faster than the formation of hydroxyapatite caused by the calcium and phosphate in solution. Similar results were also

obtained by Xin et al. (Xin, et al., 2007) showing the effect of HCO_3^- ions increase in the corrosion behavior of magnesium in simulated fluid. The solution containing 4 g/l HCO_3^- , 0.1 g/l mucin had a lower increase of pH of about +0.8 compared to 4 g/l HCO_3^- , 0.03 g/l mucin which had +1.2 hence the increase in mucin in the solution lowered the corrosion rates of the samples immersed in the solutions. It is hypothesized that mucin adsorption on the surface of the samples decreases the corrosion rate by reducing the formation of corrosion products on the surface, which explains the low pH with the increase in mucin.

4.1.2 X-ray computed tomography (micro-CT) results. Calcium phosphate was deposited on the surface of the samples immersed in the Gamble solution containing 0 g/l HCO_3^- , 0 g/l mucin and 0 g/l HCO_3^- , 0.03 g/l mucin with pitting corrosion only occurring on the areas where thickened precipitate had fallen off as illustrated in Figure 33 in the appendix. The deposition of calcium phosphate was seen to decrease dramatically on the sample immersed in the 0 g/l HCO_3^- , 0.1 g/l mucin solution. The same phenomenon was observed when there was an increase of HCO_3^- ions in the Gamble solution, which accelerated general corrosion rate of the samples corroded uniformly without severe localized corrosion as shown in Figure 34 in the appendix. Some voids and corrosion products were formed by small pitting corrosion were observed with a thin layer of corrosion product on the surface. As the concentration of HCO_3^- ions increased, the more general corrosion progressed thus increasing the corrosion product thickness, evidenced by the SEM cross-section morphology as shown in Figure 35 in the appendix.

4.1.3 Scanning electron microscope results. SEM images of the surface of the samples after immersion tests were taken after 10 days as shown in Figure 11 illustrating an increase in carbonate ions from 0 g/l HCO_3^- to 4 g/l HCO_3^- respectively with 0g/l mucin in the solution.

Figure 11(a) shows spherical calcium phosphate composed of splenial microstructures were incompactly deposited on the surface of the sample. The splenial microstructures in rosette cluster of hydroxyapatite have been observed in many studies (Pietak, Mahoney, Dias, & Staiger, 2008; Tomozawa & Hiromoto, 2011) on calcium phosphate coating on titanium or magnesium alloys and on *in vitro* and *in vivo* test for them in physiological environment.

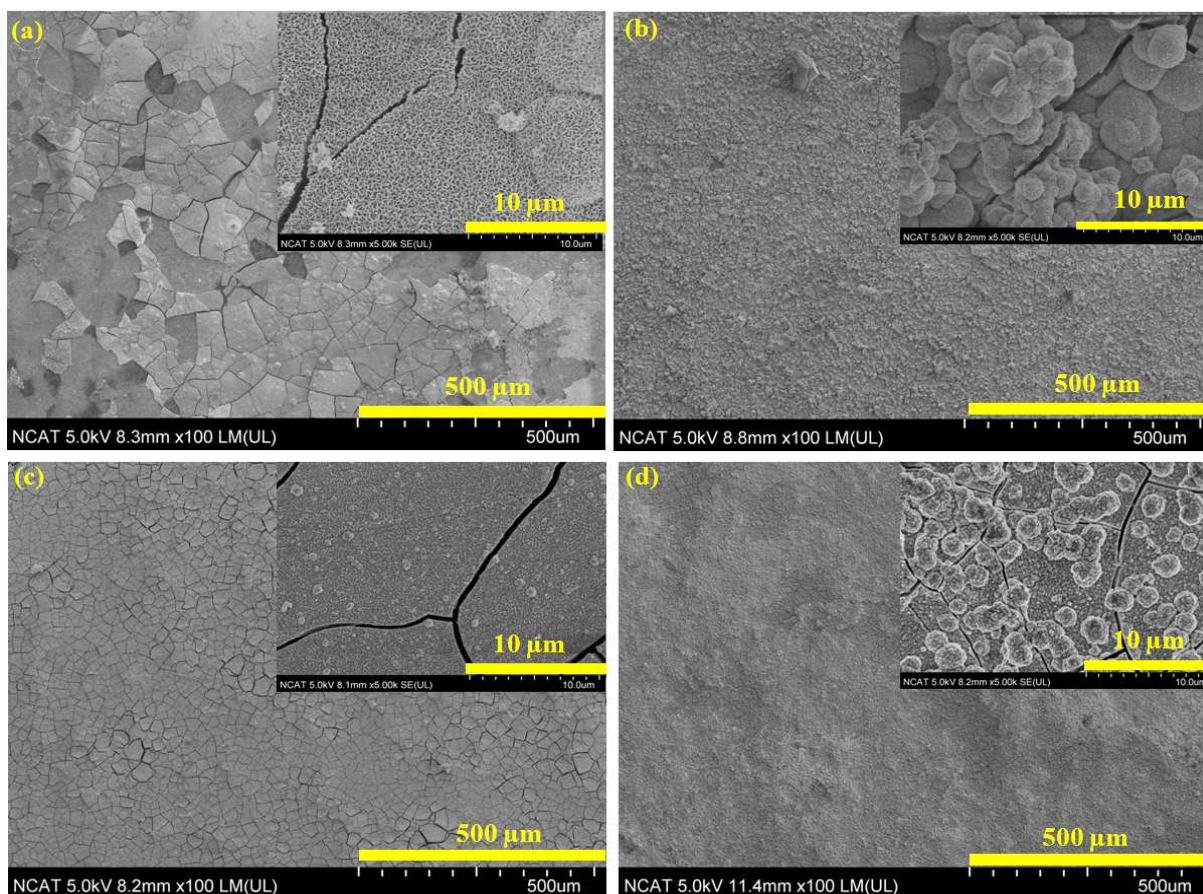


Figure 11. SEM images of corroded surface after immersion test for 10 days. Solutions had 0 g/l concentration of mucin with (a) 0 HCO_3^- ; (b) 1 HCO_3^- ; (c) 2.6 HCO_3^- ; (d) 4 HCO_3^- .

With the addition of HCO_3^- ions, the tendency of corrosion completely changed by being covered with dense corrosion products with spherical calcium phosphate partially formed at sites where pitting corrosions, as shown in Figures 11 (b), (c) and (d). The corrosion thickness was observed to increase with the increase of HCO_3^- ions concentrations while the presence of

hydroxyapatite decreased. The effects of carbonates tend to be complex in terms of corrosion. They can accelerate or slow the corrosion rate of magnesium depending on the concentration of carbonate ions. According to the work of Baril and Pebere, when the concentration of carbonate ions exceeds about 40 mg/L, the corrosion rate goes up due to accelerated dissolution of the $\text{Mg}(\text{OH})_2$ (MgO) protection film (Baril & Pebere, 2001). If the concentration is lower than this critical concentration, corrosion of magnesium can be retarded. The carbonate ions concentration in the gamble solution was about 2.6 g/L (Marques, et al., 2011) which is much higher than 40 mg/L. Hence, carbonates increase the corrosion rate in Gamble solution.

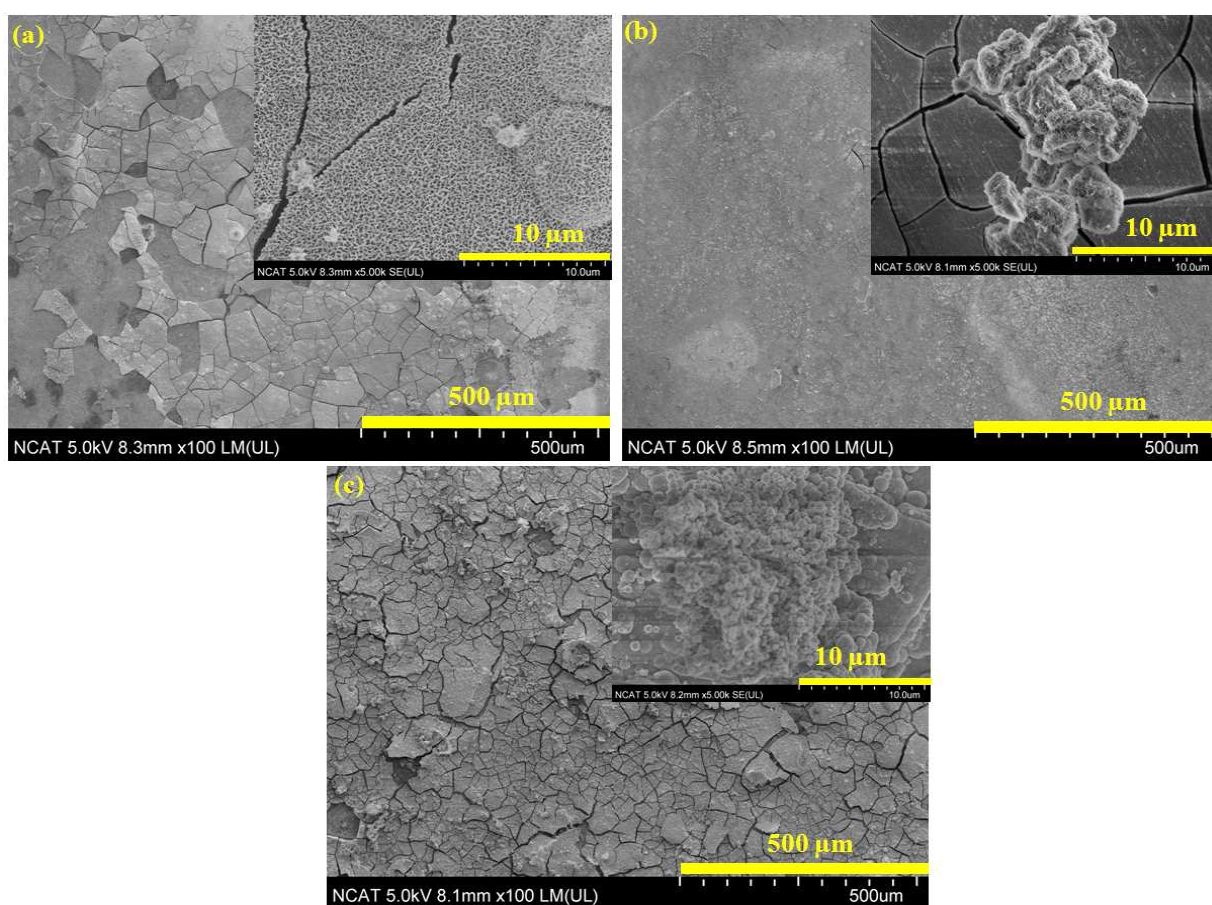


Figure 12. SEM images of corroded surface after immersion test for 10 days. Solutions had 0 g/L HCO_3^- with (a) 0 g/l mucin; (b) 0.03 g/l mucin; (c) 0.1 g/l mucin.

Figure 12 shows SEM images of corroded surface after immersion in test solutions # 1, 5, and 9 containing no concentration of carbonate ions with increasing concentrations of porcine stomach mucin 0 g/l mucin, 0.03 g/l mucin and 0.1g/l mucin respectively. It can be observed that the increase in mucin effect was almost the same as when the carbonate ions in the solutions which decreased the presence of hydroxyapatite on the surfaces of the samples. Porcine stomach mucin adsorption on the solid surface of the magnesium alloy decreased the corrosion rate by reducing the formation of corrosion products forming on the surface or the deposition of calcium phosphate on the surface of the magnesium alloy.

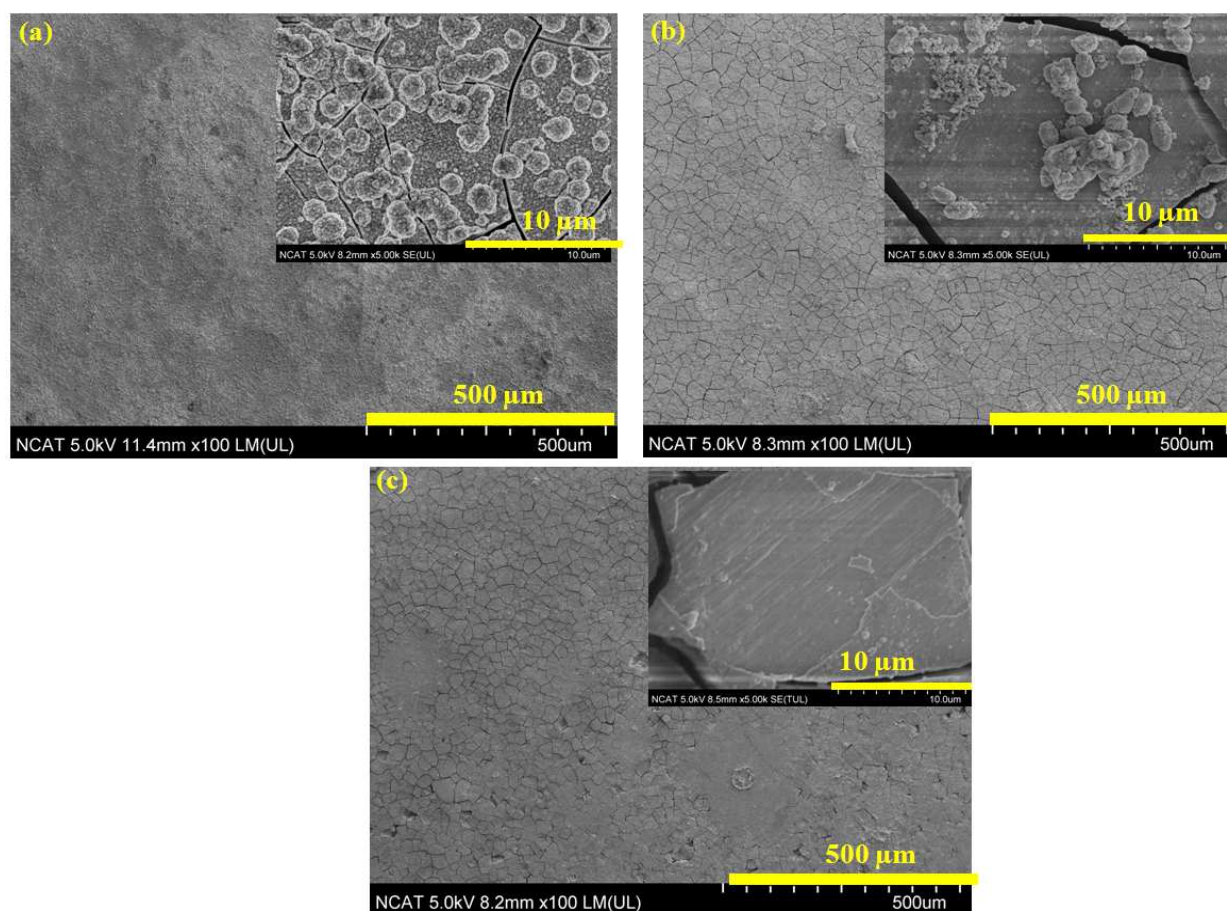


Figure 13. SEM images of corroded surface after immersion test for 10 days. Solutions had 4 g/l HCO_3 with (a) 0g/l mucin; (b) 0.03 g/l mucin; (c) 0.1 g/l mucin.

The mucin is seen to reduce the formation of hydroxyapatite on the surface by attaching on the magnesium surface hence reducing the formation of corrosion products. This same effect observed in the SEM images in Figure 13 of samples immersed in 4 g/l HCO_3^- ions with an increase in mucin. The hydroxyapatite deposition on the surface decreased with an increase in mucin causing the splenial microstructures in rosette cluster of hydroxyapatite to decrease on the surface.

Table 5

Chemical composition of corrosion products formed on the surface after immersion test in solutions for 10 days detected by EDX analysis (Unit: Atomic %)

Solution concentration	C	O	Mg	Al	P	Cl	Ca	Zn
0g/l HCO_3 , 0 g/l Mucin	6.51	42.10	0.95	0.23	18.42	0.00	31.06	0.25
2.6g/l HCO_3 , 0 g/l Mucin	3.89	50.24	21.40	0.00	12.81	0.06	10.03	0.00
0g/l HCO_3 , 0.03 g/l Mucin	6.860	44.62	10.26	0.00	13.33	0.11	24.90	0.65
2.6g/l HCO_3 , 0.03g/l Mucin	5.65	46.20	20.10	3.62	12.65	0.00	11.13	0.12
0g/l HCO_3 , 0.1 g/l Mucin	8.95	38.15	31.40	0.00	12.16	0.09	9.75	0.08
2.6g/l HCO_3 , 0.1 g/l Mucin	10.23	35.21	27.70	1.12	13.21	0.00	12.45	0.00

Table 5 shows chemical composition of general corrosion products formed on the surface after immersion tests for 10 days in Gamble solution (Marques, et al., 2011) as detected by EDX analysis. The EDX table shows corrosion products are mainly $\text{Mg}(\text{OH})_2$ and small amount of MgCO_3 due to the presence of carbonate ions. However, the solution containing 0 g/l HCO_3 , 0 g/l Mucin formed precipitation of O, Ca and P which was uniformly deposited on the surface

with Ca/P ratio of about 1.6~1.8 while magnesium was hardly detected in the corrosion products. Therefore, it might be inferred that the product on the surface on the sample of the solution was only deposited and was not a corrosion product. The fact that the Ca and P exist in the form of hydroxyapatite has been confirmed by the presence of HA peak in XRD.

The constituents of corrosion product formed in solutions containing HCO_3^- ions were O, Mg, P and Ca and Ca/P ratio was about 0.8~1. The amount of magnesium was higher and Ca/P ratio was lower in comparison to composition of corrosion product formed on the sample in the 0 g/l HCO_3^- , 0 g/l mucin solution. The was small contents of Al in corrosion products formed on the surfaces of the samples immersed in solutions containing HCO_3^- than samples immersed in solutions without HCO_3^- ion as identified from the EDX data of Table 6. Elemental mapping images on predominant constituents of cross sections of corrosion products formed after the immersion test for 10 days is shown in Figure 14.

The mapping results in Figure 14(a) showed the deposition of calcium phosphate compound on the surface of the sample immersed in Gamble solution containing 0 g/l HCO_3^- , 0 g/l mucin. The deposition of calcium phosphate was observed to be thicker with no pitting corrosion on the surface of the magnesium substrate. Small amounts of Al was also observed on the surface of the corrosion products, however, the predominant elements were Ca, P, and O. Figure 14(b) shows mapping elements of corrosion products formed on the samples immersed in solutions containing 0 g/l HCO_3^- , 0.1 g/l mucin which was observed to have thin corrosion products of Ca, P and O elements. The thickness of the corrosion product decreased in thickness in the presence of mucin. The Mg substrate had no pitting on the surface due to the deposition of both mucin and calcium phosphate on the surface.

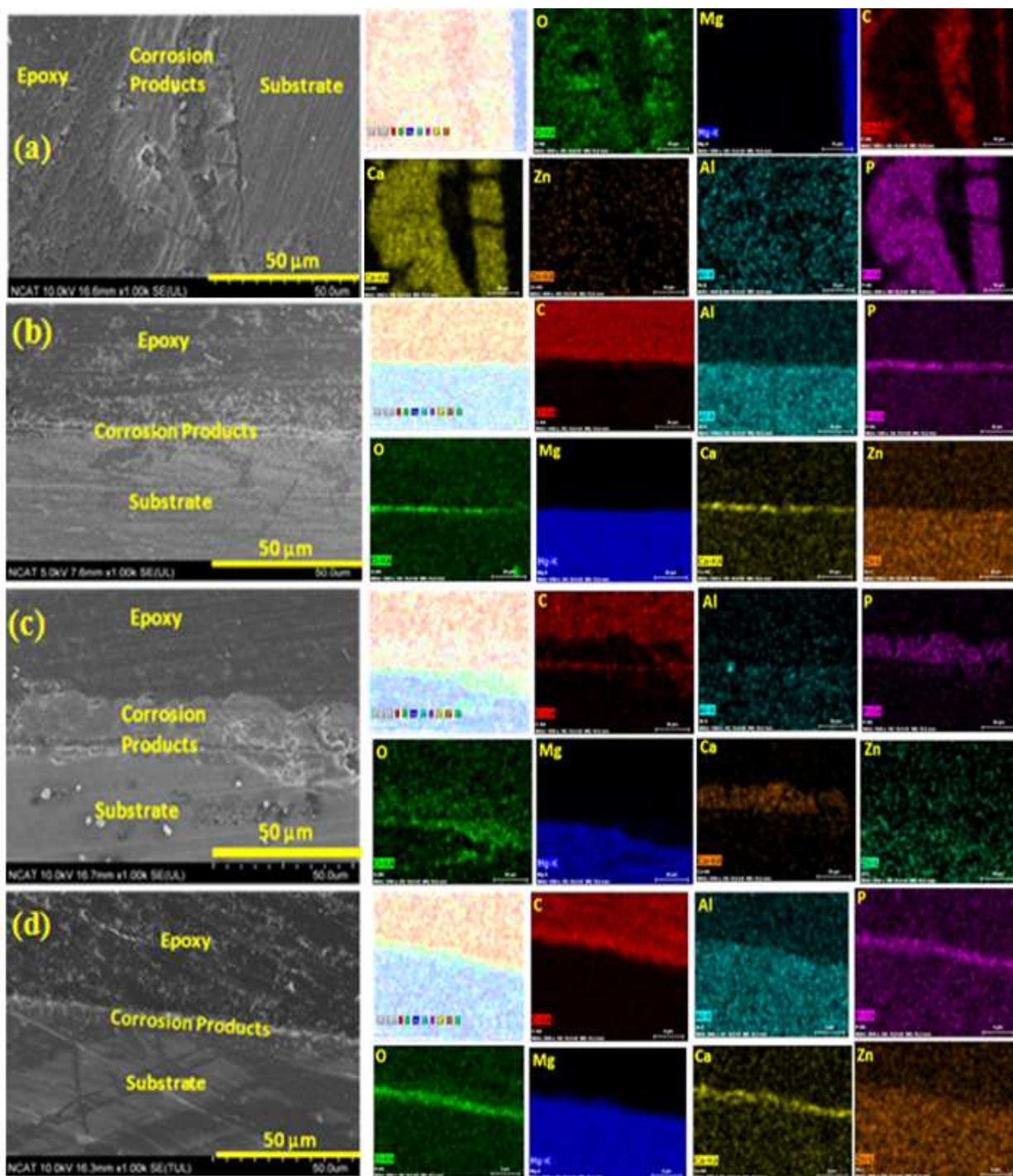


Figure 14. SEM images showing mapping images of cross-sections of corrosion products formed after immersion for 10 days in Gamble solution; (a) 0 g/l HCO_3 , 0 g/l mucin, (b) 0 g/l HCO_3 , 0.1 g/l mucin, (c) 2.6 g/l HCO_3 , 0 g/l mucin and (d) 2.6 g/l HCO_3 , 0.1 g/l mucin.

Figure 14(c) shows mapping illustrating corrosion products elements formed on the samples immersed in the Gamble solutions containing 2.6 g/l HCO_3^- , 0 g/l mucin. It was observed that the thick corrosion products displayed pitting corrosion on the surface of the sample tested compared to the sample immersed in 2.6 g/l HCO_3^- , 0.1 g/l mucin which had a thinner corrosion products with uniform and pitting corrosion forming on the surface. The main corrosion product on the samples containing HCO_3^- ions were mainly $\text{Mg}(\text{OH})_2$ which was reconfirmed from the line analysis results in Figure 15 while the samples immersed 0 g/l HCO_3^- , 0 g/l mucin had mostly calcium phosphate deposition on the surface.

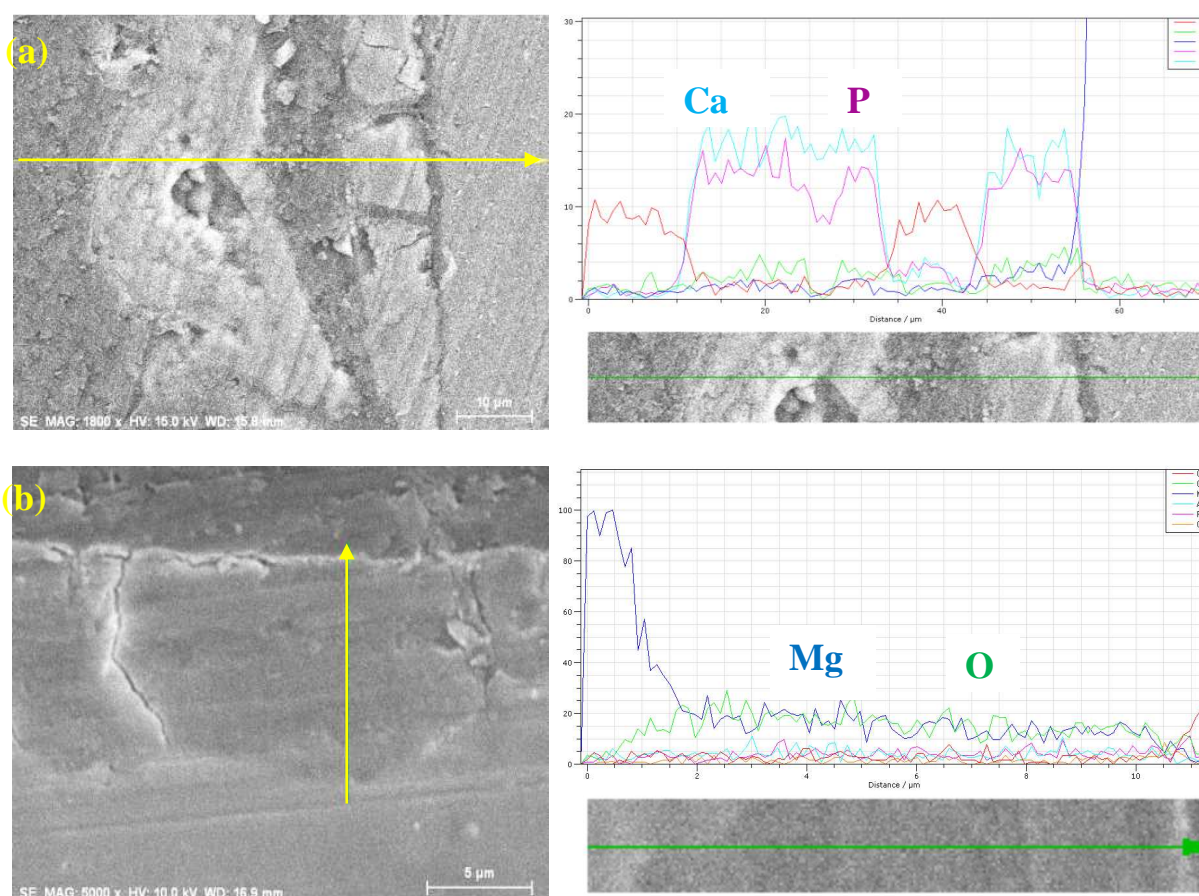


Figure 15. Line analysis of cross section on corrosion products after immersion test in the solutions (a) 0 g/l HCO_3^- , 0 g/l Mucin, (b) 2.6 g/l HCO_3^- , 0 g/l Mucin.

Figure 16 shows SEM cross-section morphology comparison to determine effect of both carbonate and mucin showing the corrosion product thickness formed on the surface samples. The thickness of corrosion products on the surface of the samples increases when immersed in the test solution containing HCO_3^- ions. Thus the more concentrated the test solution was with carbonate ions, the thicker the corrosion products. However, the thickness of the corrosion products decreased with the increase of mucin concentration in the solution. The average thickness of calcium phosphate deposition formed on the surface of the sample immersed in 0 g/l HCO_3^- , 0 g/l mucin solution was approximately 36.2 μm while the average deposition thickness formed on the surface immersed in 0 HCO_3^- , 0.1 g/l mucin was approximately 3.1 μm thick. The thickness of the corrosion products was measured using Image Pro software which measured 10 different lengths on each SEM image and an average of the values calculated to get an approximate average thickness. Since one sample was used to measure the thickness of the corrosion products, no statistical analysis was performed.

The sample immersed in 2.6 g/l HCO_3^- , 0 g/l mucin had uniform corrosion products of an average thickness of approximately 19.5 μm while 2.6 g/l HCO_3^- , 0.1 g/l mucin decreased to about 5.6 μm thick. The average thickness of corrosion products formed on the sample immersed in 4 g/l HCO_3^- , 0 g/l mucin was approximately 32 μm while the sample immersed in 4 g/l HCO_3^- , 0 g/l mucin solution had approximately 8.7 μm thick corrosion products. It can therefore be concluded that mucin had an effect on reducing the corrosion rate of the samples by lowering the corrosion products formed on the samples while the increase of carbonate ions increased passivation on the surface resulting to thicker corrosion products.

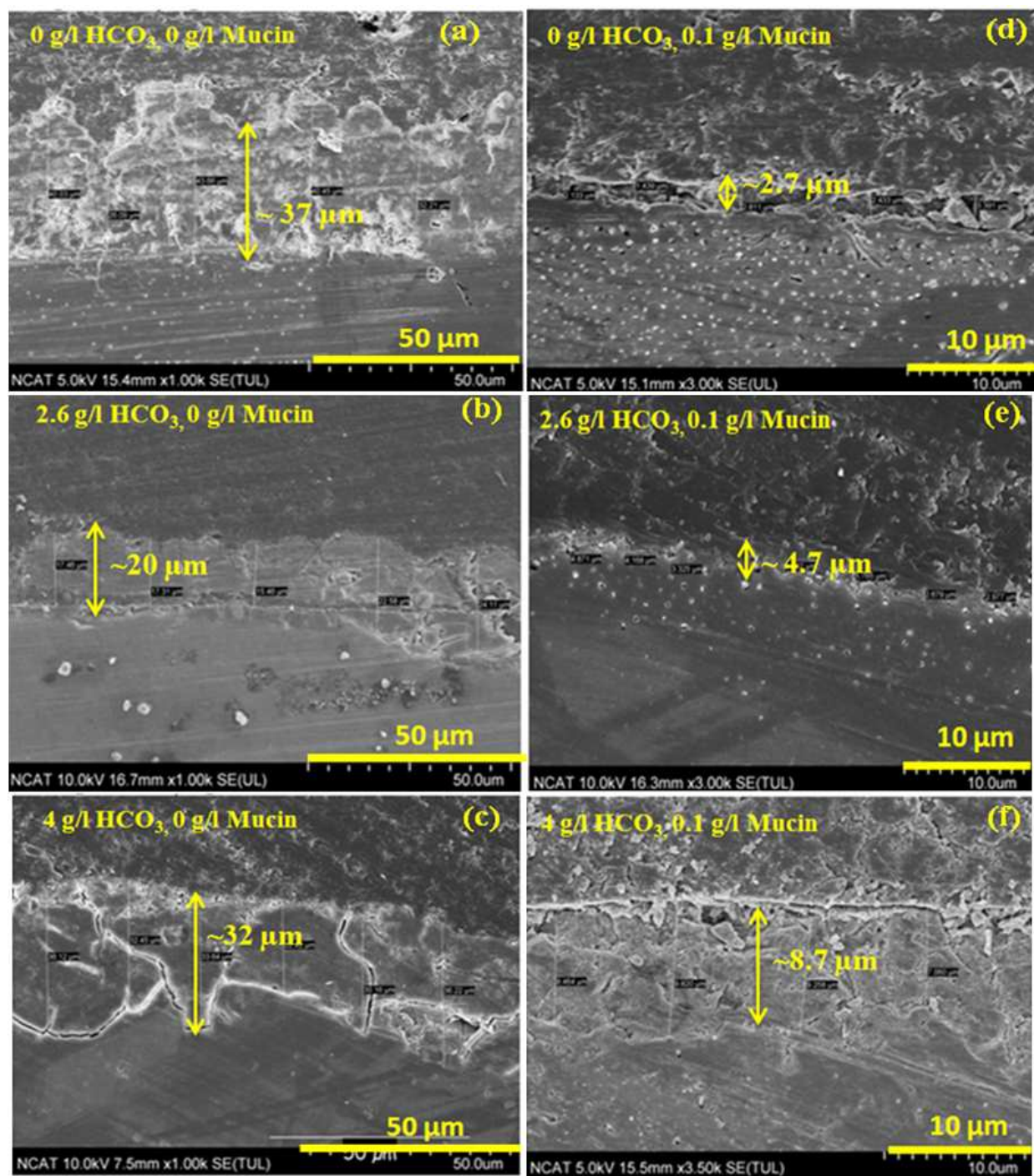


Figure 16. SEM cross-section morphology comparing the corrosion products thickness on the samples in different solution concentrations; (a) 0 g/l HCO_3^- , 0 g/l Mucin, (b) 2.6 g/l HCO_3^- , 0 g/l Mucin, (c) 4 g/l HCO_3^- , 0 g/l Mucin (d) 0 g/l HCO_3^- , 0.1 g/l Mucin, (e) 2.6 g/l HCO_3^- , 0.1 g/l Mucin and (f) 4 g/l HCO_3^- , 0.1 g/l Mucin.

4.1.4 X-ray diffraction (XRD) results. The XRD analysis of corrosion products revealed the presence of calcium phosphate (hydroxyapatite) precipitate peaks on the surface of the sample immersed in Gamble solution containing 0 g/l HCO_3^- , 0 g/l mucin. The hydroxyapatite exhibited high intensity peaks and was noted to decrease with both the increase of both mucin and bicarbonate ions in the solutions as illustrated in Figures 36 and 37 at the appendix. This implies that mucin altered the formation of corrosion by inhibiting calcium phosphate compounds from forming on the magnesium surface while the addition of carbonate ions accelerated general corrosion rate with presence of magnesium carbonate peaks on the surface of the surface samples. The results also revealed presence of magnesium hydroxide ($\text{Mg}(\text{OH})_2$) as the main corrosion products although the peaks weren't as high due to formation of thin corrosion layer formed on the surface of the immersed samples.

4.2 Electrochemical Test Results

4.2.1 pH measurement. Figure 17 shows variation of pH plot illustrating the effect of mucin when increased in Gamble solution containing 4 g/l HCO_3^- during electrochemical testing for a period of 24 hours. The pH was noted to increase gradually in all the three different solutions. The presence of bicarbonate HCO_3^- ions in the solution caused a substantial increase in the pH. However, with the increase of mucin in the Gamble solution, the pH decreased hence slowing the corrosion rate. Mucin adsorption on the surface of the magnesium samples surface reduced the formation of corrosion products forming on the surface, hence the low pH with the increase in mucin. Similarity could also be observed between the immersion test pH measurement and the electrochemical test. Both tests had a pH increase of around the same value, for example comparing 4 g/l HCO_3^- , 0 g/l mucin test solution had an increase of approximately +1.2 for the duration of the 24 hours.

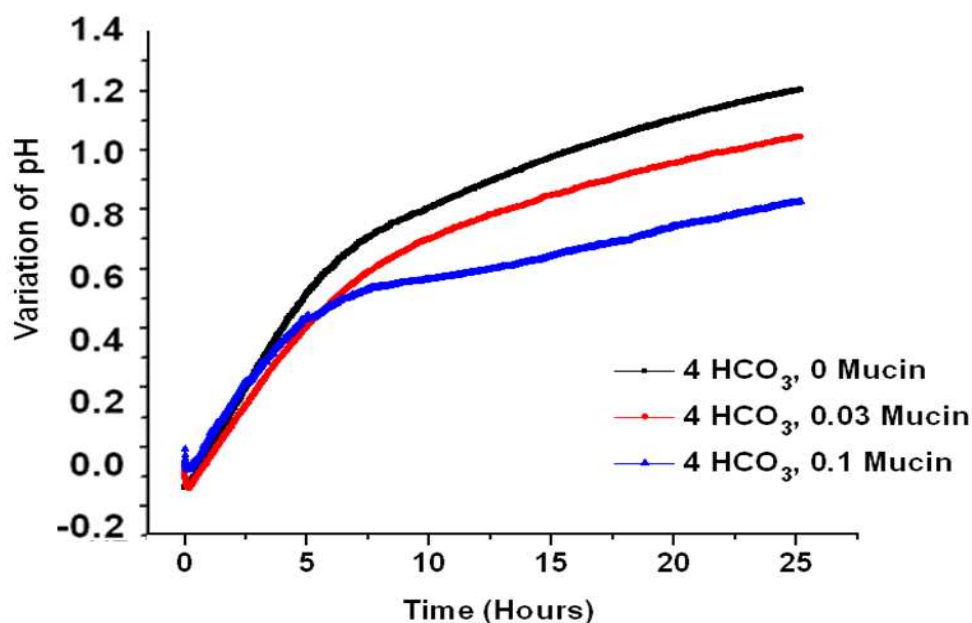


Figure 17. Variation of pH plot showing the effect of mucin increase on the pH of Gamble solution containing 4 g/l HCO₃ during electrochemical testing.

4.2.2 Open circuit potential (OCP). Figure 18 shows the evolution of Open Circuit Potential (OCP) for AZ31B magnesium alloys when immersed in Gamble solution at 37°C for 24 hour comparing the effect of mucin in terms of concentration (0 g/l, 0.03 g/l, and 0.1 g/l). Both samples immersed in gamble solution containing 0 g/l HCO₃ and 1 g/l HCO₃ in Figure 18(a) had almost identical increase in potential which increased rapidly before stabilizing after 2.5 hours of immersion. However, the samples immersed in Gamble solution containing both 2.6 g/l HCO₃ and 4 g/l HCO₃ had a prolonged increase in potential which took 5 hours before starting to fluctuate between -1.35 V and -1.45 V throughout the immersion period. Figure 18(b) had the same tendency as (a), however, the only difference is that the potential of the sample immersed in 4 g/l HCO₃ increased gradually for about 10 hours before stabilizing with a potential of 1.34V. Figure 18(c) shows a rapid increase in potential of sample immersed in Gamble

solution containing 0 g/l HCO_3^- for 1 hour before it stabilized at 1.45V. After 10 hours, the potential was observed to decrease to 1.50V. The samples immersed in 2.6 g/l HCO_3^- and 4 g/l HCO_3^- had the same increase in potential. The sharp rise observed during the open circuit potential first hours of immersion is probably due to film formation or passivation.

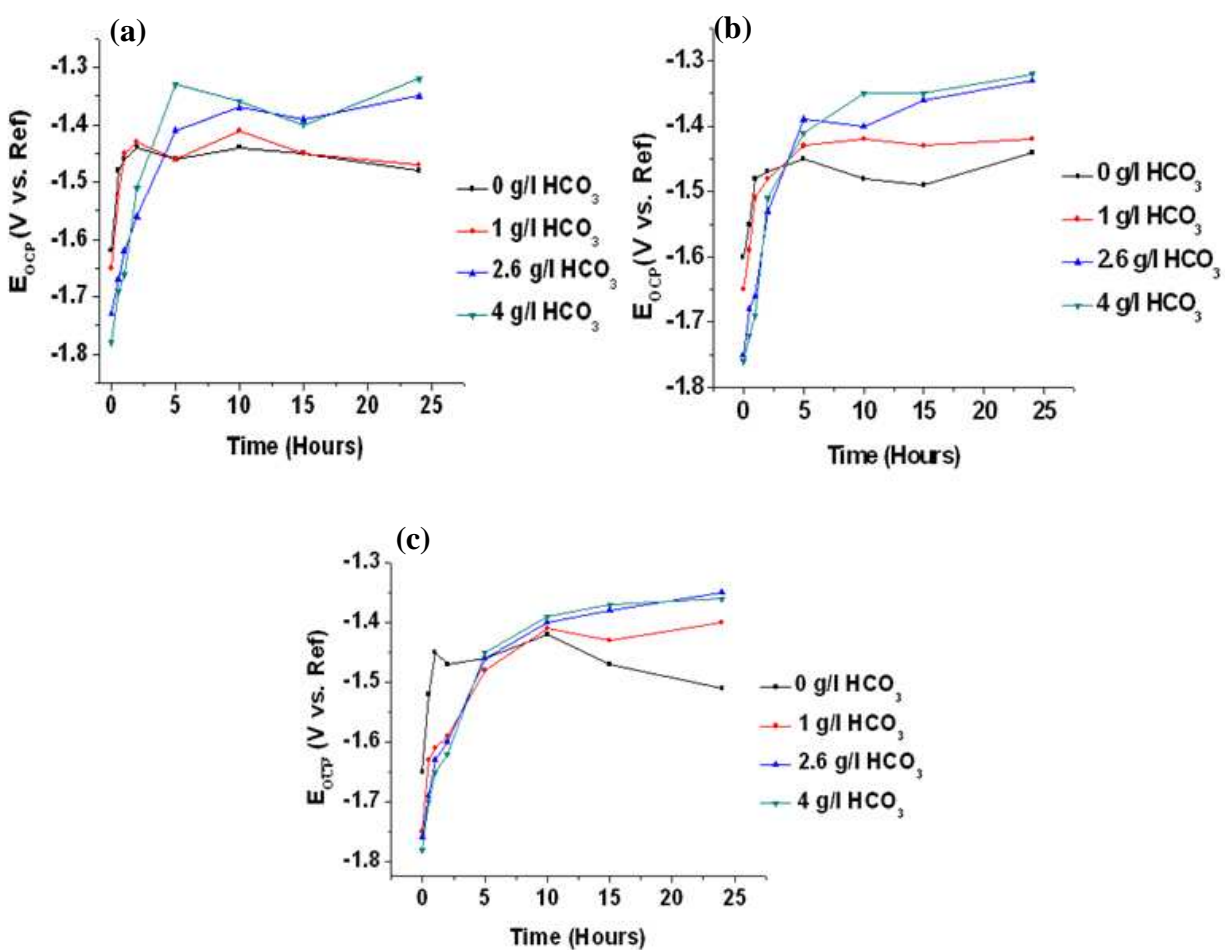


Figure 18. OCP plots comparing the mucin effect on the samples immersed in Gamble solution containing different concentration of HCO_3^- ions for 24 hours at 37°C . (a) 0 g/ml mucin; (b) 0.03 g/l mucin; (c) 0.1 g/l mucin.

The effect of the different concentrations of mucin in the solution did not have an effect on the potential on the samples being tested. However, the potential increased with an increase of HCO_3^- ions in the solutions which was due to the increase of the corrosion products forming on

the surface of the magnesium samples possibly magnesium hydroxide, magnesium carbonate or calcium phosphate. Therefore, increasing HCO_3^- ions in the solutions caused the thicker corrosion product which resulted in the higher potential.

The open circuit potential (OCP) is a parameter easily determined experimentally through direct measurement of the electrode potential in relation to a reference electrode. OCP indicates the thermodynamically tendency of a material to electrochemical oxidation in a corrosive medium. The OCP was recorded until it stabilizes around a stationary value within three to four hours of immersion, although this potential may vary with time because changes in the nature of the surface of the electrode such as the oxidation and formation of the passive layer.

4.2.3 Electrochemical impedance spectroscopy (EIS) results. As enlightened previously, in order to identify and investigate the electrochemical reaction mechanisms, the electrochemical behavior of the untreated, anodized and PLGA coated samples were examined by EIS. The EIS measurements with its frequency depending information allow distinguishing between different corrosion mechanisms and to assess the protecting ability of the surface corrosion products. The film formed during exposure to the different electrolytes can act, according to its stability and homogeneity, as a more or less efficient electric barrier for the charge transfer. The higher the resistance of the resultant surface layer, the higher the corrosion resistance of the film and therefore the higher will be the impedance value measured at low frequency (Quach, Uggowitzer, & Schmutz, 2008).

Based on the impedance plots, the microstructural features of the corrosion products and oxide coating, appropriate equivalent circuit have been proposed as shown in Figure 19 (Duan, Yan, & Wang, 2007; Ghasemi, et al., 2008). The equivalent circuit consists of two R/CPE components in series with R_s , corresponding to the three parts of the EIS measured, i.e. corrosive

environment, outer layer and inner layer, respectively. In the equivalent circuit, R_s is the solution resistance; R_1/CPE_1 pair represents the resistance of the corrosion products or coating, and R_2/CPE_2 pair is the inner layer/interface resistance of the corrosion products or coating.

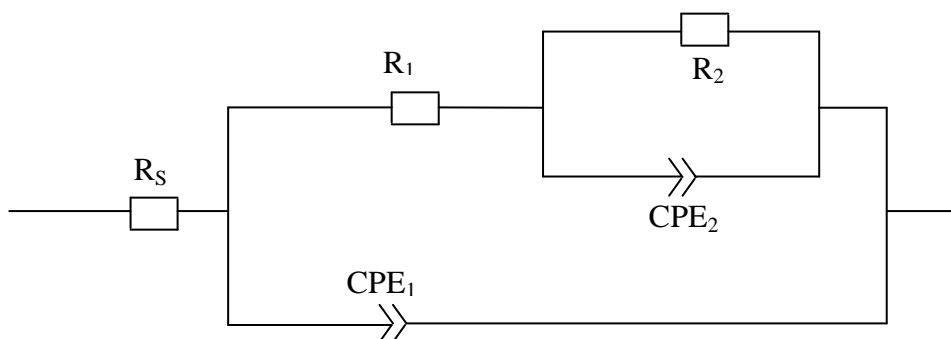


Figure 19. Schematic representation corresponding to equivalent circuit of EIS plot.

Figure 20 shows the EIS nyquist plots for AZ31 magnesium samples immersed in Gamble solution without carbonate ions showing the effect of mucin increase at 37°C at different immersion times up to 24 hours. The choice of such a long duration is essential to estimate the longevity of the material being tested for implant application and at the same time help study the corrosion products formed on the surfaces of the samples. The Nyquist plots sample had similar shapes of the except for the difference in the diameter of loops. The diameter of the capacitive semicircle of a measured Nyquist spectrum is closely related to the corrosion rate (G. L. Song, Bowles, & StJohn, 2004), the larger the semicircle is, the better the corrosion resistance is. The larger diameters represent higher frequency while the smaller diameters represent low frequency. The high frequency capacitive loop may originate from the passivation on the AZ31 alloy hence better corrosion resistance. Figure 20 (a) diameter loop increased for 10 hours, before the corrosion resistance of the sample started to decline.

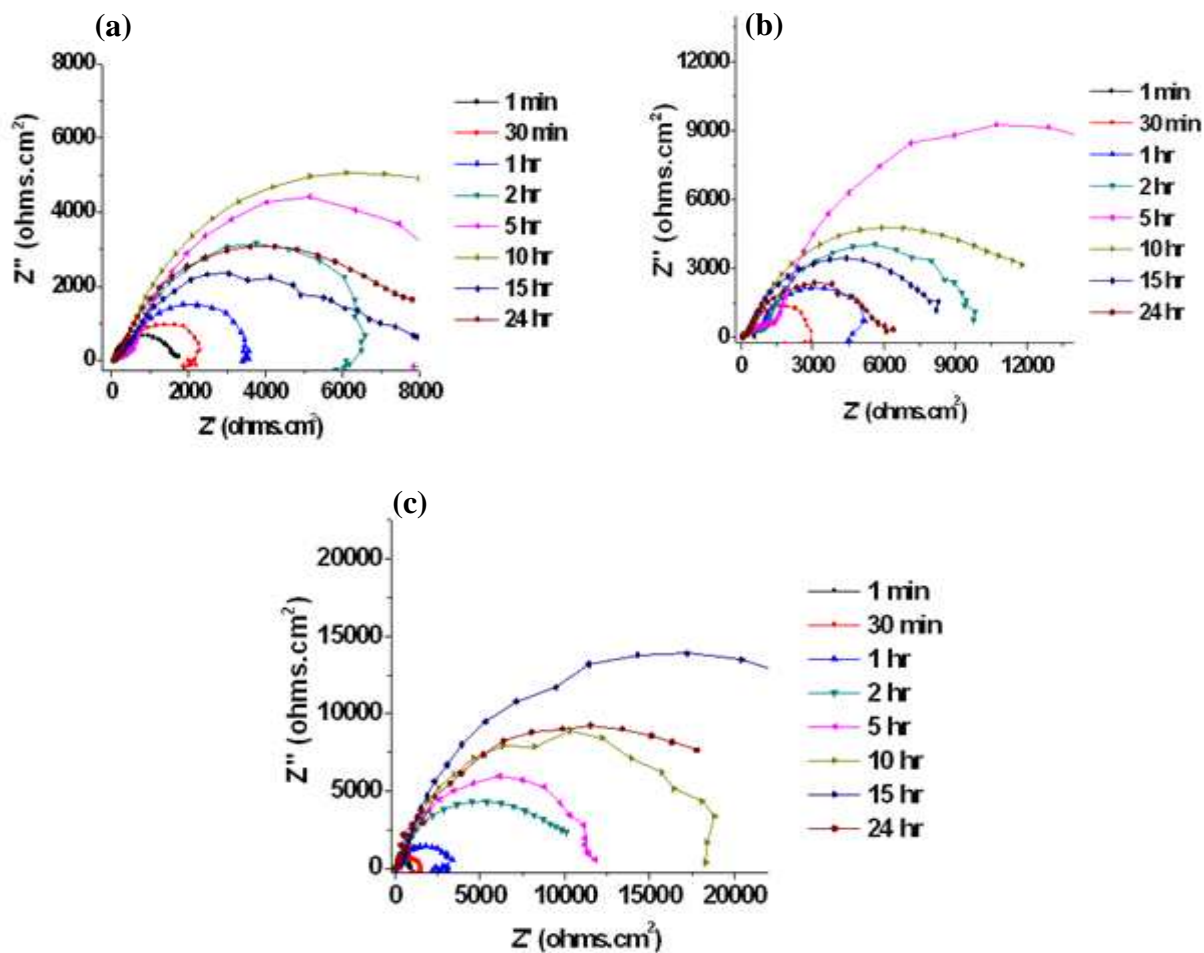


Figure 20. EIS nyquist plots of sample immersed in Gamble solution containing 0g/l HCO_3^- showing the effect of mucin increase. (a) 0g/l Mucin (b) 0.03g/l mucin; (c) 0.1g/l mucin.

Figure 20 (b) increased for 5 hours before the decline of the corrosion resistance while Figure 20 (c) increased for 15 hours before it started to decline. The decline in the diameter loop is due to the pitting corrosion formed on the surface of the samples which breaks the passivation on the surface. It can therefore be concluded that a larger amount of mucin in the Gamble solution stabilizes the sample hence having a better corrosion resistance. The circuit elements calculated from the fitting results of the immersion impedance plots showing increase in mucin concentrations is summarized in Table 6.

Table 6

Parameters of EIS showing the effect of mucin increase in Gamble solution

Time (Hours)	0 g/l HCO ₃ , 0 g/l Mucin R ₁ (Ωcm ²)	0 g/l HCO ₃ , 0.03 g/l Mucin R ₁ (Ωcm ²)	0 g/l HCO ₃ , 0 g/l Mucin R ₁ (Ωcm ²)
1 hr	3.225×10 ³	4.081×10 ³	2.571×10 ³
2 hr	6.161×10 ³	8.930×10 ³	6.034×10 ³
5 hr	8.550×10 ³	20.68×10 ³	11.87×10 ³
10 hr	13.82×10 ³	13.78×10 ³	12.34×10 ³
15 hr	7.232×10 ³	9.045×10 ³	37.48×10 ³
24 hr	8.410×10 ³	6.969×10 ³	23.49×10 ³

Table 6 shows the resistance of corrosion products formed on the immersed surface during EIS. The sample immersed in 0 g/l HCO₃, 0 g/l mucin solution had its corrosion products resistance increased over duration of 10 hours to 13.82x10³ Ωcm² before it started decreasing and fluctuating around 8.41x10³ Ωcm² after 24 hours of immersion. The decrease in the resistance of the corrosion products after 10 hours of immersion was due to pitting corrosion formed on the passivation layer which caused the resistance to decrease. The sample immersed in 0 g/l HCO₃, 0.03 g/l mucin solution had its corrosion products resistance increase for 5 hours before it started decreasing ending up with 6.96x10³ Ωcm² after 24 hours. However when 0.01 g/l of mucin was added in the solution the passivation layer was more stable and increased gradually before starting to decrease after 15 hours. Therefore, it could be concluded that a larger amount of mucin in the solution caused the corrosion products formed on the surface to be more stable and decreasing pitting corrosion from happening on the surface of the passivation layer.

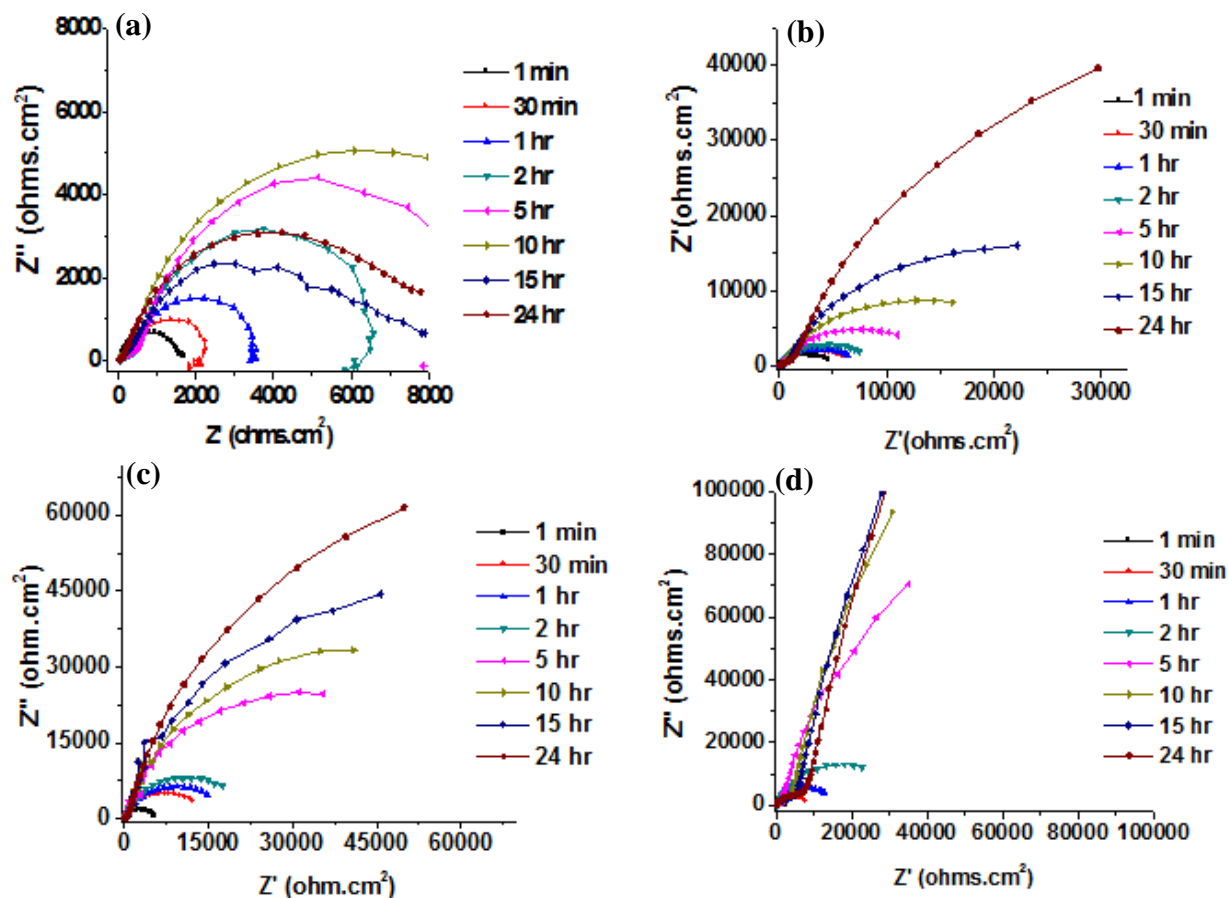


Figure 21. EIS nyquist plots of sample immersed in Gamble solution containing 0g/l mucin showing the effect of increasing carbonate ions (a) 0 g/l HCO_3^- ; (b) 1 g/l HCO_3^- ; (c) 2.6 g/l HCO_3^- ; (d) 4 g/l HCO_3^- .

Figure 21 shows EIS nyquist plots for AZ31 magnesium samples immersed in Gamble solution without mucin showing the effect of increasing carbonate ions at 37°C at different immersion times up to 24 hours. The diameters of loops are increased with the increase in carbonate ions in the solution causing surface passivation. This behavior mainly resulted from the fast precipitation of magnesium hydroxide and magnesium carbonate in the corrosion product layer that can subsequently suppress development of pitting corrosion completely.

The circuit elements calculated from the fitting resulted from the immersion impedance plots showing increase in carbonate ions concentrations are summarized in Table 7. After 24

hours of immersion, the sample immersed in 0 g/l HCO_3 , 0 g/l mucin corrosion product resistance of $8.41 \times 10^3 \Omega\text{cm}^2$ while the samples immersed in 1 g/l HCO_3 , 0 g/l mucin, 2.6 HCO_3 , 0 g/l mucin and 4 g/l HCO_3 , 0 g/l mucin had R_1 values of $191.9 \times 10^3 \Omega\text{cm}^2$, $224.7 \times 10^3 \Omega\text{cm}^2$ and $8.446 \times 10^6 \Omega\text{cm}^2$ respectively. From the EIS parameters, it can be proven that the corrosion products resistance R_1 or the passivation layer increases with the increase of the carbonate ions in the solution.

Table 7

Parameters of EIS showing the effect of carbonate ions in Gamble solution

Time (Hours)	0 g/l HCO_3 , 0g/l Mucin R_1 (Ωcm^2)	1 g/l HCO_3 , 0g/l Mucin R_1 (Ωcm^2)	2.6 g/l HCO_3 , 0 g/l Mucin R_1 (Ωcm^2)	4 g/l HCO_3 , 0g/l Mucin R_1 (Ωcm^2)
1 hr	3.225×10^3	7.137×10^3	17.82×10^3	15.77×10^3
2 hr	6.161×10^3	8.666×10^3	22.27×10^3	36.02×10^3
5 hr	8.550×10^3	14.58×10^3	76.56×10^3	503.9×10^3
10 hr	13.82×10^3	26.18×10^3	97.71×10^3	2.340×10^6
15 hr	7.232×10^3	48.54×10^3	137.9×10^3	3.923×10^6
24 hr	8.410×10^3	191.9×10^3	224.7×10^3	8.446×10^6

The corrosion resistance of the untreated sample in Gamble solution with different concentration of mucin was also evaluated by EIS. The different concentrations of mucin tested were 0, 0.1, 0.5 and 1 g/l mucin. Gamble solution with 1 g/l mucin solution had a higher polarization resistance due to the larger diameter of the capacitive loop, hence suggesting a stronger anti-corrosion property. Mucin adsorption on the surface of the magnesium samples surface increased its corrosion resistance while the low value of the polarization resistance with

0g/l mucin indicated that the untreated AZ31 Mg alloy sample would be eroded easily. The Nyquist plot is shown in Figure 22.

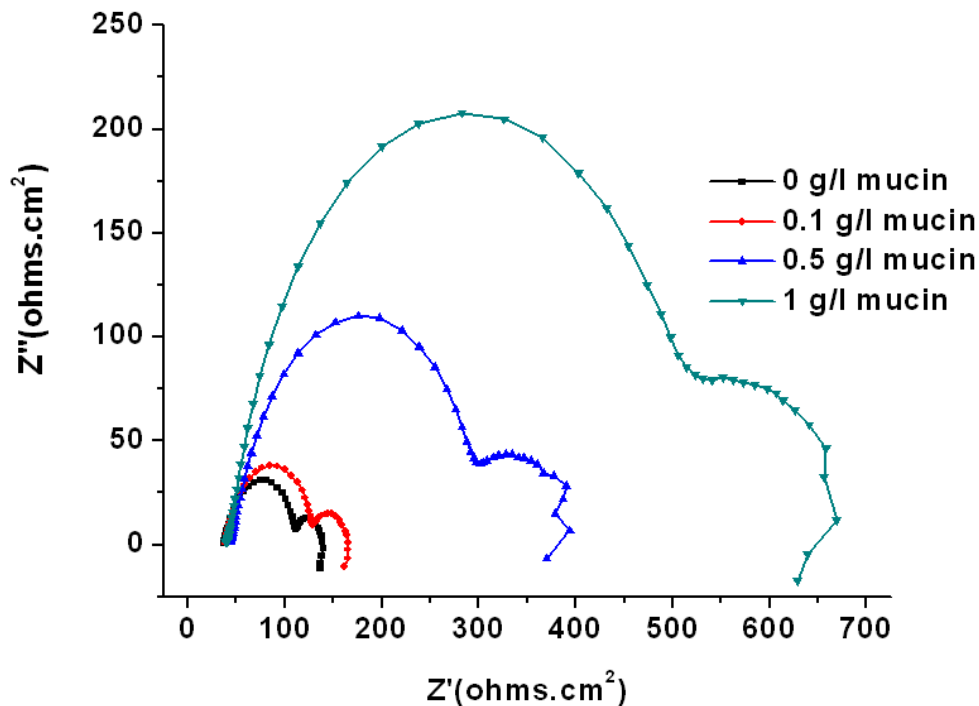


Figure 22. Nyquist plots of untreated magnesium AZ31 samples immersed in Gamble solution in different concentrations of mucin.

The values of the fitting circuit elements are summarized in Table 8 respectively. The results showed AZ31 Mg alloy sample immersed in solution containing 0 g/l mucin had a polarization resistance of $76.73 \Omega\text{cm}^2$. The low value of the polarization resistance indicated that the sample would be eroded easily. The polarization resistance value increased with increase in mucin hence solution with 1 g/l mucin had a value of $507.5 \Omega\text{cm}^2$ hence changing the anti-corrosion properties of the film thereby preventing the corrosive medium from penetrating into the Mg alloy substrate. The EIS results are in good agreement with the Potentiodynamic polarization test.

Table 8

Parameters of untreated AZ31 by fitting EIS model carried out in Gamble with different concentrations of mucin

Untreated AZ31 Sample	$R_S (\Omega\text{cm}^2)$	$R_1 (\Omega\text{cm}^2)$	$\text{CPE}_1 (\text{S}^*\text{s}^a)$	$R_2 (\Omega\text{cm}^2)$	$\text{CPE}_2 (\text{S}^*\text{s}^a)$
0 g/l Mucin	37.65	76.73	35.35×10^{-6}	23.50	4.99×10^{-3}
0.1g/l Mucin	39.08	94.16	31.88×10^{-6}	29.04	4.74×10^{-3}
0.5g/l Mucin	43.97	270.6	20.97×10^{-6}	72.38	2.67×10^{-3}
1g/l Mucin	40.49	507.5	15.47×10^{-6}	109.2	1.68×10^{-3}

EIS proved to be a useful technique, because it offers insight into both the mechanism of corrosion attack while at the same time analyzing the processes taking place on a specimen's surface (Xin, et al., 2007). A small amplitude AC signal is applied to the system being studied during the EIS experiment making it a non-destructive method for the evaluation of a wide range of materials, including coatings and anodized films. It can also provide detailed information of the systems under examination; parameters such as corrosion rates, dielectric properties, compositional influences on the conductance of solids, electrochemical mechanisms, mass transport, detection of localized corrosion, and reaction kinetics can all be determined from these data (Hamdy, El-Shenawy, & El-Bitar, 2006; Macdonald, 2005).

4.2.4 Linear polarization resistance (LPR). Linear polarization tests were conducted on a 24 hour period using sequence wizard software to assess the rate of localized corrosion of the surface of the AZ31 alloys. Figure 23 shows linear polarization curves of AZ31 sample immersed in Gamble solution for a period ranging from 1 hour to 24 hours. After 1 hour period

of immersion, the sample's OCP was about -1.62V, while after 24 hours, the OCP was -1.32V.

The linear polarization instrumentation using Gamry Echem Analyst software was used to convert the current measured to corrosion rate readings in mils per year (mpy).

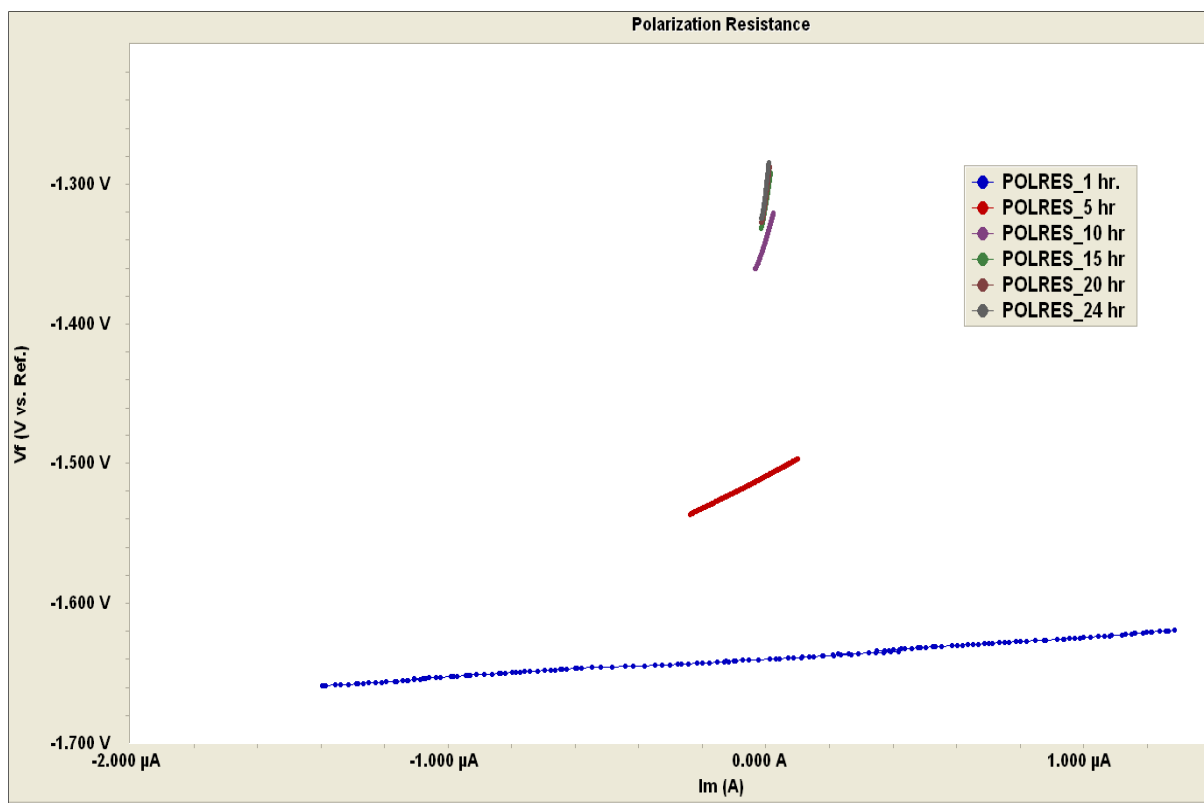


Figure 23. Linear polarization curves of sample immersed in Gamble solution containing 2.6 g/l HCO_3^- , 0g/l mucin for 24 hours.

The OCP of the samples increase as the immersion time increasing, thus the high potential and low corrosion current results low corrosion rate of 7.86×10^{-3} mpy on the sample as illustrated in Table 9. After 1 hour of immersion, the polarization curve had a low OCP with high corrosion current which is directly proportional to the corrosion rate, hence high corrosion rate of 1.079 mpy. The increase in OCP with time causing the corrosion rate to decrease was probably due to film formation or passivation on the surface of the immersed sample.

Table 9

Linear polarization data measurement by Gamry Echem Analyst software of untreated AZ31 alloy immersed in Gamble solution containing 2.6 g/l HCO_3^- , 0g/l mucin for 24 hours.

Immersion Time	Corrosion Rate (mpy)
1 hour	1.079
5 hour	126.4×10^{-3}
10 hours	20.82×10^{-3}
15 hours	10.93×10^{-3}
20 hours	8.63×10^{-3}
24 hours	7.86×10^{-3}

Linear Polarization Resistance measured the DC current through the metal interface when the electrodes are polarized by a small electrical potential. LPR test is a non-destructive electrochemical technique in which the potential of a metal is scanned over a small range relative to the open circuit potential and the resulting current is measured. This current is related to the corrosion current which in turn is directly proportional to the corrosion rate. The major advantage to LPR monitoring is the speed in which it can provide an instantaneous measurement of the corrosion rate (Argade, Panigrahi, & Mishra, 2012). Changes in the corrosion rate can typically be detected in minutes, providing an almost instantaneous measuring system. This fast response allows an operator to evaluate process changes and is particularly useful in monitoring the effectiveness of a prevention program. It can also provide a qualitative pitting tendency measurement, such as whether the tendency for pitting will be shallow and infrequent, or deep and abundant.

4.2.5 Potentiodynamic polarization. Representative potentiodynamic polarization curves for untreated AZ31B samples immersed in Gamble solution with different concentrations of mucin are displayed in Figure 24. The corrosion potential e_{corr} and corrosion current density i_{corr} were calculated from the intersection of the cathodic and anodic Tafel curves extrapolated cathodic and anodic polarization curves. When e_{corr} increases and i_{corr} decreased, the corrosion resistance of the samples would be improved. It is obviously that the corrosion potentials increased with the increase of mucin from 0 g/l to 1 g/l in the solution having corrosion potentials of -1.78 V, -1.76 V, 1.72 V and -1.64 V respectively.

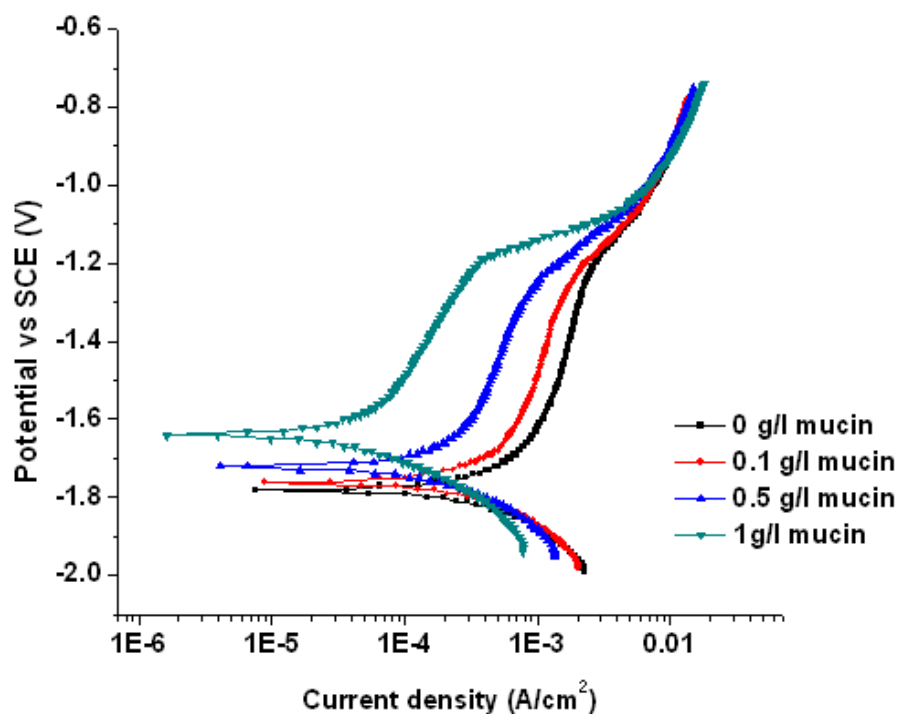


Figure 24. Potentiodynamic polarization curves of untreated magnesium AZ31 samples immersed in Gamble solution with different concentrations of mucin.

Fitting results of electrochemical parameters, as seen in Table 10, prove that polarization resistance increases and corrosion current density (i_{corr}) reduces remarkably with the increase in the mucin concentration. The untreated AZ31 sample immersed in Gamble solution containing 0

g/l mucin had a corrosion current density of 8.35×10^{-1} mA/cm² while the sample immersed in gamble solution containing 1g/l mucin had a corrosion current density of 3.07×10^{-2} mA/cm². It implied that mucin played a good protection by effectively decreasing the corrosion rate of magnesium by acting as a barrier shield.

Table 10

Parameters of untreated magnesium AZ31 samples immersed in Gamble solution with different concentrations of mucin

Untreated AZ31 Sample	E_{corr} (V)	I_{corr} (mA/cm ²)	Corrosion rate (mpy)
0 g/l Mucin	-1.78	8.35×10^{-1}	752.14
0.1 g/l Mucin	-1.76	4.90×10^{-1}	441.38
0.5 g/l Mucin	-1.72	1.71×10^{-1}	154.03
1 g/l Mucin	-1.64	3.07×10^{-2}	27.65

4.3 Plasma Electrolytic Oxidation and PLGA Coating Results

Figure 25 shows the result of potentiodynamic polarization for corrosion assessment. After the potentiodynamic polarization tests, corrosion craters could be observed evidently by naked eyes on the surface of magnesium alloy substrate, but there were no distinct changes on the surface of coated samples. Although the increase of the E_{corr} was not significant, the i_{corr} was three orders of magnitude lower than that of the untreated sample. The i_{corr} is an important parameter to evaluate the corrosion resistant properties of materials. The lower the i_{corr} , the better corrosion resistance they perform. PEO treatment improved the corrosion resistance while the multi-layer coating of both anodized and PLGA coating effectively improved the corrosion

resistance by sealing the micro-cracks and micro-pores on the outer surface oxide layer effectively and controlling the release of the magnesium ions (Y. M. Wang et al., 2009).

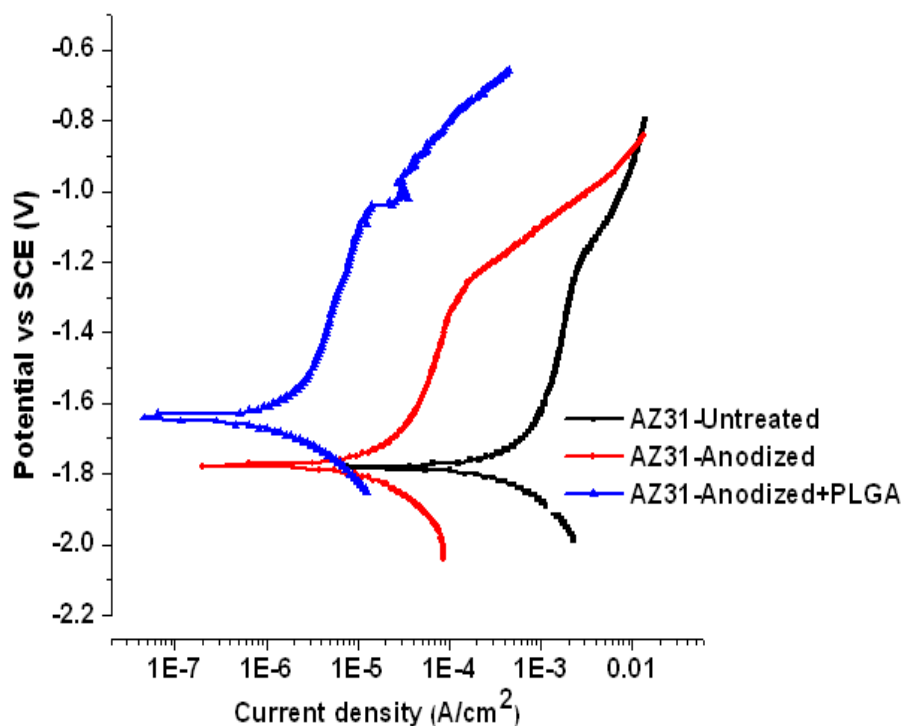


Figure 25. Potentiodynamic polarization curves of AZ31 alloy in Gamble solution.

From the measured results, the corrosion voltage was -1.78 V in the untreated Mg alloy, -1.77 V in the anodized sample and -1.64 V in the anodized+PLGA coated sample. Although corrosion potential of untreated and anodized samples remained at the same level, they have different polarization behavior, especially in anodic branch which shows the pitting corrosion behavior. The corrosion current density of the untreated, anodized and PLGA coated samples were $8.35 \times 10^{-1} \text{ mA/cm}^2$, $3.72 \times 10^{-2} \text{ mA/cm}^2$ and $2.15 \times 10^{-3} \text{ mA/cm}^2$ respectively as illustrated in Table 11. Therefore, the DC polarization curve result shows that the corrosion resistance of AZ31B magnesium alloy was greatly improved by PEO treatment and PLGA coating.

Table 11

Parameters of untreated, anodized AZ31 and anodized+ PLGA AZ31 by fitting DC polarization curve obtained in Gamble solution

AZ31 Alloy Sample	E_{corr} (V)	I_{corr} (mA/cm ²)	Corrosion rate (mpy)
Untreated	-1.78	8.35×10^{-1}	752.14
Anodized	-1.77	3.72×10^{-2}	33.51
Anodized + PLGA	-1.64	2.15×10^{-3}	0.194

Representative EIS of untreated, anodized and anodized+PLGA AZ31 alloy samples exposed to Gamble solution at 37°C are shown in Figure 26. It is evident that the impedance modulus of the untreated sample was far less than that of anodized sample while the anodized+PLGA coated sample a larger impedance modulus which confirms that PLGA coating improves the corrosion resistance of the sample by providing sealing of the micropores of the anodized sample.

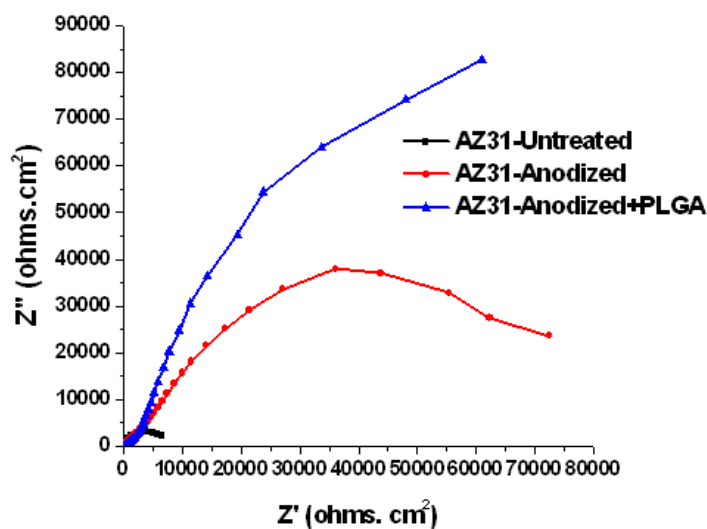


Figure 26. Nyquist plots of untreated anodized AZ31 and anodized+ PLGA coated AZ31 in Gamble solution at 37°C.

The values of the fitting circuit elements are summarized in Table 9. By combination Figure 26 and Table 12, it can be clearly seen that there is a good correlation between the experimental curves and data which are calculated from equivalent circuit. The multi-layer coating of anodization and PLGA combined proved to have a better corrosion resistance than the anodized layer by having the coating resistance (R_1) of $9388.60 \Omega\text{cm}^2$ and $6287.10 \Omega\text{cm}^2$ respectively.

Table 12

Parameters of untreated anodized and anodized + PLGA AZ31 samples obtained from EIS model carried out in Gamble solution

AZ31 Alloy Coating	$R_S (\Omega\text{cm}^2)$	$R_1 (\Omega\text{cm}^2)$	$CPE_1 (S*s^a)$	$R_2 (\Omega\text{cm}^2)$	$CPE_2 (S*s^a)$
Untreated	19.91	3925.00	–	–	9.16×10^{-6}
Anodized	28.02	6287.10	1.30×10^{-6}	6.327×10^4	425.8×10^{-9}
Anodized + PLGA	14.0×10^{-4}	9388.60	476.2×10^{-9}	1.577×10^5	1.095×10^{-6}

The surface morphology of the anodized samples was investigated by SEM which confirmed the presence of thick oxide layer on the alloy as shown in Figure 27. It is rather obvious that there exist many micropores on the surface of the coating, which is the typical feature of an anodized coated surface, and the size of pores is affected by the electrolyte types. The micro-cracks in the coating were induced by large discharge sparks caused by the vibration due to the escape and evaporation of gaseous products. The micro-pores and micro-cracks were randomly distributed in the coating surfaces which were formed by the oxygen bubbles in the coating growth process and the thermal stress due to the rapid solidification of the molten oxide in the relatively cooling electrolyte. These pores lead to poor corrosion resistance of the anodized

coating when exposed in corrosive environments (Guo, Cao, Lu, Liu, & Xu). Consequently, PLGA coating used to seal the micro-pores of the outer oxide layer of the anodized surface makes it have a compact and defect-free layer without distinct cavities and crevices. The PLGA film formed on the surface of the anodized sample can be able to prevent the outer layer of the anodized coating from being exposed directly to corrosive ions as an effective protective barrier.

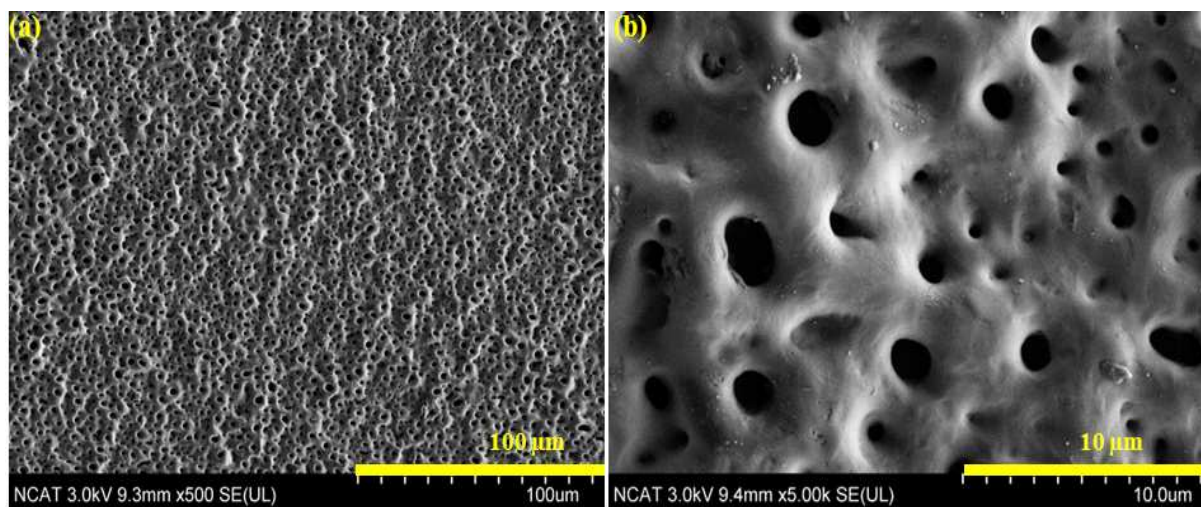


Figure 27. Surface morphologies of AZ31B anodized surface.

During the plasma electrolytic oxidation process, the applied voltages ranged from 100V-500V. The effect of applied voltage on coating corrosion resistance was various with its thickness and porosity (Zhanga, Shan, Chen, & Han, 2008). When the applied voltage was increased, the anodic reaction becomes more intense and more magnesium alloys are oxidized into various oxidations, which will make the thickness increase. When the applied voltage was low, there was no marked sparking discharge on the surface of the substrate forming smooth anodic coating with a thin transparent passive film. When the applied voltage was more than 200 V, the anodic coating was thicker and the pore size is larger with several cracks appear on the surface of the anodic coating. Thus the porosity of anodic coating increases with increasing applied voltage.

The effect of frequency was also found to affect the coating morphologies which is defined as the pulse number per second. The frequency used in this present work was between 50Hz – 100Hz using the square waveform. However, it was noted that with a higher the frequency, the shorter the time of one cycle. The continually anodizing time in one cycle decreased with the increase of frequency, which results in a good restoration of anodic coatings by electrolyte and a decrease of gas evolution (Chang et al., 2011). The porosity decreases and the corrosion resistance of anodic coatings were noticed to improve with the increase of frequency.

The poor corrosion resistance of magnesium and its alloys makes it desirable to alter its surface properties in order to improve its corrosion resistance. Various surface treatments such as electrochemical plating, conversion coating and anodization have been used to increase the corrosion resistance. PEO is one of the electrochemical surface treatment methods, which form the oxide layer on magnesium alloys in plasma state generated by applying extremely high voltage in a suitable electrolyte (Hwang, Kim, & Shin, 2009). Verdier et. al reported that the cell voltage of PEO process was important factor in the process parameter, especially influencing growth rate of oxide layer (Verdier, van der Laak, Delalande, Metson, & Dalard, 2004). The structure of the oxide layer fabricated by PEO process depends on various processing conditions, including chemical composition and concentration of electrolyte which exerts a considerable influence on the property and formation of effective oxide layer for magnesium alloy.

4.4 Cell Adhesion Assay Results

In this experiment, biocompatibility of the magnesium alloy was assessed using porcine tracheal epithelial (PTE) cells to determine the cell responses, in terms of cell morphology and cell adhesion on the surfaces of the samples after 12 hours of incubation time. Upon completion

of the adhesion assay, a phase contrast image of the glass substrate used as a control was taken using an Advanced Microscopy Group EVOS-xl digital inverted microscope to ensure the cells were still viable after the experiment as shown in Figure 28. The cells adhered to the glass substrate and were observed to be round and healthy morphology. During the initial viewing of the samples still using the optical light microscopy, an interesting finding was observed when the cells were noticed to attach on the edges on the anodized and PLGA coated samples. However, few cells were noticed to attach on the untreated samples and paclitaxel coated samples.

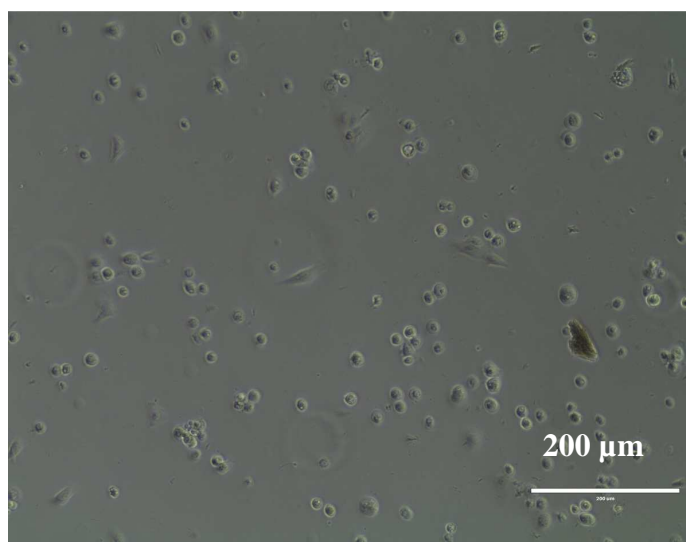


Figure 28. Optical light microscopy image showing control PTE cells attached on a glass substrate.

Figure 29 shows SEM images of cells attached to the surfaces of magnesium alloy taken after performing ion beam coating. Figure 29 (a) shows cells attached on the untreated AZ31 alloy, but did not attach well since there were areas where no cells were found on the surface. The results also demonstrated the importance of surface treatment for initial cell adhesion and for cell survival on the magnesium surfaces. Probably a shorter incubation time would have ensured more cells adhering on the surface and a long-term cell survival on the surface. The anodized surfaces however were proved to be non-toxic and biocompatible to the PTE cells because of

their three-dimensional surface as shown in Figure 29 (b). The reactivity of the magnesium was reduced by the coating which must have also helped in the adhesion of the cells. The rounded dark spots on the surface were the cells while the white areas were the anodized layer. The result indicated a healthy morphology of cells and good interaction between cells and anodized magnesium alloys surfaces.

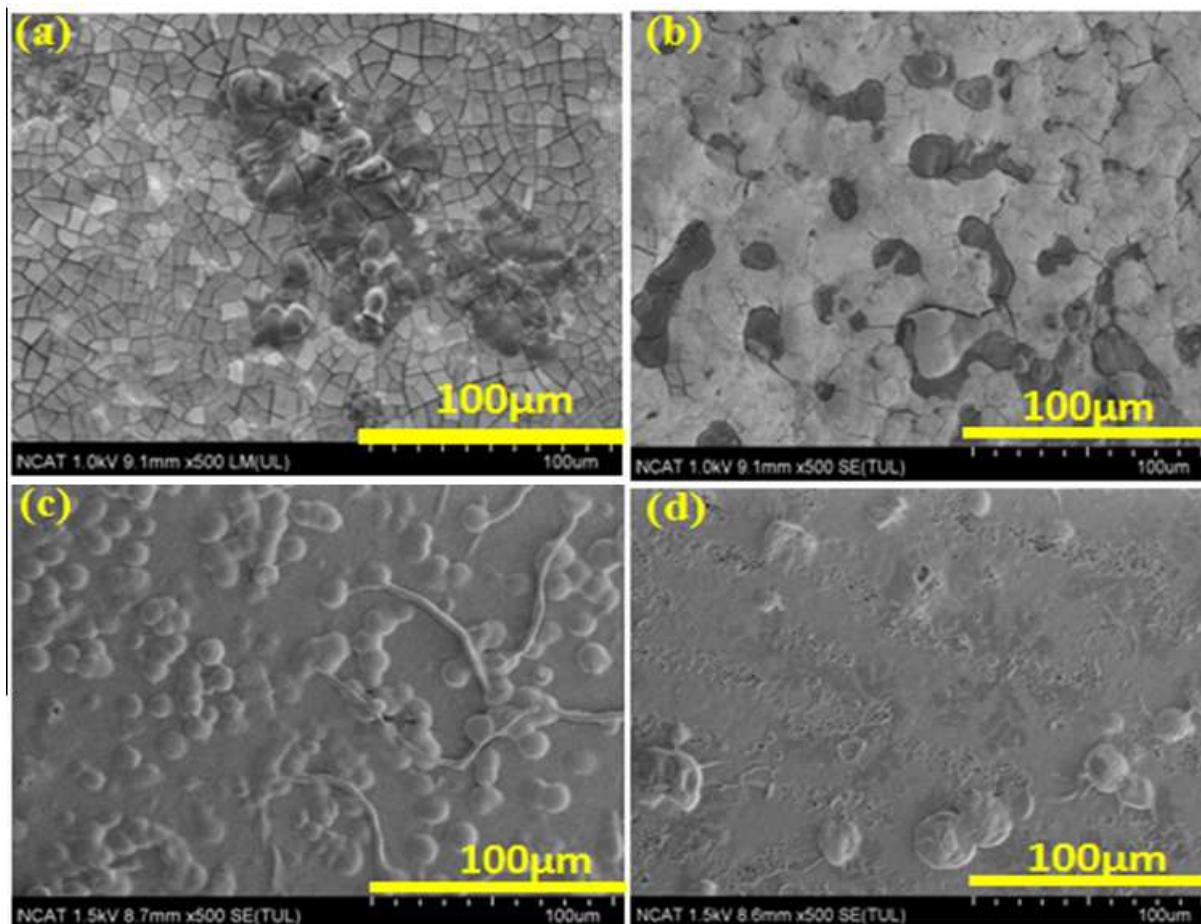


Figure 29. SEM images of PTE cells adhered on the surfaces after the cell adhesion assay for 12 hours. (a) untreated AZ31, (b) Anodized coated AZ31, (c) Untreated AZ31 coated with 2wt% PLGA and (d) untreated AZ31 coated with 2wt% PLGA with 10% paclitaxel drug.

The SEM image in Figure 29 (c) shows untreated AZ31 alloy coated with 2% wt PLGA which had a good interaction with the cells. The cells seemed to be spreading along the surface

with the morphologies being round shaped and attached closely together showing a healthy morphology attaching on the polymer. The fact that some of the cells have a spherical shape suggests that the cells are starting to detach from the surface. Figure 29 (d) shows sample coated with 2% wt PLGA+10% wt paclitaxel drug. As mention earlier, paclitaxel is an anti-cancer chemotherapy drug which exhibits a significant activity against a variety of solid tumors, including breast cancer and lung cancer. Therefore the paclitaxel-loaded PLGA coated sample released the drug to the cells during polymer breakdown. Hence because of drug, it was hard to find cells attached on the surface while the ones found had a deformed shape possibly caused by the drug.

Paclitaxel has been shown to exhibit a significant activity against a variety of solid tumors, including breast cancer, lung cancer, head and neck carcinomas (Fonseca, Simoes, & Gaspar, 2002; Spencer & Faulds, 1994; Thigpen, 2000). In vascular stent materials, loading drug in the coating on the stent can limit the early thrombogenicity. Drugs in the stent coating can be released by diffusion mechanisms or during polymer breakdown. So, a properly designed drug release coating on the stent has negligible risk of systemic toxicity (X. Wang et al., 2008).

In vitro cell culture tests can be used to screen potential bioabsorbable Mg alloys for their effects on the cells and tissue in particular physiological environments, such as bones or blood vessels. Cell adhesion has been particular interest because it plays important roles in the regulation of cell behavior in wound healing and tissue regeneration, such as the regulation of growth, differentiation, migration and survival of cells. Cell adhesion is the integrated process of multiple complex events, such as specific binding of membrane proteins with extracellular matrix (ECM) and the signal transduction. These events are strictly controlled by complicated

mechanisms and are highly interconnected and interdependent driven by ligand receptor interactions, especially integrin bindings (Arnaout, Goodman, & Xiong, 2007).

A large range of factors including hydrogen gas evolution, pH increase due to Mg dissolution in the cell culture medium, as well as the chemical and physical properties of the native or corroded magnesium surface may all have contributed to a decrease in cell adhesion and growth on the Mg substrate in comparison to glass. Dissecting those factors is possible but requires extensive experiments that go beyond the scope of this study.

CHAPTER 5

Conclusions and Future Work

This work reviews the biological performance of AZ31 magnesium alloys (biodegradable materials for temporary implant) in simulated airway surface fluid at 37°C. The corrosion behavior was studied by the analysis of corrosion resistance variation with immersion time, using electrochemical impedance spectroscopy (EIS), open circuit potential (OCP), polarization resistance and corrosion current density using potentiodynamic polarization technique. The results and morphological characterization of the samples were confirmed by x-ray computed tomography (Micro-CT), scanning electron microscopy (SEM). Chemical composition of the surface corrosion products was determined with electron dispersive x-ray spectroscopy (EDX) and X-ray diffraction (XRD).

The aim is to explore possible routes to improve limiting factors such as the corrosion resistance and improve integration of the implant with tissue, and ultimately highlights the need for further research. It is aimed to find the best magnesium alloy with low cost and low corrosion rate as implant in human body. Furthermore, the feasibility to slow down the biodegradation of magnesium alloys to solve the rapidly corroding magnesium implant problems was demonstrated by studying the effect of adding porcine stomach mucin to Gamble solution on the corrosion behavior of AZ31 alloy.

Biocompatibility of the magnesium alloy was assessed using porcine tracheal epithelial (PTE) cells to determine the cell responses, in terms of cell morphology and cell adhesion on the surfaces of the samples. A good cell interaction with the material's surface demonstrates that the magnesium implants material will possess acceptable biocompatibility and that the magnesium

ions produced from implant dissolution is not expected to lead to toxic reactions, as the concentration of magnesium in the body is controlled by homeostatic mechanisms.

The main aspects worth to emphasize are summarized as follows:

- 1) The immersion test demonstrated that thick corrosion product layer was formed on the magnesium alloy surface with the addition of carbonate ions which also induced fast passivation on the surface. The addition of porcine stomach mucin into the physiological media inhibited the corrosion rate of the samples by reducing the thickness of the corrosion products on the surface. When carbonate ions was absent in the physiological media, calcium phosphate (hydroxyapatite) was formed on the surface with more calcium element at the top of the corrosion products than bottom layer of corrosion products while the mucin inhibited the deposition of hydroxyapatite on the surface.
- 2) From the various electrochemical tests, all results confirmed that the increase in carbonate ions in the test solution caused fast precipitation of magnesium hydroxide in the corrosion product layer that can subsequently suppress development of pitting corrosion completely. Mucin was observed to increase the corrosion resistance of the samples by attaching on the sample surface hence decreasing the corrosion current densities.
- 3) pH measurements both for immersion and electrochemical tests showed a substantial increase in the pH when carbonate ions was added in the test solution while absence of carbonate caused the pH to decrease due to the formation of calcium phosphate which induced the hydrogen ions causing pH drop. The addition of mucin in the test solution attenuated magnesium induced increase in pH thereby slowing the corrosion rate of the magnesium samples.

- 4) PEO treatment led to a substantial improvement of the corrosion resistance consisting of a compact and porous layer in order to delay the initial corrosion rate of magnesium. Consequently, a multi-layer coating of PLGA coating further slowed down the initial corrosion rate by sealing all the micro-pores and cracks on the outer oxide layer effectively.
- 5) The cell adhesion assay results indicated healthy morphology of cells and good interaction between cells and AZ31 magnesium alloy. Therefore, the present *in vitro* cell assay indicates that AZ31 magnesium alloy has great potential to be used as implants/stents in biomedical applications.

The promising future of magnesium and its alloys is dependent on being able to control the rate of corrosion in body fluids. The encouraging *in vitro* results obtained in this work provides a scientific foundation which helps understand what is happening *in vivo* which was analyzed using simulated airway surface liquid. The presence of the physiological mucin concentration in the airway could be beneficial in terms of controlling the corrosion rate of the biodegradable magnesium alloy airway stent. With a novel way of controlling the concentration of mucin in the airway, the corrosion rate of a magnesium alloy implant in the airway could potentially be controlled for a specific period of time thereby fulfilling its mission and step away by degrading after tissue healing. The results therefore represent the basis for future research in evaluating magnesium as a bioresorbable airway stent.

References

- Allen, A., Hutton, D. A., Pearson, J. P., & Sellers, L. A. (1984). Mucus glycoprotein structure, gel formation and gastrointestinal mucus function. *Ciba Found Symp*, *109*, 137-156.
- Argade, G. R., Panigrahi, S. K., & Mishra, R. S. (2012). Effects of grain size on the corrosion resistance of wrought magnesium alloys containing neodymium. *Corrosion Science*, *58*, 145-151. doi: DOI 10.1016/j.corsci.2012.01.021
- Arnaut, M. A., Goodman, S. L., & Xiong, J. P. (2007). Structure and mechanics of integrin-based cell adhesion. *Current Opinion in Cell Biology*, *19*(5), 495-507. doi: DOI 10.1016/j.ceb.2007.08.002
- Arrabal, R., Matykina, E., Hashimoto, T., Skeldon, P., & Thompson, G. E. (2009). Characterization of AC PEO coatings on magnesium alloys. *Surface & Coatings Technology*, *203*(16), 2207-2220. doi: DOI 10.1016/j.surfcoat.2009.02.011
- Baril, G., & Pebere, N. (2001). The corrosion of pure magnesium in aerated and deaerated sodium sulphate solutions. *Corrosion Science*, *43*(3), 471-484. doi: Doi 10.1016/S0010-938x(00)00095-0
- Barrere, F., van der Valk, C. M., Dalmeijer, R. A. J., van Blitterswijk, C. A., de Groot, K., & Layrolle, P. (2003). In vitro and in vivo degradation of biomimetic octacalcium phosphate and carbonate apatite coatings on titanium implants. *Journal of Biomedical Materials Research Part A*, *64A*(2), 378-387. doi: Doi 10.1002/Jbm.A.10291
- Bjarnason, H., Cahill, B., Klow, N. E., Han, Y. M., Urness, M., Gunther, R., . . . Hunter, D. W. (1999). Tracheobronchial metal stents: effects of covering a bronchial ostium in pigs. *Acad Radiol*, *6*(10), 586-591.

- Blawert, C., Dietzel, W., Ghali, E., & Song, G. L. (2006). Anodizing treatments for magnesium alloys and their effect on corrosion resistance in various environments. *Advanced Engineering Materials*, 8(6), 511-533. doi: DOI 10.1002/adem.200500257
- Bouissou, C., Rouse, J. J., Price, R., & van der Walle, C. F. (2006). The influence of surfactant on PLGA microsphere glass transition and water sorption: remodeling the surface morphology to attenuate the burst release. *Pharm Res*, 23(6), 1295-1305. doi: 10.1007/s11095-006-0180-2
- Burningham, A. R., Wax, M. K., Andersen, P. E., Everts, E. C., & Cohen, J. I. (2002). Metallic tracheal stents: complications associated with long-term use in the upper airway. *Ann Otol Rhinol Laryngol*, 111(4), 285-290.
- Cao, G., & Kou, S. (2006). Hot cracking of binary Mg-Al alloy castings. *Materials Science and Engineering a-Structural Materials Properties Microstructure and Processing*, 417(1-2), 230-238. doi: DOI 10.1016/j.msea.2005.10.050
- Chang, L. R., Cao, F. H., Cai, J. S., Liu, W. J., Zhang, Z., & Zhang, J. Q. (2011). Influence of electric parameters on MAO of AZ91D magnesium alloy using alternative square-wave power source. *Transactions of Nonferrous Metals Society of China*, 21(2), 307-316. doi: Doi 10.1016/S1003-6326(11)60714-0
- Chino, Y., Kado, M., & Mabuchi, M. (2008). Compressive deformation behavior at room temperature-773 K 14 in Mg-0.2 mass%(0.035at.%)Ce alloy. *Acta Materialia*, 56(3), 387-394. doi: DOI 10.1016/j.actamat.2007.09.036
- Chiu, K. Y., Wong, M. H., Cheng, F. T., & Man, H. C. (2007). Characterization and corrosion studies of fluoride conversion coating on degradable Mg implants. *Surface & Coatings Technology*, 202(3), 590-598. doi: DOI 10.1016/j.surfcoat.2007.06.035

- Collard, P., Freitag, L., Reynaert, M. S., Rodenstein, D. O., & Francis, C. (1996). Respiratory failure due to tracheobronchomalacia. *Thorax*, *51*(2), 224-226. doi: Doi 10.1136/Thx.51.2.224
- Colombo, A., & Karvouni, E. (2000). Biodegradable stents : "fulfilling the mission and stepping away". *Circulation*, *102*(4), 371-373.
- Diamond, J. M. (1979). Osmotic water flow in leaky epithelia. *J Membr Biol*, *51*(3-4), 195-216.
- Djordjevic, M. B., & Schmid-Fetzer, R. (2006). Thermodynamic calculation as a tool for thixoforming alloy and process development. *Materials Science and Engineering a-Structural Materials Properties Microstructure and Processing*, *417*(1-2), 24-33. doi: DOI 10.1016/j.msea.2005.08.227
- Duan, H. P., Yan, C. W., & Wang, F. H. (2007). Growth process of plasma electrolytic oxidation films formed on magnesium alloy AZ91D in silicate solution. *Electrochimica Acta*, *52*(15), 5002-5009. doi: DOI 10.1016/j.electacta.2007.02.021
- Dube, L., & Granry, J. C. (2003). The therapeutic use of magnesium in anesthesiology, intensive care and emergency medicine: a review. *Canadian Journal of Anaesthesia-Journal Canadien D Anesthesie*, *50*(7), 732-746.
- Dumon, J. F. (1990). A Dedicated Tracheobronchial Stent. *Chest*, *97*(2), 328-332.
- Elliott, M., Roebuck, D., Noctor, C., McLaren, C., Hartley, B., Mok, Q., . . . Wallis, C. (2003). The management of congenital tracheal stenosis. *International Journal of Pediatric Otorhinolaryngology*, *67*, S183-S192. doi: DOI 10.1016/j.ijporl.2003.08.023
- Erne, P., Schier, M., & Resink, T. J. (2006). The road to bioabsorbable stents: reaching clinical reality? *Cardiovasc Intervent Radiol*, *29*(1), 11-16. doi: 10.1007/s00270-004-0341-9

- Fonseca, C., Simoes, S., & Gaspar, R. (2002). Paclitaxel-loaded PLGA nanoparticles: preparation, physicochemical characterization and in vitro anti-tumoral activity. *Journal of Controlled Release*, 83(2), 273-286. doi: Pii S0168-3659(02)00212-2
Doi 10.1016/S0168-3659(02)00212-2
- Ghasemi, A., Raja, V. S., Blawert, C., Dietzel, W., & Kainer, K. U. (2008). Study of the structure and corrosion behavior of PEO coatings on AM50 magnesium alloy by electrochemical impedance spectroscopy. *Surface & Coatings Technology*, 202(15), 3513-3518. doi: DOI 10.1016/j.surfcoat.2007.12.033
- Goh, C. S., Wei, J., Lee, L. C., & Gupta, M. (2006). Development of novel carbon nanotube reinforced magnesium nanocomposites using the powder metallurgy technique. *Nanotechnology*, 17(1), 7-12. doi: Doi 10.1088/0957-4484/17/1/002
- Gottlieb, J., Fuehner, T., Dierich, M., Wiesner, O., Simon, A. R., & Welte, T. (2009). Are metallic stents really safe? A long-term analysis in lung transplant recipients. *European Respiratory Journal*, 34(6), 1417-1422. doi: Doi 10.1183/09031936.00041909
- Gray, J. E., & Luan, B. (2002). Protective coatings on magnesium and its alloys - a critical review. *Journal of Alloys and Compounds*, 336(1-2), 88-113.
- Grillo, H. C., Donahue, D. M., Mathisen, D. J., Wain, J. C., & Wright, C. D. (1995). Postintubation Tracheal Stenosis - Treatment and Results. *Journal of Thoracic and Cardiovascular Surgery*, 109(3), 486-493. doi: Doi 10.1016/S0022-5223(95)70279-2
- Guo, M., Cao, L., Lu, P., Liu, Y., & Xu, X. Anticorrosion and cytocompatibility behavior of MAO/PLLA modified magnesium alloy WE42. *J Mater Sci Mater Med*, 22(7), 1735-1740. doi: 10.1007/s10856-011-4354-z

- Hamdy, A. S., El-Shenawy, E., & El-Bitar, T. (2006). Electrochemical Impedance Spectroscopy Study of the Corrosion Behavior of Some Niobium Bearing Stainless Steels in 3.5% NaCl. *International Journal of Electrochemical Science*, 1(4), 171-180.
- Han, L. H., Hu, H., Northwood, D. O., & Li, N. Y. (2008). Microstructure and nano-scale mechanical behavior of Mg-Al and Mg-Al-Ca alloys. *Materials Science and Engineering a-Structural Materials Properties Microstructure and Processing*, 473(1-2), 16-27. doi: DOI 10.1016/j.msea.2007.03.053
- Hassan, S. F., & Gupta, M. (2003). Development of high strength magnesium copper based hybrid composites with enhanced tensile properties. *Materials Science and Technology*, 19(2), 253-259. doi: Doi 10.1179/026708303225009346
- Heublein, B., Rohde, R., Kaese, V., Niemeyer, M., Hartung, W., & Haverich, A. (2003). Biocorrosion of magnesium alloys: a new principle in cardiovascular implant technology? *Heart*, 89(6), 651-656.
- Hitachi. (2012). SU8000 Detector System: Variety of Signal Detection System (pp. 1). North Carolina: Hitachi.
- Hsiao, H. Y., & Tsai, W. T. (2005). Characterization of anodic films formed on AZ91D magnesium alloy. *Surface & Coatings Technology*, 190(2-3), 299-308. doi: DOI 10.1016/j.surfcoat.2004.03.010
- Hsiao, H. Y., Tsung, H. C., & Tsai, W. T. (2005). Anodization of AZ91D magnesium alloy in silicate-containing electrolytes. *Surface & Coatings Technology*, 199(2-3), 127-134. doi: DOI 10.1016/j.surfcoat.2004.12.010

- Hwang, D. Y., Kim, Y. A., & Shin, D. H. (2009). Corrosion Resistance of Plasma-Anodized AZ91 Mg Alloy in the Electrolyte with/without Potassium Fluoride. *Materials Transactions*, 50(3), 671-678. doi: DOI 10.2320/matertrans.MER2008345
- Inoue, H., Sugahara, K., Yamamoto, A., & Tsubakino, H. (2002). Corrosion rate of magnesium and its alloys in buffered chloride solutions. *Corrosion Science*, 44(3), 603-610. doi: Doi 10.1016/S0010-938x(01)00092-0
- Jacobs, J. J., Gilbert, J. L., & Urban, R. M. (1998). Corrosion of metal orthopaedic implants. *Journal of Bone and Joint Surgery-American Volume*, 80A(2), 268-282.
- Jain, R. A. (2000). The manufacturing techniques of various drug loaded biodegradable poly(lactide-co-glycolide) (PLGA) devices. *Biomaterials*, 21(23), 2475-2490. doi: Doi 10.1016/S0142-9612(00)00115-0
- Jayaraman, S., Song, Y., Vetrivel, L., Shankar, L., & Verkman, A. S. (2001). Noninvasive in vivo fluorescence measurement of airway-surface liquid depth, salt concentration, and pH. *Journal of Clinical Investigation*, 107(3), 317-324. doi: 10.1172/JCI11154
- Jeffery, P. K., & Li, D. (1997). Airway mucosa: secretory cells, mucus and mucin genes. *European Respiratory Journal*, 10(7), 1655-1662.
- Joris, L., Dab, I., & Quinton, P. M. (1993). Elemental composition of human airway surface fluid in healthy and diseased airways. *American Review of Respiratory Disease*, 148(6 Pt 1), 1633-1637.
- Knowles, M. R., & Boucher, R. C. (2002). Mucus clearance as a primary innate defense mechanism for mammalian airways. *Journal of Clinical Investigation*, 109(5), 571-577. doi: Doi 10.1172/Jci200215217

- Kuwahara, H., Al-Abdullat, Y., Ohta, M., Tsutsumi, S., Ikeuchi, K., Mazaki, N., & Aizawa, T. (2000). Surface reaction of magnesium in Hank's solutions. *Magnesium Alloys 2000*, 350-3, 349-358.
- Lee, E. Y. (2008). Advancing CT and MR imaging of the lungs and airways in children: imaging into practice. *Pediatric Radiology*, 38, S208-S212. doi: DOI 10.1007/s00247-008-0767-3
- Levine, M. J., Reddy, M. S., Tabak, L. A., Loomis, R. E., Bergey, E. J., Jones, P. C., . . . Al-Hashimi, I. (1987). Structural aspects of salivary glycoproteins. *J Dent Res*, 66(2), 436-441.
- Liang, J., Srinivasan, P. B., Blawert, C., & Dietzel, W. (2009). Comparison of electrochemical corrosion behaviour of MgO and ZrO₂ coatings on AM50 magnesium alloy formed by plasma electrolytic oxidation. *Corrosion Science*, 51(10), 2483-2492. doi: DOI 10.1016/j.corsci.2009.06.034
- Liang, J., Srinivasan, P. B., Blawert, C., & Dietzel, W. (2010). Influence of pH on the deterioration of plasma electrolytic oxidation coated AM50 magnesium alloy in NaCl solutions. *Corrosion Science*, 52(2), 540-547. doi: DOI 10.1016/j.corsci.2009.10.011
- Lindstrom, R., Johansson, L. G., & Svensson, J. E. (2003). The influence of NaCl and CO₂ on the atmospheric corrosion of magnesium alloy AZ91. *Materials and Corrosion-Werkstoffe Und Korrosion*, 54(8), 587-594. doi: DOI 10.1002/maco.200390130
- Liu, C. L., Wang, Y. J., Zeng, R. C., Zhang, X. M., Huang, W. J., & Chu, P. K. (2010). In vitro corrosion degradation behaviour of Mg-Ca alloy in the presence of albumin. *Corrosion Science*, 52(10), 3341-3347. doi: DOI 10.1016/j.corsci.2010.06.003
- Macdonald, J. R. (2005). Impedance spectroscopy: Models, data fitting, and analysis. *Solid State Ionics*, 176(25-28), 1961-1969. doi: DOI 10.1016/j.ssi.2004.05.035

- Makadia, H. K., & Siegel, S. J. (2011). Poly Lactic-co-Glycolic Acid (PLGA) as Biodegradable Controlled Drug Delivery Carrier. *Polymers (Basel)*, 3(3), 1377-1397. doi: 10.3390/polym3031377
- Makar, G. L., & Kruger, J. (1993). Corrosion of Magnesium. *International Materials Reviews*, 38(3), 138-153.
- Marques, M. R. C., Loebenberg, R., & Almukainzi, M. (2011). Simulated Biological Fluids with Possible Application in Dissolution Testing. *Dissolution Technologies*, 18(3), 15-28.
- Miller, W. K. (1993). Stress-corrosion Cracking. *ASM*, 251.
- Mizutani, Y., Kim, S. J., Ichino, R., & Okido, M. (2003). Anodizing of Mg alloys in alkaline solutions. *Surface & Coatings Technology*, 169, 143-146.
- Mordike, B. L., & Ebert, T. (2001). Magnesium - Properties - applications - potential. *Materials Science and Engineering a-Structural Materials Properties Microstructure and Processing*, 302(1), 37-45. doi: Doi 10.1016/S0921-5093(00)01351-4
- Murgu, S. D., & Colt, H. G. (2006). Tracheobronchomalacia and excessive dynamic airway collapse. *Respirology*, 11(4), 388-406. doi: DOI 10.1111/j.1400-1843.2006.00862.x
- Nguyen, Q. B., Gupta, M., & Srivatsan, T. S. (2009). On the role of nano-alumina particulate reinforcements in enhancing the oxidation resistance of magnesium alloy AZ31B. *Materials Science and Engineering a-Structural Materials Properties Microstructure and Processing*, 500(1-2), 233-237. doi: DOI 10.1016/j.msea.2008.09.050
- Nuutinen, J. (1977). Acquired tracheobronchomalacia. A clinical study with bronchological correlations. *Ann Clin Res*, 9(6), 350-355.
- Offner, G. D., & Troxler, R. F. (2000). Heterogeneity of high-molecular-weight human salivary mucins. *Adv Dent Res*, 14, 69-75.

- Pan, C. J., Tang, J. J., Shao, Z. Y., Wang, J., & Huang, N. (2007). Improved blood compatibility of rapamycin-eluting stent by incorporating curcumin. *Colloids and Surfaces B-Biointerfaces*, 59(1), 105-111. doi: DOI 10.1016/j.colsurfb.2007.04.015
- Pan, C. J., Tang, J. J., Weng, Y. J., Wang, J., & Huang, N. (2007). Preparation and characterization of rapamycin-loaded PLGA coating stent. *Journal of Materials Science-Materials in Medicine*, 18(11), 2193-2198. doi: DOI 10.1007/s10856-007-3075-9
- Park, T. G. (1994). Degradation of Poly(D,L-Lactic Acid) Microspheres - Effect of Molecular-Weight. *Journal of Controlled Release*, 30(2), 161-173. doi: Doi 10.1016/0168-3659(94)90263-1
- Pietak, A., Mahoney, P., Dias, G. J., & Staiger, M. P. (2008). Bone-like matrix formation on magnesium and magnesium alloys. *Journal of Materials Science-Materials in Medicine*, 19(1), 407-415. doi: DOI 10.1007/s10856-007-3172-9
- Prasad, Y. R. K., Rao, K. P., & Gupta, M. (2009). Hot workability and deformation mechanisms in Mg/nano-Al₂O₃ composite. *Composites Science and Technology*, 69(7-8), 1070-1076. doi: DOI 10.1016/j.compscitech.2009.01.032
- Przylusk.J, & Palka, E. (1970). Study of Kinetics of Anodic Oxydation of Magnesium in a Ammonium Chloride Solution. *Electrochimica Acta*, 15(5), 853-&. doi: Doi 10.1016/0013-4686(70)90050-2
- Quach, N. C., Uggowitzer, P. J., & Schmutz, P. (2008). Corrosion behaviour of an Mg-Y-RE alloy used in biomedical applications studied by electrochemical techniques. *Comptes Rendus Chimie*, 11(9), 1043-1054. doi: DOI 10.1016/j.crci.2008.06.007

- Riemelmoser, F. O., Kuhlein, M., Kilian, H., Kettner, M., Hanzi, A. C., & Uggowitz, P. J. (2007). Micro-alloyed wrought magnesium for room-temperature forming. *Advanced Engineering Materials*, 9(9), 799-802. doi: DOI 10.1002/adem.200700161
- Rose, M. C., & Voynow, J. A. (2006). Respiratory tract mucin genes and mucin glycoproteins in health and disease. *Physiol Rev*, 86(1), 245-278. doi: 86/1/245 [pii] 10.1152/physrev.00010.2005
- Satoh, S., Hinoda, Y., Hayashi, T., Burdick, M. D., Imai, K., & Hollingsworth, M. A. (2000). Enhancement of metastatic properties of pancreatic cancer cells by MUC1 gene encoding an anti-adhesion molecule. *Int J Cancer*, 88(4), 507-518. doi: 10.1002/1097-0215(20001115)88:4<507::AID-IJC1>3.0.CO;2-0 [pii]
- Schliecker, G., Schmidt, C., Fuchs, S., Wombacher, R., & Kissel, T. (2003). Hydrolytic degradation of poly(lactide-co-glycolide) films: effect of oligomers on degradation rate and crystallinity. *International Journal of Pharmaceutics*, 266(1-2), 39-49. doi: Doi 10.1016/S0378-5173(03)00379-X
- Smith, L. J., Swaim, J. S., Yao, C., Haberstroh, K. M., Nauman, E. A., & Webster, T. J. (2007). Increased osteoblast cell density on nanostructured PLGA-coated nanostructured titanium for orthopedic applications. *Int J Nanomedicine*, 2(3), 493-499.
- Song, G., Atrens, A., Stjohn, D., Nairn, J., & Li, Y. (1997). The electrochemical corrosion of pure magnesium in 1 N NaCl. *Corrosion Science*, 39(5), 855-875. doi: Doi 10.1016/S0010-938x(96)00172-2
- Song, G. L., & Atrens, A. (1999). Corrosion mechanisms of magnesium alloys. *Advanced Engineering Materials*, 1(1), 11-33. doi: Doi 10.1002/(Sici)1527-2648(199909)1:1<11::Aid-Adem11>3.3.Co;2-E

- Song, G. L., & Atrens, A. (2003). Understanding magnesium corrosion - A framework for improved alloy performance. *Advanced Engineering Materials*, 5(12), 837-858. doi: DOI 10.1002/adem.200310405
- Song, G. L., Bowles, A. L., & StJohn, D. H. (2004). Corrosion resistance of aged die cast magnesium alloy AZ91D. *Materials Science and Engineering a-Structural Materials Properties Microstructure and Processing*, 366(1), 74-86. doi: DOI 10.1016/j.msea.2003.08.060
- Song, G. L., & Song, S. Z. (2007). A possible biodegradable magnesium implant material. *Advanced Engineering Materials*, 9(4), 298-302.
- Spencer, C. M., & Faulds, D. (1994). Paclitaxel - a Review of Its Pharmacodynamic and Pharmacokinetic Properties and Therapeutic Potential in the Treatment of Cancer. *Drugs*, 48(5), 794-847. doi: Doi 10.2165/00003495-199448050-00009
- Spittle, N., & McCluskey, A. (2000). Lesson of the week: tracheal stenosis after intubation. *BMJ*, 321(7267), 1000-1002.
- Srinivasan, P. B., Liang, J., Blawert, C., Stormer, M., & Dietzel, W. (2010). Characterization of calcium containing plasma electrolytic oxidation coatings on AM50 magnesium alloy. *Applied Surface Science*, 256(12), 4017-4022. doi: DOI 10.1016/j.apsusc.2010.01.069
- Staiger, M. P., Pietak, A. M., Huadmai, J., & Dias, G. (2006). Magnesium and its alloys as orthopedic biomaterials: A review. *Biomaterials*, 27(9), 1728-1734. doi: DOI 10.1016/j.biomaterials.2005.10.003
- Stamenkovic, S., Hierner, R., De Leyn, P., & Delaere, P. (2007). Long-segment tracheal stenosis treated with vascularized mucosa and short-term stenting. *Annals of Thoracic Surgery*, 83(3), 1213-1215. doi: DOI 10.1016/j.athoracsur.2006.04.027

- Tabak, L. A. (1995). In Defense of the Oral Cavity - Structure, Biosynthesis and Function of Salivary Mucins. *Annual Review of Physiology*, 57, 547-564. doi: DOI 10.1146/annurev.physiol.57.1.547
- Tan, A. L. K., Soutar, A. M., Annergren, I. F., & Liu, Y. N. (2005). Multilayer sol-gel coatings for corrosion protection of magnesium. *Surface & Coatings Technology*, 198(1-3), 478-482. doi: DOI 10.1016/j.surfcoat.2004.10.066
- Tarran, R., Grubb, B. R., Gatzky, J. T., Davis, C. W., & Boucher, R. C. (2001). The relative roles of passive surface forces and active ion transport in the modulation of airway surface liquid volume and composition. *J Gen Physiol*, 118(2), 223-236.
- Thigpen, J. T. (2000). Chemotherapy for advanced ovarian cancer: overview of randomized trials. *Semin Oncol*, 27(3 Suppl 7), 11-16.
- Thomann, M., Krause, C., Angrisani, N., Bormann, D., Hassel, T., Windhagen, H., & Meyer-Lindenberg, A. (2010). Influence of a magnesium-fluoride coating of magnesium-based implants (MgCa0.8) on degradation in a rabbit model. *Journal of Biomedical Materials Research Part A*, 93A(4), 1609-1619. doi: Doi 10.1002/Jbm.A.32639
- Thornton, D. J., Rousseau, K., & McGuckin, M. A. (2008). Structure and function of the polymeric mucins in airways mucus. *Annual Review of Physiology*, 70, 459-486. doi: 10.1146/annurev.physiol.70.113006.100702
- Tomozawa, M., & Hiromoto, S. (2011). Microstructure of hydroxyapatite- and octacalcium phosphate-coatings formed on magnesium by a hydrothermal treatment at various pH values. *Acta Materialia*, 59(1), 355-363. doi: DOI 10.1016/j.actamat.2010.09.041
- Tsuji, H., Mizuno, A., & Ikada, Y. (2000). Properties and morphology of poly(L-lactide). III. Effects of initial crystallinity on long-term in vitro hydrolysis of high molecular weight

- poly(L-lactide) film in phosphate-buffered solution. *Journal of Applied Polymer Science*, 77(7), 1452-1464. doi: Doi 10.1002/1097-4628(20000815)77:7<1452::Aid-App7>3.0.Co;2-S
- Verdier, S., van der Laak, N., Delalande, S., Metson, J., & Dalard, F. (2004). The surface reactivity of a magnesium-aluminium alloy in acidic fluoride solutions studied by electrochemical techniques and XPS. *Applied Surface Science*, 235(4), 513-524. doi: DOI 10.1016/j.apsusc.2004.03.250
- Vijh, A. K. (1971). Sparking Voltages and Side Reactions during Anodization of Valve Metals in Terms of Electron Tunnelling. *Corrosion Science*, 11(6), 411-&. doi: Doi 10.1016/S0010-938x(71)80125-7
- Wang, X., Zhang, X., Castellot, J., Herman, I., Iafrati, M., & Kaplan, D. L. (2008). Controlled release from multilayer silk biomaterial coatings to modulate vascular cell responses. *Biomaterials*, 29(7), 894-903. doi: DOI 10.1016/j.biomaterials.2007.10.055
- Wang, Y. M., Wang, F. H., Xu, M. J., Zhao, B., Guo, L. X., & Ouyang, J. H. (2009). Microstructure and corrosion behavior of coated AZ91 alloy by microarc oxidation for biomedical application. *Applied Surface Science*, 255(22), 9124-9131. doi: DOI 10.1016/j.apsusc.2009.06.116
- Webb, E. M., Elicker, B. M., & Webb, W. R. (2000). Using CT to diagnose nonneoplastic tracheal abnormalities: Appearance of the tracheal wall. *American Journal of Roentgenology*, 174(5), 1315-1321.
- Widdicombe, J. H. (2002). Regulation of the depth and composition of airway surface liquid. *J Anat*, 201(4), 313-318.

- Winters, S. L., & Yeates, D. B. (1997). Roles of hydration, sodium, and chloride in regulation of canine mucociliary transport system. *Journal of Applied Physiology*, 83(4), 1360-1369.
- Winzer, N., Atrens, A., Song, G. L., Ghali, E., Dietzel, W., Kainer, K. U., . . . Blawert, C. (2005). A critical review of the stress corrosion cracking (SCC) of magnesium alloys. *Advanced Engineering Materials*, 7(8), 659-693. doi: DOI 10.1002/adem.200500071
- Witte, F. (2010a). The history of biodegradable magnesium implants: A review. *Acta Biomaterialia*, 6(5), 1680-1692. doi: DOI 10.1016/j.actbio.2010.02.028
- Witte, F. (2010b). The history of biodegradable magnesium implants: a review. *Acta Biomater*, 6(5), 1680-1692. doi: S1742-7061(10)00096-6 [pii]
10.1016/j.actbio.2010.02.028
- Witte, F., Fischer, J., Nellesen, J., Crostack, H. A., Kaese, V., Pisch, A., . . . Windhagen, H. (2006). In vitro and in vivo corrosion measurements of magnesium alloys. *Biomaterials*, 27(7), 1013-1018. doi: DOI 10.1016/j.biomaterials.2005.07.037
- Witte, F., Kaese, V., Haferkamp, H., Switzer, E., Meyer-Lindenberg, A., Wirth, C. J., & Windhagen, H. (2005). In vivo corrosion of four magnesium alloys and the associated bone response. *Biomaterials*, 26(17), 3557-3563.
- Wood, D. E. (2001). Airway stenting. *Chest Surg Clin N Am*, 11(4), 841-860.
- Wu, C. S., Zhang, Z., Cao, F. H., Zhang, L. J., Zhang, J. Q., & Cao, C. N. (2007). Study on the anodizing of AZ31 magnesium alloys in alkaline borate solutions. *Applied Surface Science*, 253(8), 3893-3898. doi: DOI 10.1016/j.apsusc.2006.08.020
- Xin, Y. C., Liu, C. L., Zhang, X. M., Tang, G. Y., Tian, X. B., & Chu, P. K. (2007). Corrosion behavior of biomedical AZ91 magnesium alloy in simulated body fluids. *Journal of Materials Research*, 22(7), 2004-2011. doi: Doi 10.1557/Jmr.2007.0233

- Zeng, R. C., Zhang, J., Huang, W. J., Dietzel, W., Kainer, K. U., Blawert, C., & Ke, W. (2006). Review of Studies on Corrosion of Magnesium Alloys. *Transactions of Nonferrous Metals Society of China*, 16, S763-S771.
- Zhang, E. L., Yin, D. S., Xu, L. P., Yang, L., & Yang, K. (2009). Microstructure, mechanical and corrosion properties and biocompatibility of Mg-Zn-Mn alloys for biomedical application. *Materials Science & Engineering C-Biomimetic and Supramolecular Systems*, 29(3), 987-993.
- Zhang, W., Tian, B., Du, K. Q., Zhang, H. X., & Wang, F. H. (2011). Preparation and Corrosion Performance of PEO Coating With Low Porosity on Magnesium Alloy AZ91D In Acidic KF System. *International Journal of Electrochemical Science*, 6(11), 5228-5248.
- Zhang, Y. J., Yan, C. W., Wang, F. H., & Li, W. F. (2005). Electrochemical behavior of anodized Mg alloy AZ91D in chloride containing aqueous solution. *Corrosion Science*, 47(11), 2816-2831. doi: DOI 10.1016/j.corsci.2005.01.010
- Zhang, R. F., Shan, D. Y., Chen, R. S., & Han, E. H. (2008). Effects of electric parameters on properties of anodic coatings formed on magnesium alloys. *Materials Chemistry and Physics*, 107(2-3), 356-363. doi: DOI 10.1016/j.matchemphys.2007.07.027
- Zreiqat, H., Howlett, C. R., Zannettino, A., Evans, P., Schulze-Tanzil, G., Knabe, C., & Shakibaei, M. (2002). Mechanisms of magnesium-stimulated adhesion of osteoblastic cells to commonly used orthopaedic implants. *Journal of Biomedical Materials Research*, 62(2), 175-184.
- Zucchi, F., Frignani, A., Grassi, V., Balbo, A., & Trabaneli, G. (2008). Organo-silane coatings for AZ31 magnesium alloy corrosion protection. *Materials Chemistry and Physics*, 110(2-3), 263-268. doi: DOI 10.1016/j.matchemphys.2008.02.015

Zuo, Y., Zhao, P. H., & Zhao, J. M. (2003). The influences of sealing methods on corrosion behavior of anodized aluminum alloys in NaCl solutions. *Surface & Coatings Technology*, 166(2-3), 237-242. doi: Pii S0257-8972(02)00779-X

Doi 10.1016/S0257-8972(02)00779-X

Appendix

0g/ HCO_3^- and 0ml/ml Mucin		1g/ HCO_3^- and 0ml/ml Mucin		2.6g/ HCO_3^- and 0ml/ml Mucin		4g/ HCO_3^- and 0ml/ml Mucin	
0.03g/ HCO_3^- and 0.03 ml/ml Mucin		1g/ HCO_3^- and 0.03 ml/ml Mucin		2.6g/ HCO_3^- and 0.03 ml/ml Mucin		4g/ HCO_3^- and 0.03 ml/ml Mucin	
0.1g/ HCO_3^- and 0.1 ml/ml Mucin		1g/ HCO_3^- and 0.1 ml/ml Mucin		2.6g/ HCO_3^- and 0.1 ml/ml Mucin		4g/ HCO_3^- and 0.1 ml/ml Mucin	

Figure 30. Optical images of AZ31B before immersion test













0g/l HCO ₃ ⁻ and 0ml/ml Mucin	1g/l HCO ₃ ⁻ and 0ml/ml Mucin	2.5g/l HCO ₃ ⁻ and 0ml/ml Mucin	4g/l HCO ₃ ⁻ and 0ml/ml Mucin
			
0 g/l HCO ₃ ⁻ and 0.03 ml/ml Mucin	1 g/l HCO ₃ ⁻ and 0.03 ml/ml Mucin	2.5 g/l HCO ₃ ⁻ and 0.03 ml/ml Mucin	4 g/l HCO ₃ ⁻ and 0.03 ml/ml Mucin
			
0g/l HCO ₃ ⁻ and 0.1 ml/ml Mucin	1g/l HCO ₃ ⁻ and 0.1 ml/ml Mucin	2.5 g/l HCO ₃ ⁻ and 0.1 ml/ml Mucin	4 g/l HCO ₃ ⁻ and 0.1 ml/ml Mucin
			

Figure 31. Optical images of corroded AZ31B after 3 days immersion test in Gamble solutions



Figure 32. Optical images of corroded AZ31B after 10 days immersion test in Gamble solutions

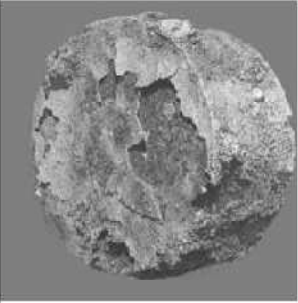

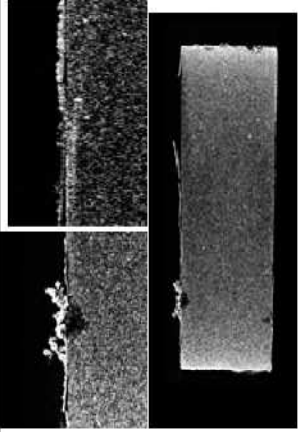

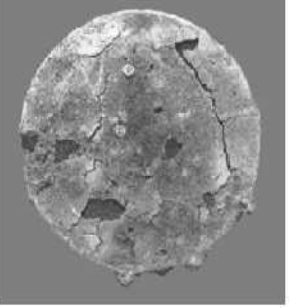
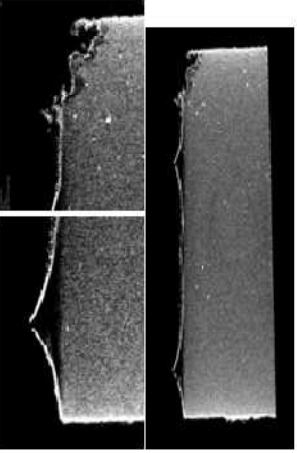
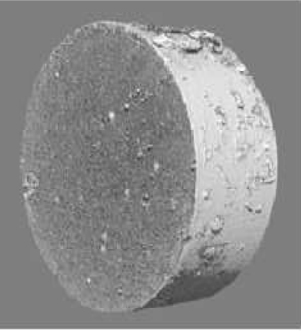
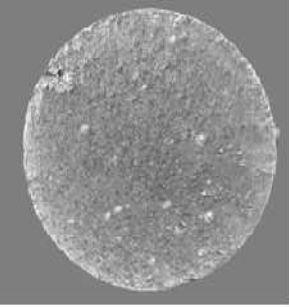
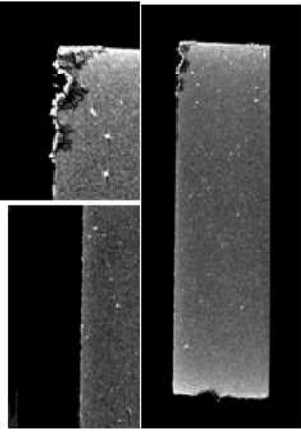
Sample	Left Corner	Up	Cross-section
0g/L HCO_3^- , 0g/L Mucin			
0g/L HCO_3^- , 0.03g/L Mucin			
0g/L HCO_3^- , 0.1g/L Mucin			

Figure 33. CT data after immersion showing effect of increasing mucin without HCO_3^- in Gamble solution for 10 days

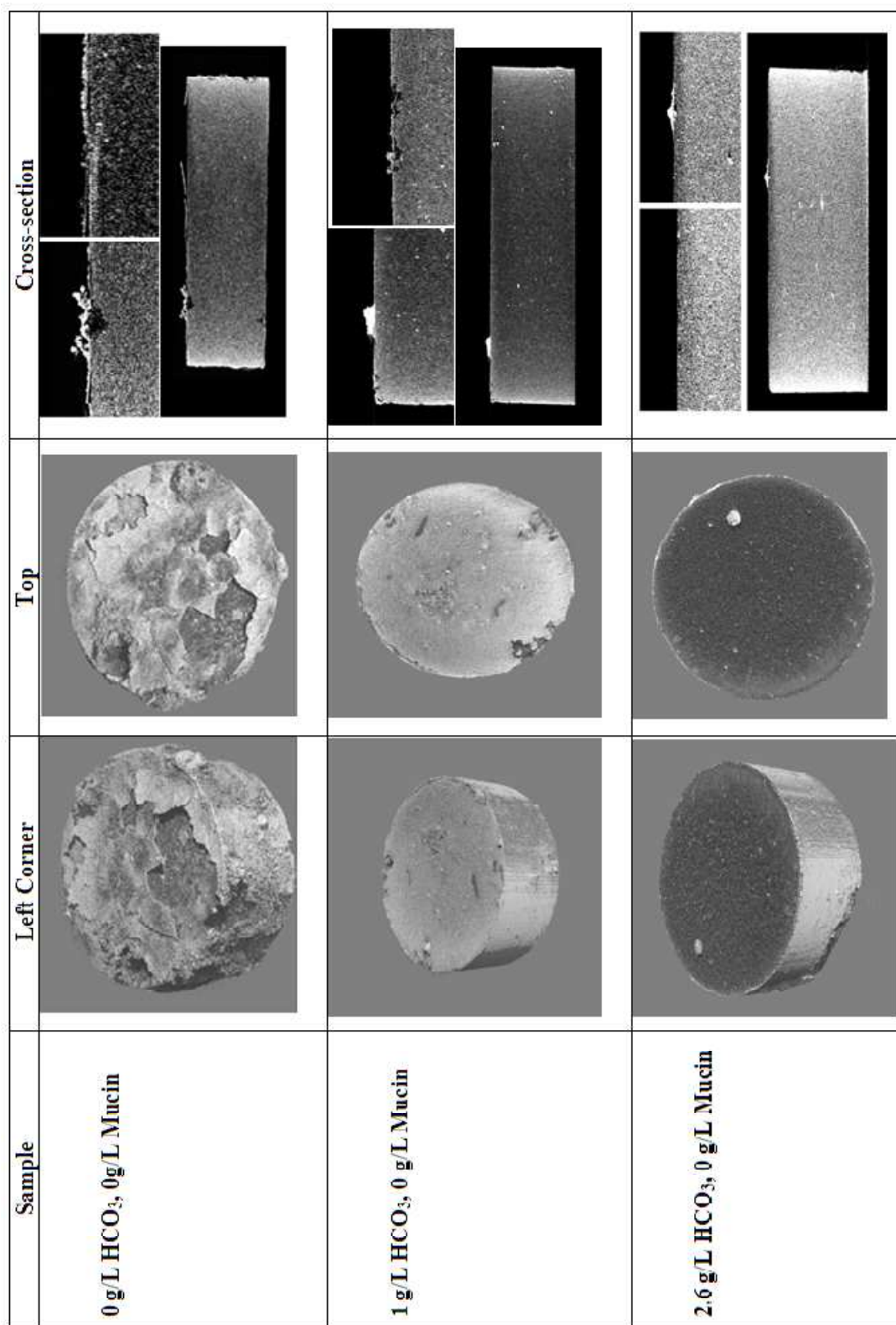


Figure 34. CT data immersion showing effect of increasing HCO_3^- ions in Gamble solution for 10 days

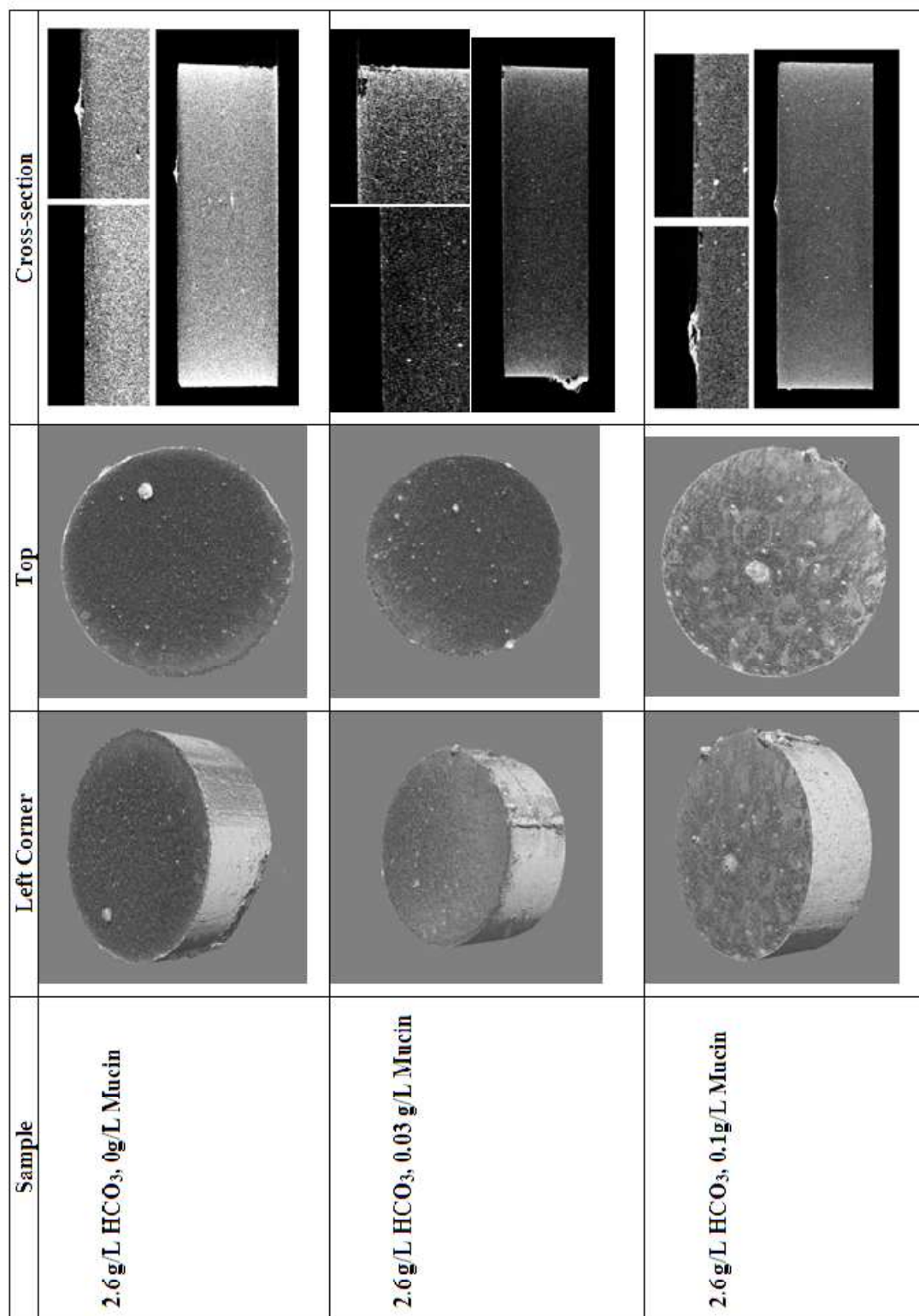


Figure 35. CT data after 10 days immersion showing effect of increasing mucin in Gamble solution containing 2.6 g/l

HCO_3^-

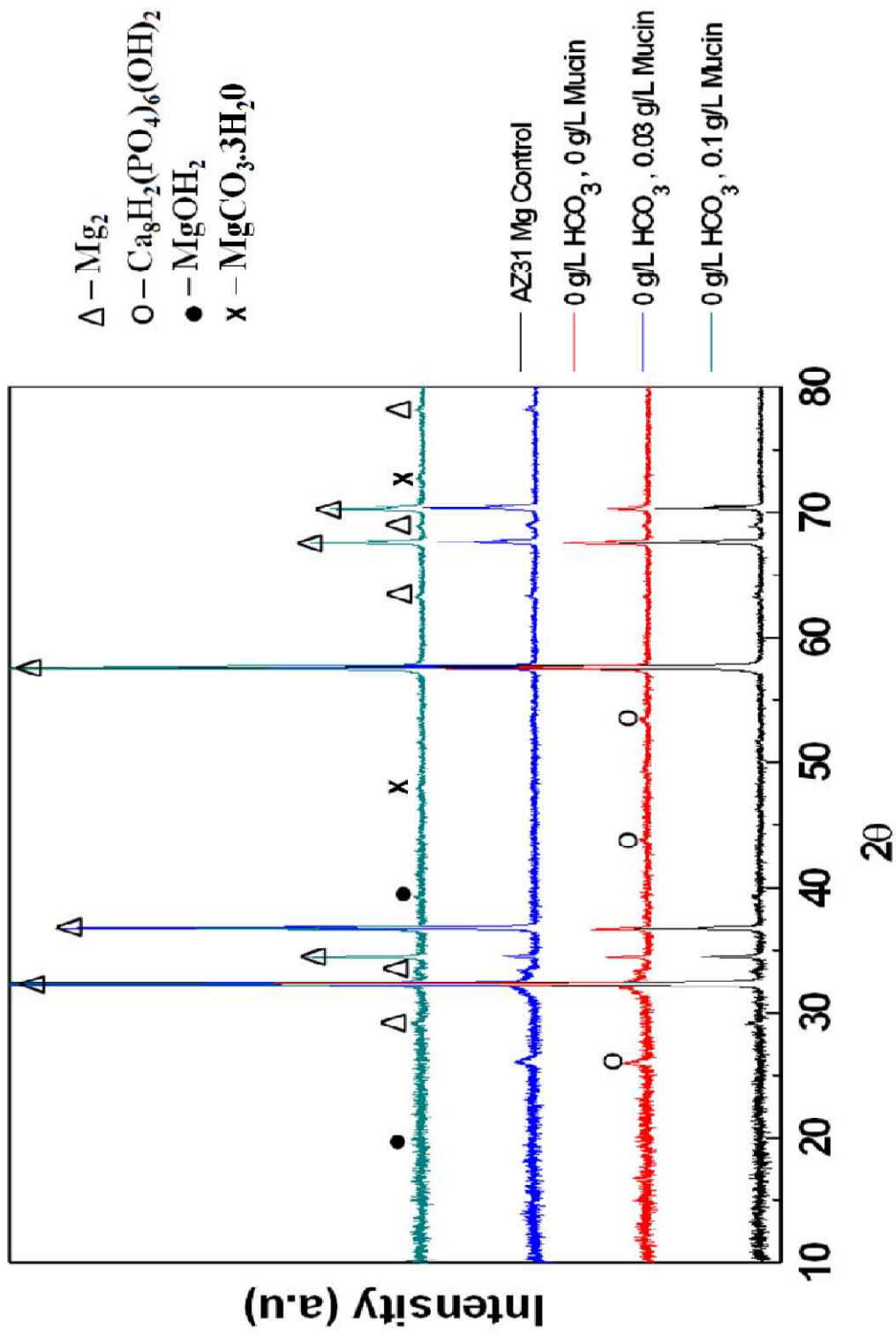


Figure 36. XRD patterns of studied Mg alloy comparing peaks from the different solutions with different mucin

concentration after 10 day immersion test

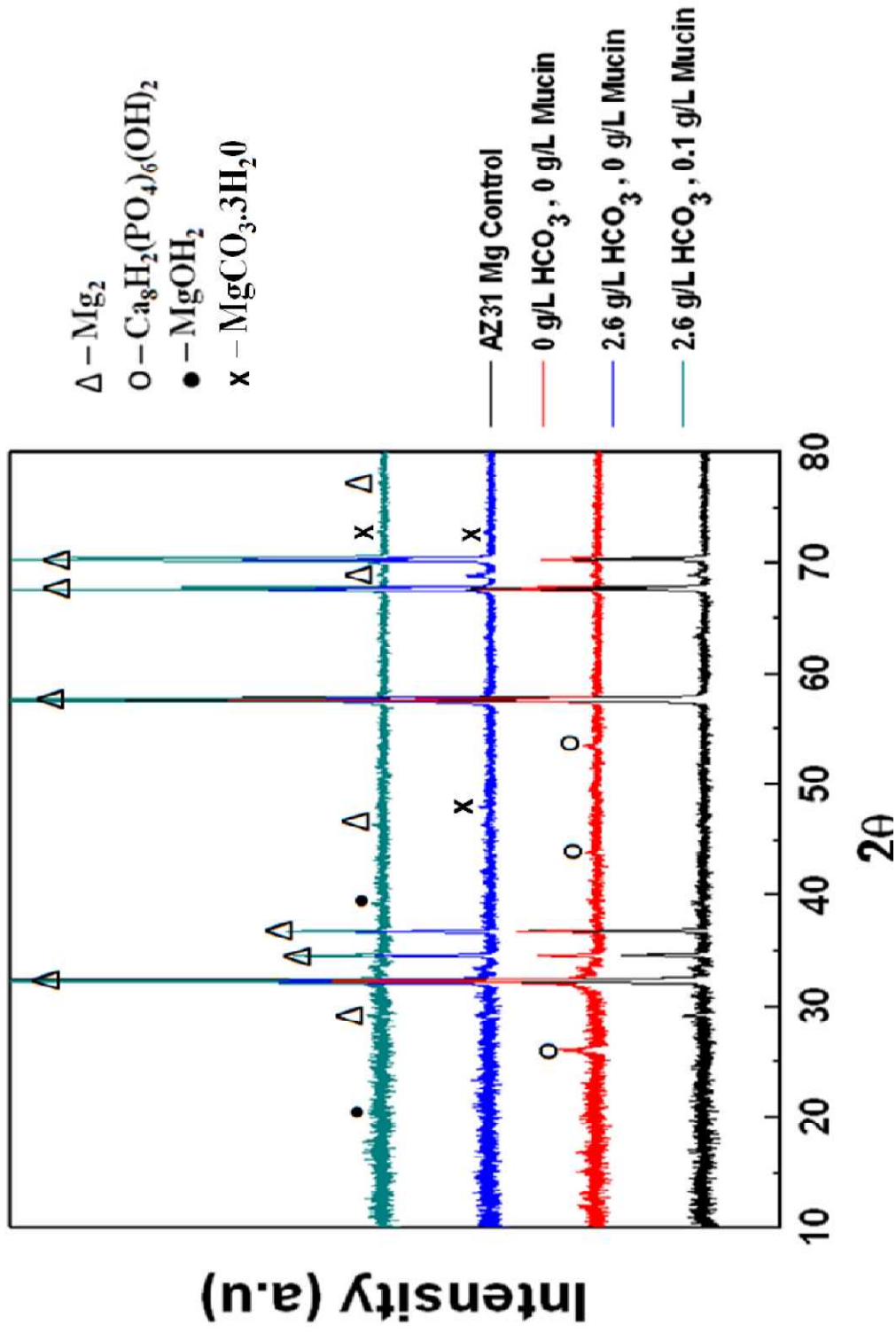


Figure 37. XRD patterns of studied Mg alloy comparing peaks of samples immersed in 0 g/l HCO_3 , 0 g/l mucin, 2.6 g/l HCO_3 , 0 g/l mucin and 2.6 g/l HCO_3 , 0.1 g/l mucin after 10 day immersion test